TWO-PHASE FLOW DYNAMICS
BY REAL-TIME NEUTRON IMAGING
IN OSCILLATING HEAT PIPE

A Thesis

presented to

the Faculty of the Graduate School

at the University of Missouri-Columbia

In Partial Fulfillment

of the Requirements for the Degree

Master of Science

---

by

Il Yoon

Dr. William H. Miller, Thesis Supervisor

AUGUST 2008

The undersigned, appointed by the dean of the Graduate School, have examined the thesis entitled

TWO-PHASE FLOW DYNAMICS

BY REAL-TIME NEUTRON IMAGING

IN OSCILLATING HEAT PIPE

presented by Il Yoon,

a candidate for the degree of Master of Science,

and hereby certify that, in their opinion, it is worthy of acceptance.

Professor William H. Miller

Professor Robert A. Winholtz

Professor Mark A. Prelas

To my family, God's special gift to me, Dad, Mom, brother Soo-ryun and sister-in-law Hey-jin.

ACKNOWLEDGEMENTS

First of all and most of all, I would like to thank my God. He has encouraged and strengthened me consistently with His wisdom and creativeness to complete this work.

I would like to thank Dr. Robert A. Winholtz. He has provided me excellent guidance and supports to finish this work as well as taught me many useful lessons for my future research. His suggestions and creative ideas have inspired me to make this thesis more valuable. I would like to thank to my supervisor Dr. William H. Miller. He introduced me to this work and gave me important advices to complete my thesis. I would like to thank Dr. Mark A. Prelas who evaluate this work as a committee member. I also would like to thank the rest of professors in Nuclear Science and Engineering Institute, Dr. Sudarshan K.Loyalka, Dr. Tushar K.Ghosh and Robert V. Tompson. Further, I would like to thank departmental secretary Latricia J. Vaughn who has helped me with beautiful smile.

I would like to thank Corey Wilson and Brian V. Borgmeyer who are colleagues for the experiments done for this thesis. I also would like to thank David L. Jacobson and Daniel S. Hussey who are scientists at Neutron Imaging Facility, NIST.

I would like to express special thank to my family who pray for me. Thanks Dad, Mom, Soo-ryun and Hey-jin.

I acknowledge the support of University of Missouri Research Board for financial assistance.

I also acknowledge the support of the National Institute of Standards and Technology, U.S. Department of Commerce, in providing the neutron research facilities used in this work.

TABLE OF CONTENTS

LIST OF FIGURES

LIST OF TABLES

TWO-PHASE FLOW DYNAMICS BY REAL-TIME
NEUTRON IMAGING IN OSCILLATING HEAT PIPE

Il Yoon

Dr. William H. Miller, Thesis Supervisor

ABSTRACT

Neutron imaging can produce unique images of objects making it a useful non-destructive technique with various applications in science and industry. Oscillating heat pipes (OHP) are being studied as a higher performance way of cooling high power electronics. They have shown better performance than conventional heat pipes, but little is known about the dynamics of the liquid and vapor inside the OHP. In these studies, the dynamics of liquid and vapor were studied by calculating the liquid and vapor volume fractions in different sections of the OHPs using neutron imaging and the resulting data were compared with external temperature data to investigate the workings of the OHPs. The results show that neutron imaging is a useful technique to quantify the dynamics of the vapor and liquid in OHPs. Imaging shows that at lower heat fluxes water does not circulate around the heat pipe as it does at higher heat fluxes. Instead, the evaporator, where heat is input, is largely vapor with only very short entrances of liquid. In contrast, acetone circulates around the heat pipe at lower heat input as well as at higher heat input. The acetone-OHP shows better performance than a water-OHP due to more active liquid movement. It is inferred that viscosity and density affect the performance of OHP. Temporal volume fraction data corresponds well with temperature data. In contrast, individual temporal volume fraction data does not show as good a correspondence with individual temperature at each thermocouple position.

Chapter 1 Introduction

The curiosity and desire to see and investigate the unseen has been with human kind since the human race existed. Because of the desire to see the magnificent and wondrous universe, human kind developed telescopes. Because of the curiosity to see the small and fine materials such as cells and small universes, they invented microscopes. Human curiosity and desire could not be satisfied with seeing an outward appearance. Thus they developed techniques such as spectrometers to know about the inward characteristics. But, people can naturally be impressive more by seeing directly. The discovery of neutron and its unique characteristic has offered to man a useful method to see the inside of the materials directly.

As electronics become integrated in a small space while performing a heavy work load, the generated heat from the electronics becomes a serious problem to solve for current and further development. The conventional heat pipe has shown good performance for cooling electronic devices. One of the well-known applications is CPU cooling of notebook or desktop computers. But, when the integration of circuits becomes denser, the heat density generated is greater. Thus, there is need to develop a heat transfer device showing better performance. The oscillating heat pipe (OHP) has shown better performance than conventional heat pipes for heat transfer. Thus, it is supposed to be an alternative candidate to the conventional heat pipe for the cooling of electronics. To achieve better performance and application to electronics, an understanding of liquid and vapor dynamics in the OHP tubes is needed. But, their dynamics is not currently well

understood. So, there is a need to look in and investigate the behavior of liquid and vapor inside OHP tubes.

Neutrons have some unique characteristics for an imaging technique. Neutron attenuation coefficients look random while X-ray attenuation coefficients increases with the increasing atomic number of materials. Thus, neutron imaging is usually regarded as complementary method to X-ray radiography. Particularly, different isotopes of the same atom have different neutron attenuation coefficients. Thus, different isotopes can be discriminated with neutron imaging. Neutrons are also very sensitive to hydrogen. This phenomenon is a useful characteristic for studying the dynamics of liquids that contain hydrogen. In addition, neutron imaging has little effect from gamma ray radiation. In these studies, the water and acetone were used as the working fluid in OHPs. Both water and acetone have hydrogen. The oscillating heat pipes are made from copper, so when they are irradiated by neutrons, they becomes activated and emit gamma rays. Thus neutron imaging is the proper technique for these studies.

There are some previous studies about two-phase flow volumetry using neutron imaging. In previous studies there exist two kinds of calibration methods, roughly, for two-phase volumetry. One is to make calibration curve by making and imaging a calibration sample with different thicknesses and the other one is to take an image when the sample is empty and when it is fully filled with the liquid and to calculate the fraction volume information mathematically. But, in these studies, it was not possible to use previous calibration methods because of experimental conditions. So, there is a need to develop algorithms to analyze flow dynamics in OHP for these studies.

The performance of OHPs has been investigated by some other research groups. By analyzing temperature data, the behavior of liquid in tubes was estimated. The dynamics of liquid in OHPs also have been studied by watching the movement of liquid directly. But, transparent materials such as glass were used to see the inside of the tube. The behavior of liquid in glass tubes may not be same in copper heat pipes. Thus, there is need to watch the movement of liquid in copper heat pipes directly. So, in these studies, the dynamics of the liquid in OHPs were imaged by neutron imaging and then to analyze the movement. Vapor and liquid volume fractions were calculated using algorithms developed for this work.

Chapter 2 Background

Neutron radiography

Neutron radiography is one of the imaging methods that can be used to make an image using neutrons. It can produce image data which have advantages that other imaging techniques do not have based on the characteristics of neutrons. Neutrons are penetrable to many kinds of materials. Their linear attenuation coefficients vary according to materials differently than other radiations making neutron radiography a unique technique in imaging technology.

The imaging method was developed initially based on visible light whose wavelength ranges from approximately 400 nm to 700 nm because the human eye can only detect visible light. As a detecting techniques were improved, its usable wavelength range was widened from visible light to UV, IR, X-ray, gamma ray, etc. These improvements were not limited to electromagnetic waves only. Some particles such as electron and neutron, and recently positron can be used for imaging. Each imaging technique has its own characteristics useful in special situations based on its source and principle. Thus, the need to visualize an unseen sample and the discovery of new imaging sources has led to new ways to investigate samples of interest. The neutron was discovered by Chadwick in 1932. Its discovery led the experiments about neutron radiography by H. Kallmann and E. Kuhn in the 1930's (Berger 1971). But, extensive work on development and application was started in 1960's because good neutron sources became more available during this decade (Berger 1970).

Neutron radiography consists of three principle components, a neutron beam, a

sample to be irradiated, and a recording device (Harms and Wyman 1986). In Figure 2.1, the neutron beam is emitted from the neutron source via the collimator and penetrates the sample. Then, the penetrated neutron beam is recorded at detector, converting it into the image data.

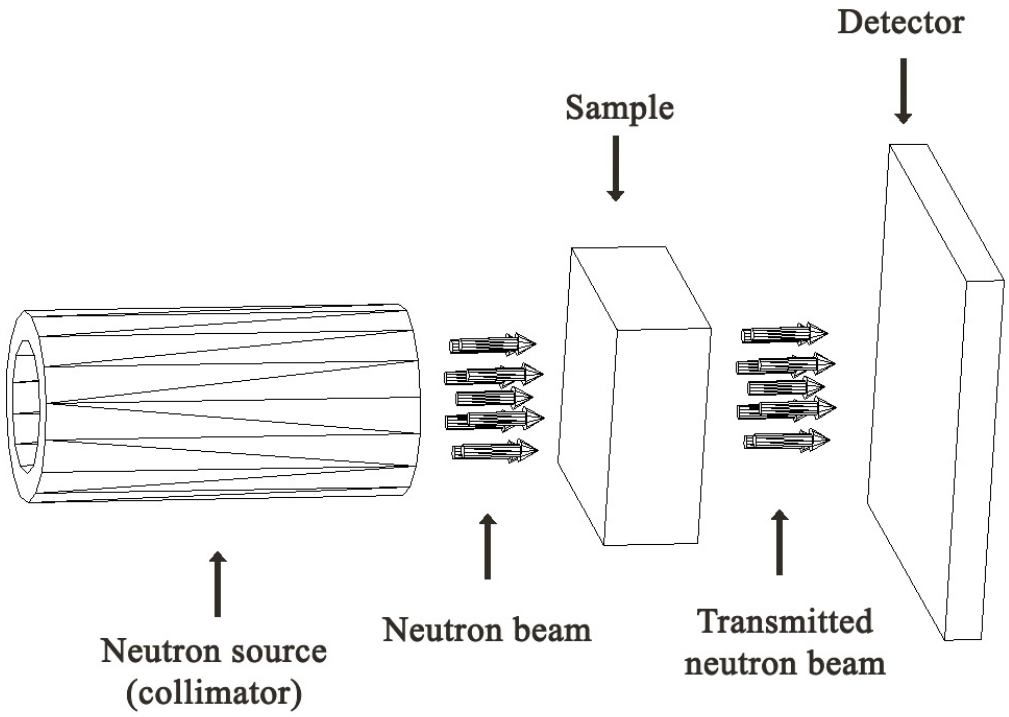

Figure 2.1. The schematic view of a neutron radiography device

Neutrons readily penetrate many kinds of materials, like X-rays. Thus neutron and X-ray radiography are useful for examining the inside of specimens. But, there are some advantages for neutron radiography because of the unique characteristics of neutrons. The attenuation coefficients for neutrons for the elements are seemingly random, while the attenuation coefficients for X-rays are proportional to the atomic numbers of elements. Thus, neutron radiography can produce contrast in images of materials that X-ray radiography cannot do (Berger 1970). This is why sometimes neutron radiography is

considered as a complementary method to X-ray radiography. This gives neutron radiography a unique advantage. Figure 2.2 shows mass attenuation coefficients for the elements for neutrons and X-rays (Berger 1971). The other characteristic of neutrons is that the attenuation of neutrons is different for different isotopes of same element (Berger 1970). For example, the cross section of 0.0253-eV neutrons for boron-10 is 3837 barns while boron-11 0.0055 barns (Glasstone and Sesonske 1994). Thus, it is possible to discriminate different isotopes of the same element with the image data by neutron radiography. This is another advantage of neutron radiography. The detection of neutrons can have little or almost no effect from gamma ray radiation. Sometimes, there are needs to make an image of highly radioactive samples or some samples become radioactive during irradiation by neutron flux. In these cases, neutron radiography can produce images regardless of gamma ray radiation (Berger 1970). For example, in these experiments, the sample, copper heat pipes, were activated when taking images because they was irradiated by neutrons.

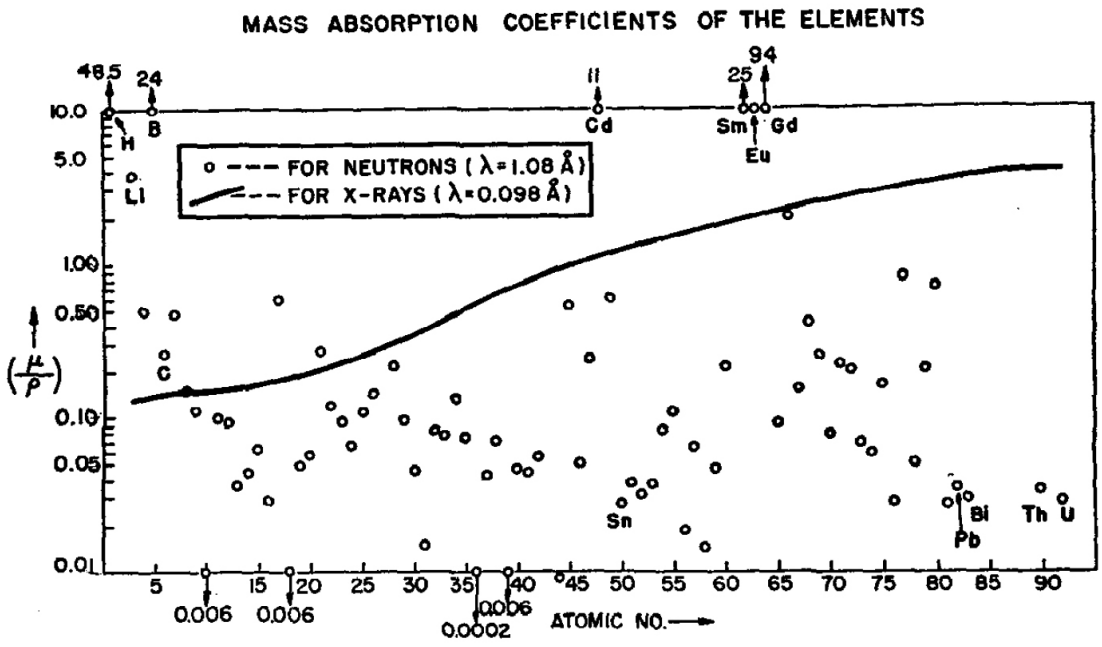

Figure 2.2. Mass attenuation coefficients ($cm^2 \cdot g^{-1}$) of neutron and X-ray for the elements. It shows that mass attenuation coefficients for neutron are random while for X-ray are proportional to the atomic number (Berger 1971).

The neutron beam from a neutron sources usually has too high of an energy spectrum for normal purpose neutron radiography. Thus, there is need to reduce or moderate its energy where the attenuation of neutrons has the most differences for materials. Thus, the fast neutron source is surrounded by moderator to reduce neutron energy (Hawkesworth and Walker 1983). To direct a neutron beam toward the sample, a collimator is needed. There are three types of collimator: the simple straight parallel collimator, a Soller slit collimator, and a divergent collimator (Berger 1970).

The primary characteristics of a neutron beam for neutron radiography are the intensity, the energies of the neutrons, the degree of collimation, and the beam quality. The intensity of neutron beam is the main factor controlling the exposure time. The energy of the neutrons is the main factor determining the penetration powers though the sample. The degree of collimation is the main factor determining the image quality or

spatial resolution. It is defined as the collimator length to diameter (L/D) ratio. The beam quality is the main factor controlling the non-neutron background in the image data. It is defined as n/γ ratio or the neutron to gamma ray ratio (Hawkesworth and Walker 1983).

The spatial resolution of thermal neutron radiography is usually described by the term Ug, 'geometric unsharpness' or penumbral. Ug is from the image practiced by X-radiography and defined as

$$Ug = S(D/L) \tag{2.1}$$

where L is the length of collimator plus distance from the end of collimator to the sample, D is the entrance diameter of collimator and S is the distance between a sample and the image recorder. A lower L/D produces a higher beam intensity and shorter exposure time, which can produce a better image quality. A higher L/D produces a better image resolution. Thus, there is confliction in the L/D ratio and the best L/D ratio should be chosen by compromise between these two factors (Hawkesworth and Walker 1983).

Three types of neutron sources are used: reactor, accelerator, and radioactive isotopes (Hawkesworth and Walker 1983). Among them, reactor sources are the most widely used. There is sometimes a need to produce a neutron radiographic image of a sample that cannot be moved to a reactor thus, alternative neutron sources, accelerator or radioactive isotopes, were introduced to neutron radiography (Hawkesworth and Walker 1983). However, the neutron beam from an accelerator or radioactive isotopes gives lower image quality and throughput. The most widely used reactions for accelerator based neutron radiography are

$${}^{3}_{1}T + {}^{2}_{1}D \rightarrow {}^{4}_{2}He + {}^{1}_{0}n + 17.6MeV \tag{2.2}$$

$$^{9}_{4}Be+^{2}_{1}D\rightarrow^{10}_{5}B+^{1}_{0}n+4.35MeV \quad (2.3)$$

$$^{9}_{4}Be+\gamma\rightarrow2^{4}_{2}He+^{1}_{0}n-1.67MeV\,. \quad (2.4)$$

Radioactive isotopes are useful because they can be moved and are easy to use. Their disadvantage is the lower beam intensity which gives lower image quality in the same exposure time. The half-lives of isotopes are another disadvantage. The frequently used isotopes are ^{124}Sb-Be, ^{241}Am-Be, ^{242}Cm-Be and ^{252}Cf (Hawkesworth and Walker 1983). Among them, the ^{124}Sb-Be reaction is considered as the most suitable source. It uses the (γ,n) reaction. Antimony (^{124}Sb) is the gamma ray source with an energy of 1.69 MeV and Be is the target to produce the neutron with the mean energy of about 24 keV (Bücherl et al 2004). Its has advantages of being inexpensive and having a good thermalization factor of 50. But, it has short half-life of 60 d with high gamma ray emission from antimony (Hawkesworth and Walker 1983). ^{241}Am-Be, and ^{242}Cm-Be reactions are based on the (α,n) reaction. ^{241}Am-Be has advantages of a long half-life of 458 y, but it has a poor thermalization factor of 200 and is expensive to produce with low specific activity. ^{242}Cm-Be has the advantage of high specific activity but it has low half-life of 163 d (Hawkesworth and Walker 1983). ^{252}Cf uses spontaneous fission to produce neutrons. It has some advantages: compactness, low gamma ray emission, relatively inexpensive cost, high specific activity, and a relatively long half-life of 2.65 y and a good thermalization factor of 100 (Hawkesworth and Walker 1983, Silva and Crispim 2001).

There are several kinds of neutron image detectors. To make images, neutrons should be converted into detectable secondary radiation such as alpha, beta, gamma or light. Conventionally, film-based neutron image detectors are used for neutron radiography (Domanus et al. 1992). A film-based neutron detector has two types: direct

method and transfer method. There are some other methods: track-etch systems and electronic techniques including scintillator–camera systems, neutron image intensifiers and fast framing systems (Berger 2004).

A digital detector is replacing a film detector for neutron radiography. A digital detector does not have better image resolution than a film detector, but it has many advantages comparable to a film detector. Actually, resolution of some digital detectors is close to a film detector. With the reasonable resolution, its advantages are following: high efficiency, high sensitivity, fast read out, high frame rate, wide dynamic range, and high linearity. In addition, it is suitable for quantitative evaluation, image post-processing, archiving and data transfer, and tomography (Lehmann et al. 2004).

Currently available digital detectors are a CCD camera based detector, imaging plate system, amorphous silicon flat panel system, and pixel detectors. A CCD camera based detector uses Li-6 doped ZnS panel for a scintillator. To reduce dark current producing noise on the image, cooling technique is applied to some CCD cameras. For low light image detection, MCP intensifier can be used with CCD camera. An imaging plate system uses Eu doped BaFBr substrates. The incidence of neutron excites electrons in semi-stabilized state and those electrons are deexcited by scanning laser and emit photons. And, then, emitted photons are gathered and multiplied by PMT to reconstruct image information. The advantage of imaging plate system is its high sensitivity and wide dynamic range. The advantage of amorphous silicon flat panel system is that it can be placed into the neutron beam directly and, thus, it is possible to get the real time images (Lehmann et al. 2004).

Oscillating Heat Pipes (OHP)

Currently, as the integration of chips becomes higher and the size of the circuits becomes smaller, dissipation of the heat generated from the electronic device becomes a more important problem to solve for further development. The concept of the oscillating (or pulsating) heat pipe (OHP) was initially developed by Akachi (1990). The advantages of an OHP compared to a traditional heat pipe are a high driving force, lower pressure drops, and higher heat transfer coefficients (Ma, Hanlon and Chen 2006). A mathematical model for the oscillating motion of the fluid in an OHP was done by Ma, (2006).

An OHP is a set of capillary tubes connected continuously each other. It is usually divided into three parts: evaporator, condenser, and an adiabatic region (Karimi and Culham 2004; Ma, Hanlon and Chen 2006). Figure 2.3 shows a schematic view of a typical OHP. The oscillating motion of the OHP is caused by pressure differences between the evaporator and condenser. The OHP is initially evacuated and filled partially with a fluid such as water or methanol. The partially filled liquid is distributed throughout the pipe and liquid slugs or vapor bubbles are formed. The oscillating movement is caused and maintained by a non-equilibrium pressure state. The heat is supplied at the evaporator, and then vapor bubbles become larger. This means that the pressure at the evaporator becomes higher. Because of this non-equilibrium pressure, liquid slugs are pushed to the condenser which has relatively lower pressure. This is the driving force. At the condenser, the vapor bubbles become smaller and release their heat obtained at the evaporator. In this way, the non-equilibrium pressure state is maintained. Because tubes are connected each other, the movement of liquid slugs and vapor bubbles in one tube can cause the fluidic movement in another other adjacent tube. This is a restoring force. The

combination of movement due to the driving force and the restoring force produces oscillating movement in the OHP. During operation there is no equilibrium pressure state.

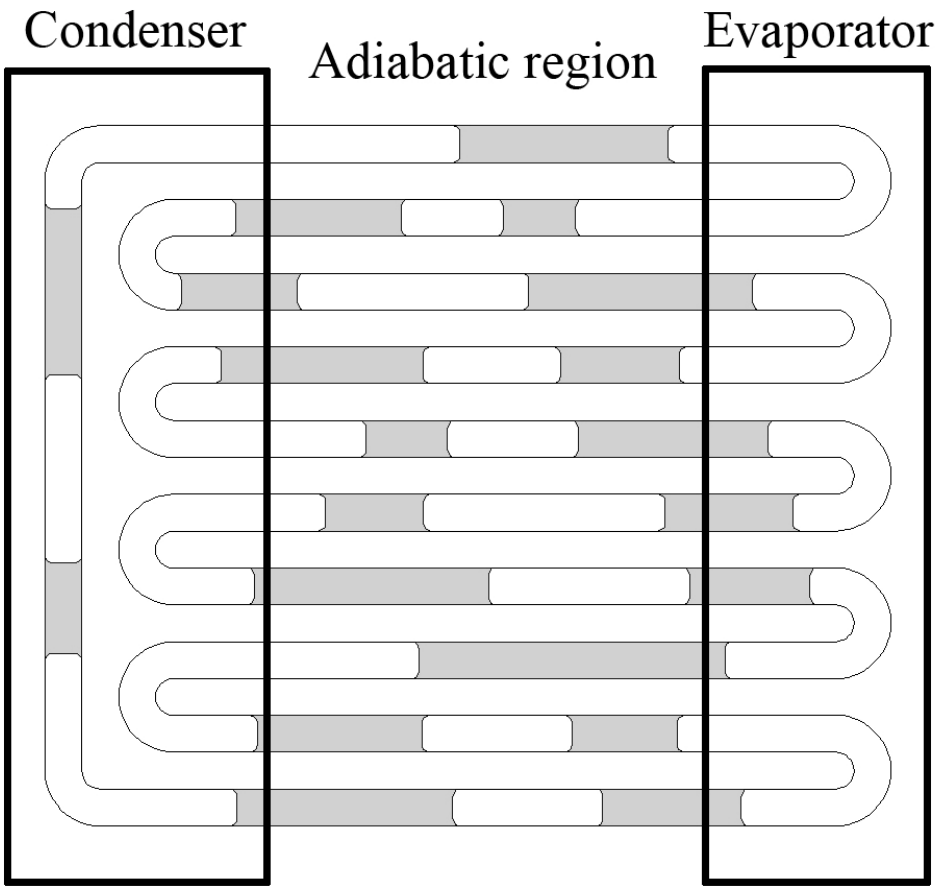

Figure 2.3. The schematic view of OHP. The gray colored sections are liquid, while white colored sections are vapor in tubes.

The thermal performance of an OHP is determined by temperature difference between the evaporator and condenser at a supplied heat input. The factors affecting the temperature difference are the structure, shape, material, and length of tubes. In total, five thermal resistances affect the performance of OHP. They are two thermal resistances in the wall, R_{wall}, a thermal resistance by evaporation at the evaporator, R_{evp}, a thermal

resistance by condensation at the condenser, R_{cond}, a thermal resistance along the pipe, $R_{l\text{-}v}$ (Figure 2.4). The heat capacity, Q, is defined as

$$Q = \frac{\Delta T}{2R_{wall} + R_{evp} + R_{l-v} + R_{cond}} = \frac{\Delta T}{\frac{L_{eff}}{k_{eff} \cdot A_{cross}}} \tag{2.5}$$

where ΔT is the overall temperature difference along the pipe, k_{eff} is the effective thermal conductivity, L_{eff} is effective thermal length, and A_{cross} is the cross-sectional area of the tube. Among the factors, a thermal resistance by evaporation at the evaporator, R_{evp}, a thermal resistance by condensation at the condenser, R_{cond}, and a thermal resistance along the pipe, $R_{l\text{-}v}$ are important in determining the performance. A high thermal conductivity is needed to remove the heat by connecting from the tubes to a heat sink. The effective thermal conductivity is calculated by the Equation 2.5 (Karimi and Culham 2004).

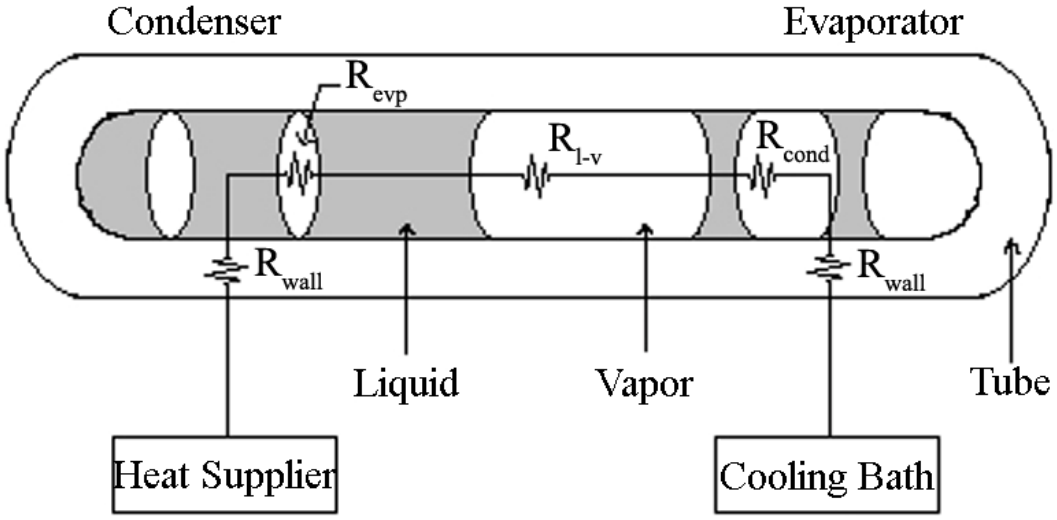

Figure 2.4. Thermal resistance in OHP (Karimi and Culham 2004)

It has been reported that flow boiling heat transfer coefficients varying from 1000 to 6500 W/m^2·°C (Kandlikar and Steinke 2002). Based on these values, the thermal

resistance in the evaporator is obtained from (0.001/A) and (1.54 x 10^{-4}/A)°C/W. The total thermal resistance for a typical OHP has range from of (3.29 x 10-4/A) and (2.10 x 10-3/A) *°C/W.* The estimated maximum and minimum thermal conductivities for an OHP whose length is 20 cm, with various heating/cooling and cross sectional area are shown in Table 2.1. As shown in Table 2.1, the maximum effective conductivity is about 24 *kW/m·°C,* approximately 10 times higher than that of diamond (Karimi and Culham 2004).

Table 2.1. Estimated maximum and minimum thermal conductivities for an OHP according to its dimensions (Karimi and Culham 2004)

A_{cross} [cm^2]	$A_{evp} = A_{cond}$ [cm^2]	$k_{eff,min}$ [$W/m^{2}.°$ C]	$k_{eff,max}$ [$W/m^{2}.°$ C]
0.3	9	2,86	18,24
0.4	16	3,81	24,32
0.6	9	1,43	9,12
0.9	16	1,91	12,16

For choosing working fluid, the following factors should be considered: operating vapor temperature range, compatibility with the heat pipe materials, thermal stability, wettability, reasonable vapor pressure, high latent heat and thermal conductivity, low liquid and vapor viscosities, and acceptable freezing point. The working temperature for an OHP is varies. It can be from cryogenic to high temperatures. But, usually, the working temperature range for OHP is from approximately 50 °C to 150 °C (Karimi and Culham 2004). Water and methanol are typically considered for the working fluid. Water is good fluid because it has a high latent heat, high thermal conductivity, and is safe. The copper/water OHP is normally used for electronic cooling applications. Methanol has a lower surface tension than that of water. Copper/methanol is preferable to copper/water when a OHP is operated at or below 0 °C.

Capillary forces are an important factor for the operation of an OHP. Thus, the internal pipe diameter should be considered because the capillary forces depend on it. A theoritical maximum tolerable inner diameter has been defined as

$$D_{\max} = 2\sqrt{\frac{\sigma}{g(\rho_{liq} - \rho_{vap})}} \tag{2.6}$$

where σ is the surface tension, g is the gravitational acceleration, and ρ is the density (Karimi and Culham 2004). Liquid slugs should be stable in operation. To be stable, D should be lower than D_{max}. This creates an arangement of alternating liquid and vapor slugs and prevents counter flow between the liquid and vapor phases.

The filling ratio is the volume fraction of the tubes initially occupied by liquid (Karimi and Culham 2004). Determination of the filling ratio depends on the type of working fluid, operating parameters, and construction. The actual filling ratio is usually 20-70%. At lower filling ratio, more oscillations are possible because more vapor bubbles are produced. But, it is accompanied with reduced liquid mass, causing less sensible heat transfer. At higher filling ratios, there are fewer oscillations, causing reduced performance. At close to 0% filling ratio, there is almost no liquid in the pipe. This means that there is a high thermal resistance, reducing the performance. At close to 100% filling ratio, there is very little vapor. So, almost no oscillation is occurred and this causes reduced performance.

Two-phase Volumetry by Neutron Radiography

There have been a number of investigations to find the volume fraction information in two-phases flow images obtained by neutron radiography. One of methods is to make a calibration sample and compare with the intensity of the image. One of the

investigations using this method is described as follows. The air-water and steam-water flow in a narrow rectangular duct and a small diameter tube was imaged by neutron radiography and the void fraction of the vapor phases was measured by image processing technique (Hibiki et al 1992). A calibration sample made of aluminum alloy was prepared to measure the void fraction. The sample had five gaps (0.5, 1.0, 1.5, 2.0, 2.5, 3.0mm) and each gap was filled with deionized water. An image of the calibration sample filled with water was taken and compared with the thickness of water in the sample. After several image corrections, a comparison between image intensity and the thickness of water was made and calibration data was calculated. Then, 255 images of two-phase flow were taken and integrated. The resulting integrated image was divided into 480 × 512 cells (pixels). The intensity of each pixel of the image was compared with the calibration curve to find the thickness of water. Then, from the thickness of water, the void fraction in the two-phases flow was calculated.

Some studies were also done without preparing a calibration sample. Volume fraction measurement of multiphase flow by neutron radiography was done by Sonoda et al (1992). In this investigation, water two-phase flow distributed in a convergent-divergent nozzle and two-phase flow generated by nozzles were made. The attenuation of neutron beam intensity by a nozzle and water two-phase flow was calculated as

$$I = I_0 \exp\left\{-\mu_A \rho_A X_A - (1-\alpha)\mu_W \rho_l X_N - \alpha \mu_W \rho_g X_N\right\} \tag{2.7}$$

where subscripts A, W, l and g are aluminum nozzle, water, liquid and gas respectively. μ_A and μ_W are mass attenuation coefficients for aluminum and water. ρ_A, ρ_l and ρ_g are density of aluminum, liquid and gas. X_A and X_N is the thickness of aluminum and nozzle. α is the void fraction to be calculated. Before the water flowed down, the intensity of the image is

calculated as

$$S_{BK} = G\exp(\mu_A \rho_A X_A) + O \tag{2.8}$$

and after the water flowed down, the intensity of the image is calculated as

$$S_{TP} = G\exp\{(1-\alpha)\mu_W \rho_l X_N - \mu_A \rho_A X_A\} + O \tag{2.9}$$

where G and O are gain and offset of the video signal. Then, Equation 2.9 is divided by Equation 2.8 and resulting equation is expressed as

$$\frac{S_{TP} - O}{S_{BK} - O} = \exp\{(1-\alpha)\mu_W \rho_l X_N\}. \tag{2.10}$$

From Equation 2.10, the void fraction α was calculated.

A similar method to calculate the void fraction for two-phase flow was done by Asano et al. (2004), Asano et al. (2005) and Sarkar et al. (2005). In this method, it was assumed that the brightness of the image is proportional to the neutron beam intensity detected and the neutron beam intensity attenuation by the gas phase is zero. The attenuated brightness by two-phase flow in the image is defined as

$$S_{tp}(x,y) = G(x,y)\exp[-\rho_w \mu_{mw} t_w(x,y) - \{1-\alpha(x,y)\}\rho_L \mu_{mL} t(x,y)] + O_{tp}(x,y) \tag{2.11}$$

where subscripts w and L are wall and liquid, $t(x,y)$ is the thickness of the two-phase flow and α is the average void fraction, $G(x,y)$ is gain and $O(x,y)$ is the offset. The brightness of fully filled gas and fully filled liquid are defined respectively as

$$S_1(x,y) = G(x,y)\exp[-\rho_w \mu_{mw} t_w(x,y)] + O_1(x,y) \tag{2.12}$$

and

$$S_0(x,y) = G(x,y)\exp[-\rho_w \mu_{mw} t_w(x,y) - \rho_L \mu_{mL} t(x,y)] + O_0(x,y). \tag{2.13}$$

Then, the two-dimensional void fraction distribution is defined as

$$\alpha(x,y) = \frac{\ln\left[S_{tp}(x,y) - O_{tp}(x,y)\right] - \ln\left[S_0(x,y) - O_0(x,y)\right]}{\ln\left[S_1(x,y) - O_1(x,y)\right] - \ln\left[S_0(x,y) - O_0(x,y)\right]}. \tag{2.14}$$

(Asano et al. 2004).

Another method was done by Uchimura et al (1998). In this method, the void fraction α is expressed as

$$\alpha = \frac{A_g}{A_l + A_g} = \frac{\int_{x_1}^{x_2} (z_2 - z_1)dx}{\int_{x_1}^{x_2} (z_3 - z_0)dx} \tag{2.15}$$

where A_g and A_l are the cross-sectional area of gas and liquid respectively, and z_0, z_1, z_2, and z_3 are shown in Figure 2.5. The x_1 and x_2 in the equation indicate the pipe region. The neutron intensity with the gas in the tube is expressed as

$$I = I_0 \exp\{-\sigma(z - z_0)\} \qquad \text{at } z_0 \le z \le z_1 \tag{2.16}$$

$$I = I_1 = I_2 = I_0 \exp\{-\sigma(z_1 - z_0)\} \qquad \text{at } z_1 < z \le z_2 \tag{2.17}$$

$$I = I_2 \exp\{-\sigma(z - z_2)\} \qquad \text{at } z_2 < z \le z_3 \tag{2.18}$$

where σ is the attenuation coefficient. I_0 and z are shown in Figure 2.5. The neutron intensity without the gas in the tube is expressed as

$$I_3' = I_0 \exp\{-\sigma(z_3 - z_0)\}. \tag{2.19}$$

Then, the averaged void fraction σ(y) is expressed as

$$\alpha = \frac{\int_{x_1}^{x_2} \ln\left(\frac{I_3}{I_3'}\right)dx}{\int_{x_1}^{x_2} \ln\left(\frac{I_0}{I_3'}\right)dx}. \tag{2.20}$$

The brightness at the background image where there is no pipe corresponds to I_0. The

brightness of the pipe in the image with the gas and without the gas corresponds to I_3 and I_3'. Then, averaged void fraction σ(y) is expressed as

$$\alpha(y) = \frac{\sum_{x=x_1}^{x_2} \left(\ln I_{BUBBLE}(x,y) - \ln I_{NON-BUB}(x) \right)}{\sum_{x=x_1}^{x_2} \left(\ln I_{AVERAGE} - \ln I_{NON-BUB}(x) \right)}. \tag{2.21}$$

where $I_{AVERAGE}$ is the brightness of the pipe section with the background removed, and $I_{NON\text{-}BUB}$(x) and I_{BUBBLE}(x,y) are the brightness of the pipe in the image without and with the gas, respectively (Uchimura et al. 1998).

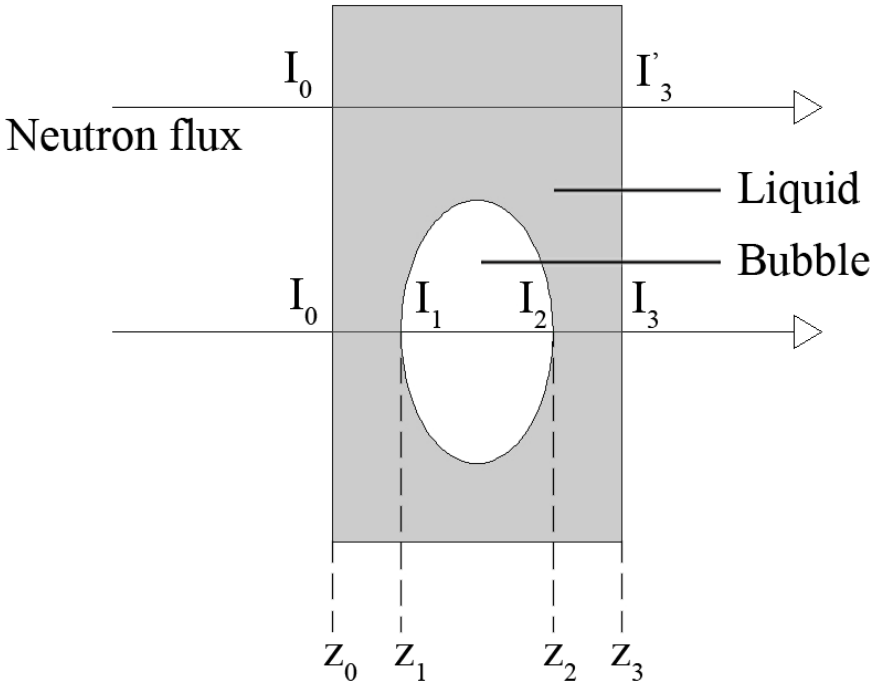

Figure 2.5. The model for the measurement of void fraction in two-phase flow (Uchimura et al. 1998)

Chapter 3 Experimental Setup and Procedure

Neutron Radiography Facility at NIST

A description of the neutron radiography facility at NIST follows (Jacobson et al. 2006). An exterior photograph and floorplan drawing are shown in Figure 3.1. The experimental area, inside a radition shielded cave, has a volume of 30 m^3. The neutron source is a 14 cm diameter disk with a fluence rate of about 1×10^{14} cm^{-2} s^{-1}. The source is imaged through a pinhole to the sample position. The maximum diameter of the pinhole aperture, d, is 2 cm. The distance, L, downstream of the aperture to the sample position can vary from 1 to 6 m. For this work, the sample position remained fixed at 6 m. In Table 3.1, the beam diameter and fluence rate are given at various aperture settings and sample distances.

Table 3.1 Beam properties at neutron radiography facility, NIST. The fluence rates, beam diameters and L/d ratios at the object position are listed (Jacobson et al. 2006).

L (m)	d (cm)	L/d	Beam Dia. (cm)	Fluence Rate 15 cm Bismuth (s^{-1} cm^{-2})
2	2.0	100	8	1.53×10^8
3	2.0	150	13	6.80×10^7
4	2.0	200	17	3.83×10^7
6	2.0	300	26	1.70×10^7
6	1.5	400	26	1.00×10^7
6	1.0	600	26	4.30×10^6
6	0.5	1200	26	1.00×10^6
6	0.1	6000	26	4.30×10^4

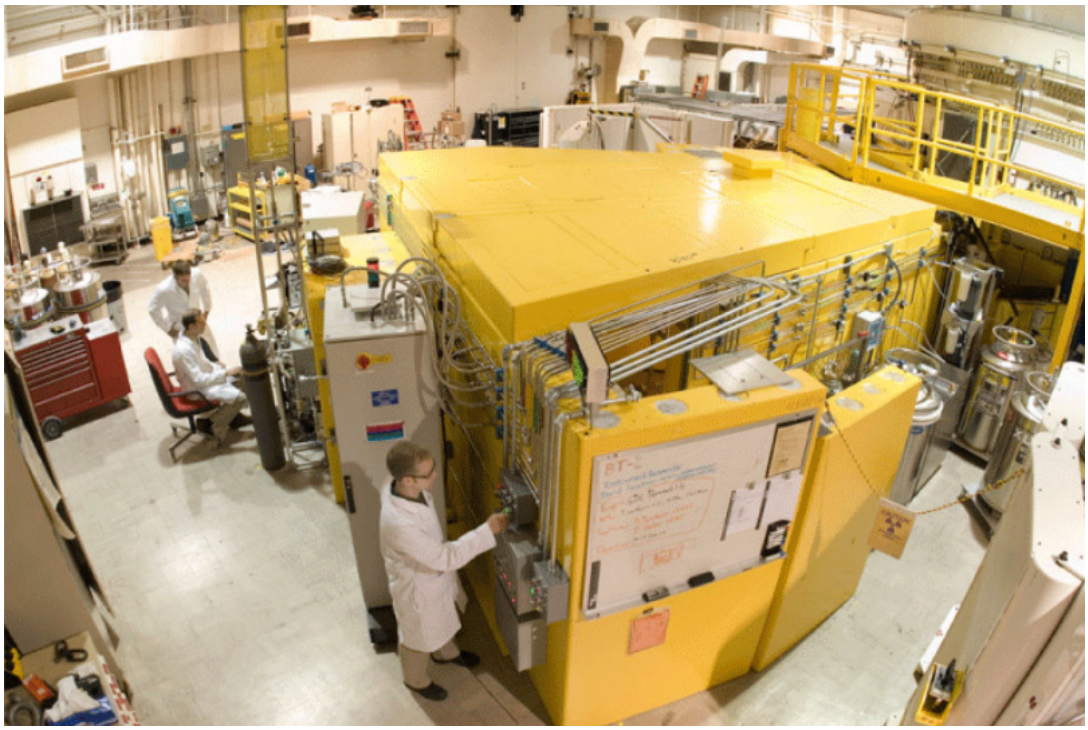

(a) Photo of the neutron imaging facility at BT-2, NIST

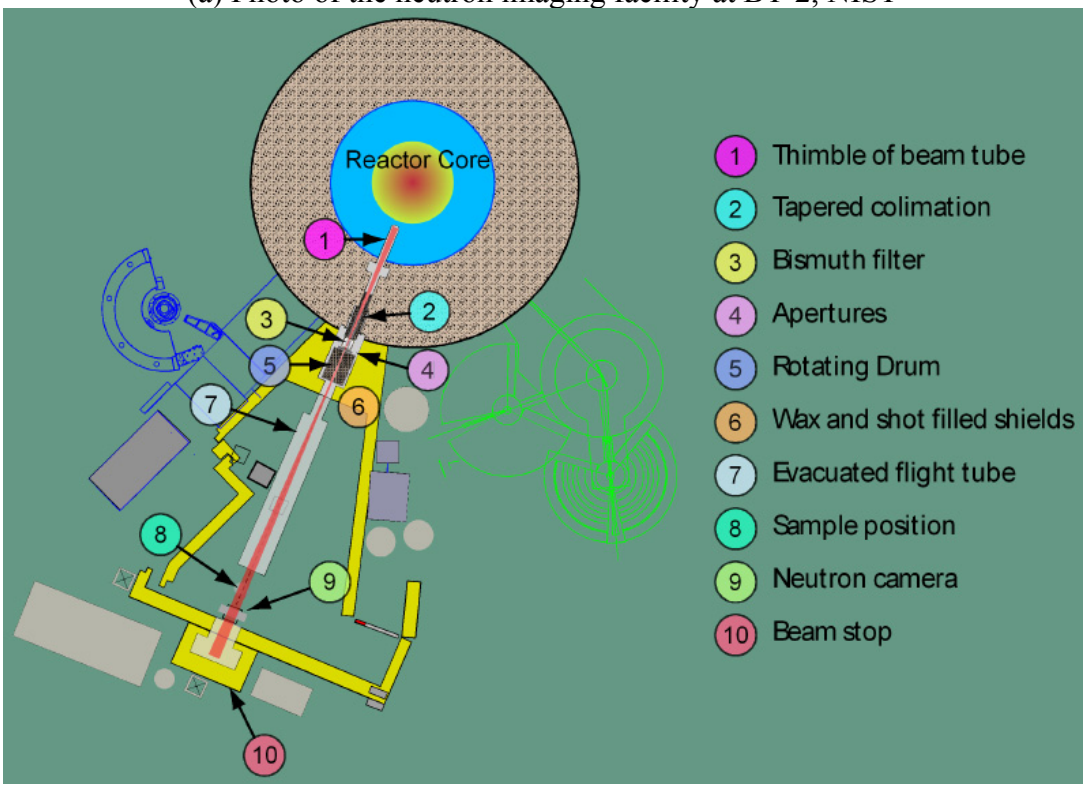

(b) A schematic view of the facility with the components indicated

Figure 3.1. Photo and a schematic view of the Neutron Imaging facility, NIST (adapted from Jacobson, 2007).

The neutron beam for neutron imaging technique is emitted from through the thimble inside the reactor. The collimator is located in the beam port. It has a tapered shape and is composed of a steel shell filled with heavy concrete. The determination of the collimation angle depends on the diameters of the aperture and thimble. The collimator used for this facility (Figure 3.2) is designed not only to collimate the neutron beam but also to reduce gamma ray and fast neutrons from the reactor core (Jacobson et al. 2006). A bismuth filter (Figure 3.3) is located in the beam path to reduce the gamma ray and fast neutron intensity. To reduce phonon scattering by thermal neutrons, it is cooled by liquid nitrogen using a special 'Banjo' dewar (Figure 3.4). Experimental data showed that 50% of the initial beam intensity was reduced by a filter of 5 cm thickness. A bismuth filter of 15 cm is used now. It reduces the thermal neutron beam intensity to 12.5% of its initial value.

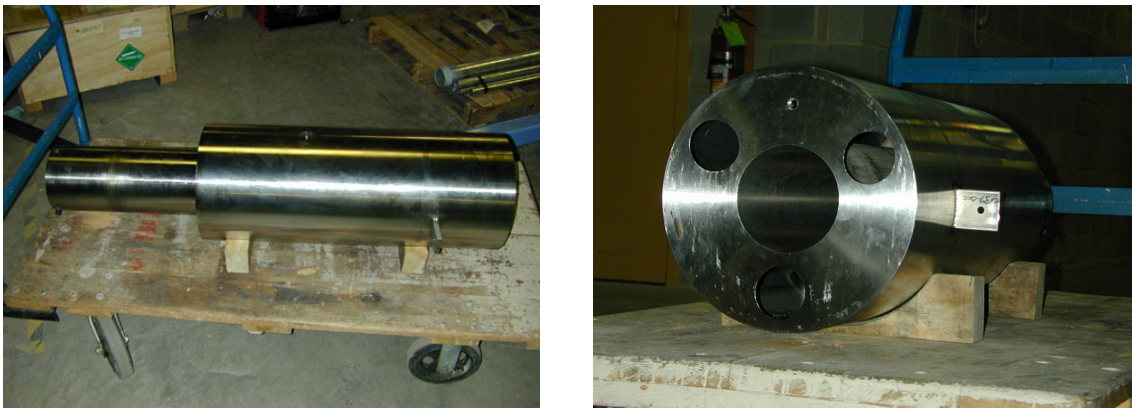

(a) Side-view of collimator (b) Front-view of collimator

Figure 3.2. Photographs of the collimator (Jacobson 2007).

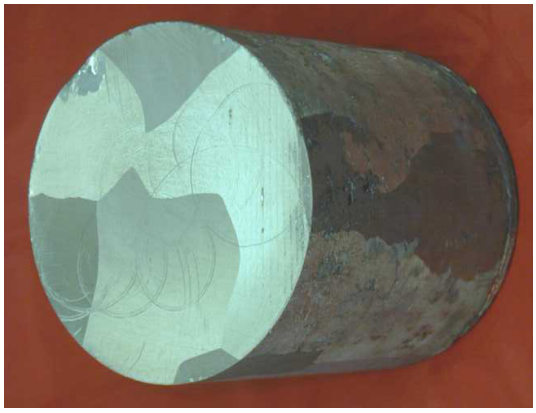

Figure 3.3. Bismuth filter for the Neutron Imaging beam line (Jacobson 2007).

Figure 3.4. Dewar used on the Neutron Imaging beam line (Jacobson 2007).

An aperture assembly is placed in the beam path and consists of several apertures, each linearly aligned. Five apertures can be placed in the aperture card. The aperture card can be moved as needed without reactor shutdown or movement of shielding material. A motorized linear translation device is used to move different apertures into place (Figure 3.5). A rotating drum, filled with heavy concrete, with 3 tubes is also placed in the beam path and works as a fast acting neutron absorber. It is made from cadmium with a thickness of 60 cm along the beam direction. It is rotated to have one of four functions on the beam. Three of them make beam pass through an additional collimator and the last one works as a shutter. Thus, when there is a need to turn on and off the neutron beam quickly during experiment, it can act as a switch (Figure 3.6). Shielding outside the biological shielding is present to reduce the background radiation to users to a very low level. It consists of welded steel boxes filled with steel shot and wax. Background radiation has been measured at or below 2 $\mu Sv\ h^{-1}$ (Jacobson et al. 2006). An evacuated flight tube is placed along the beam path to reduce neutron air scattering. It also reduces radioactive argon-41 generation. There is an adjustable beam aperture made from boron

aluminum and Li-6 plastic at the exit of the flight tube. It modifies the beam shape, initially circular, to be an adjustable rectangle at the sample. It reduces unnecessary activation of the sample and neutron scattering that can affect image quality (Figure 3.7).

Figure 3.5. Aperture assembly for the Neutron Imaging beam line (Jacobson 2007).

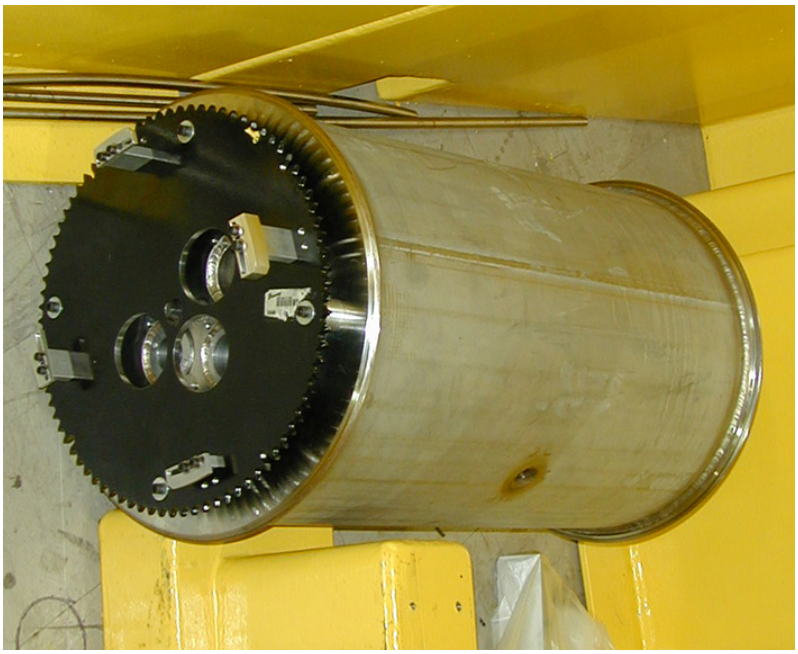

Figure 3.6. Collimator drum for the Neutron Imaging beam line (Jacobson 2007).

Figure 3.7. Flight tube for the Neutron Imaging beam line with adjustable beam aperture (Jacobson 2007).

A removable sample manipulation platform is located between the flight tube and detector. The sample placed on the platform can be translated and rotated under computer control.

For a detection of the transmitted neutrons, a Varian Paxscan 2520 was used (Jacobson et al. 2006). The Paxscan 2520 is an amorphous silicon flat-panel detector with a Li-6 doped ZnS scintillator with 300 μm spatial resolution and is capable of a frame rate of 30 fps. This device converts light to electric charge to reconstruct an image as a CCD does. However, a CCD used in neutron radiography cannot be connected to the scintillator directly because it is damaged by neutron beam irradiation and thus, it needs a mirror and optics to move the CCD out of the neutron beam. The amorphous silicon detector, in contrast, can be directly in contacted with the scintillator without damaging it with the neutron beam. Thus, it does not need a mirror and other optics and, as a result, can improve the light acceptance from the scintillator (Estermann et al. 2005, Estermann and Dubois 2005, Koerner, Lehmann, and Vontobel 2000).

The beam stop is placed to stop neutron beam flight and consists of boron carbide powder in a square box with a magnesium window and steel shot and wax. The thickness of the former is 15 cm and of the latter is 75 cm (Jacobson et al. 2006) (Figure 3.8).

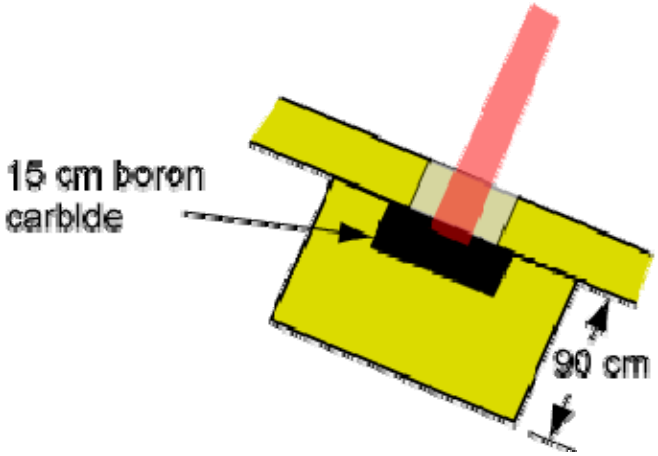

Figure 3.8. Beamstop for the Neutron Imaging beam line (Jacobson 2007)

Oscillating Heat Pipes

Two 6-turn open-loop oscillating heat pipes (OHPs) were used and analyzed, one was filled with high-purity liquid chromatorgraphy (HPLC) water and the other is filled with HPLC acetone purchased from Fisher Scientific, to compare the effect of the working fluid on the heat transfer performance and fluid behavior through imaging. The two OHPs were otherwise identical. Commercially available alloy 122 copper tubing was used to make OHPs. Inner and outer diameters were 1.65 and 3.18 mm, respectively. Alloy 122 copper blocks were used to make condenser and evaporator plates on which to mount the cooling block and heater. Semi-circular grooves were made to place the copper tubes in the copper blocks using a ball end mill. The depth was 3.18 mm for all semi-circular grooves. The size of condenser plate was 155 by 64 mm and the size of evaporator was 155 by 38 mm. The thickness was 6.35 mm for each. A drawing of OHPs with dimensions is shown in Figure 3.9. Before placing the tubing in the grooves, Omegabond '201' thermal paste was placed in the grooves to improve the thermal conductivity between the tubes and the copper plate. The filled ratio of the water-OHP

and the acetone-OHP were 50.0% and 47.7%, respectively. The water and acetone were charged into the OHP as follows. The air in the tube was evacuated with a vacuum pump and then the working liquid inserted into the tubing, filling it. After filling the vacuum pump was used to remove fluid to the intended filled ratio, whereupon the OHP was sealed by cold welding the filling tube shut (Wilson, 2006). The amount of fluid in the OHP was determined with a precision balance from the weights of the OHP compared to its evacuated and completely filled states.

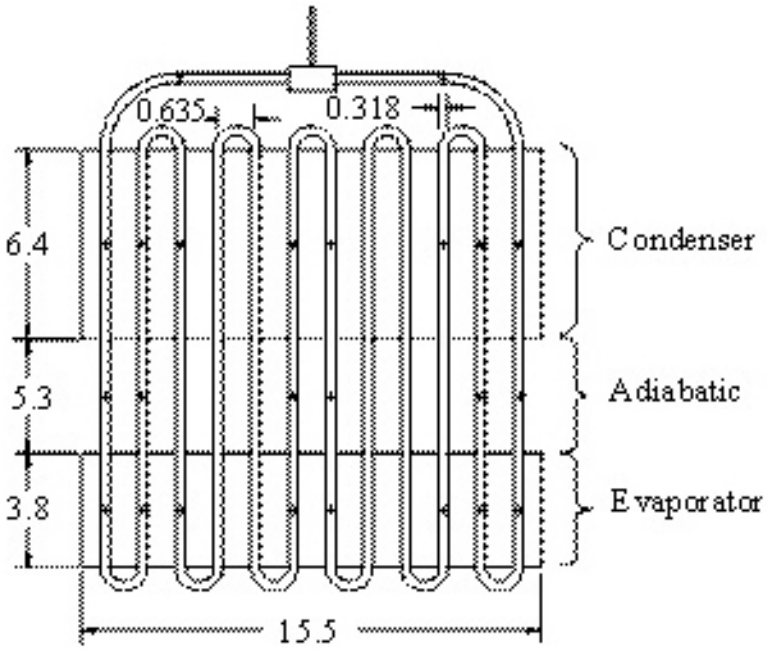

Figure 3.9. Drawings of OHPs with dimensions. Positions of thermocouples are indicated with crosses (Wilson, 2008a).

Setup and Procedure

A Tempco strip heater and a cooling block were attached to the evaporator and the condenser, respectively, using thermal paste to improve thermal conductivity. In Figure 3.10, the strip heater and cooling block used are shown. Electrically insulating cloth was attached to the strip heater to prevent unexpected shorting of the electrical

terminals. The OHP with the strip heater covered with its electric insulator and the cooling block positioned in the sample holder are shown in Figure 3.11. The power to the strip heater was supplied by a Staco 3PN501B voltage regulator. A Fluke 45 dual display multimeter was used to monitor the voltage supplied by the voltage regulator. Heavy water (D, 99%), purchased from Cambridge Isotope Laboratories, Inc., was used within the cooling block because heavy water has lower neutron attenuation coefficients to prevent obscuring the working fluids in the OHP. The heavy water was pumped through a heat exchanger connected to a Julabo F34/MD circulator to remove heat from the system. Thus, the heat exchanger acted as a thermal connector between the heavy water cooling loop and a regular water cooling bath.

(a) Strip heater

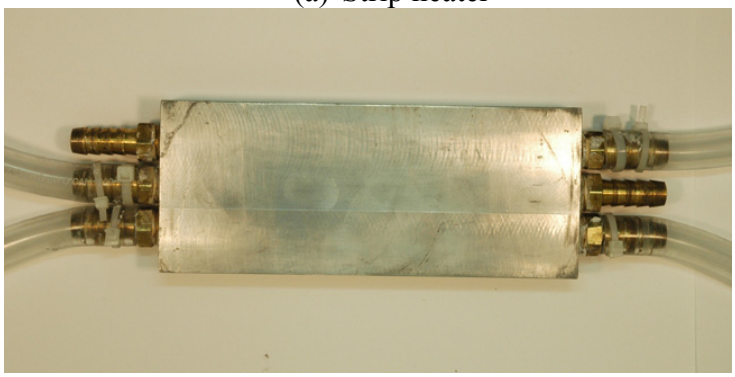

(b) Cooling block

Figure 3.10. Strip heater and cooling block used in the experiments.

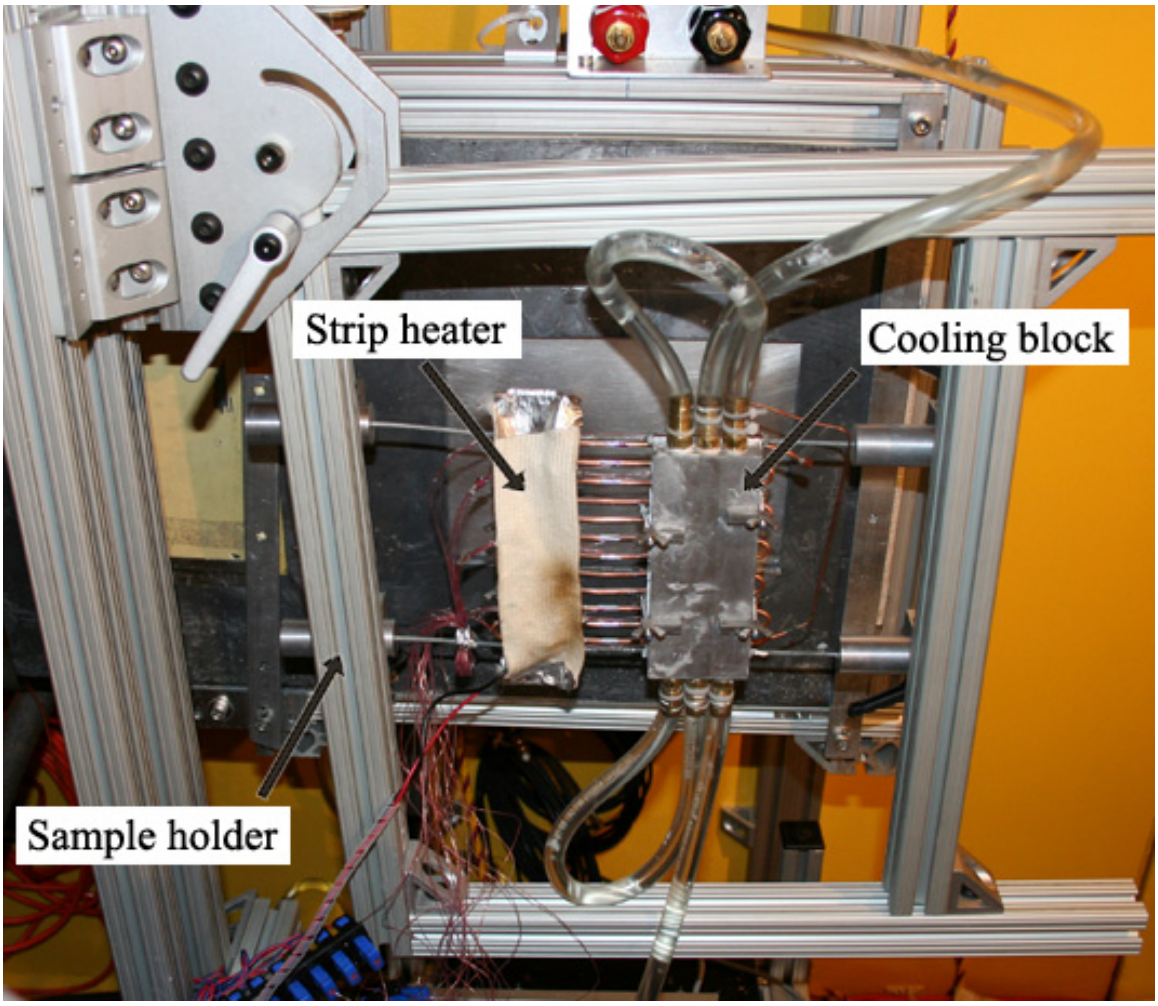

Figure 3.11. The OHP with cooling block and strip heat attached positioned on the sample holder. The strip heater was covered by an electric insulator.

To measure the temperature data, T type thermocouples were attached to the copper tubes. Positions of the thermocouples on the OHPs are shown in Figure 3.12. The temperature data was collected with a National Instruments SCXI-1600 data acquisition system. The OHPs were surrounded by an insulator of fiber glass, to isolate them thermally and to ensure that heat was exchanged only through the evaporator and condenser. The fiber glass was wrapped with aluminum foil to prevent any dispersing of activated fiber glass particles into the air. In Figure 3.13, a conceptual diagram of the experimental setup for heating and cooling the OHPs is shown.

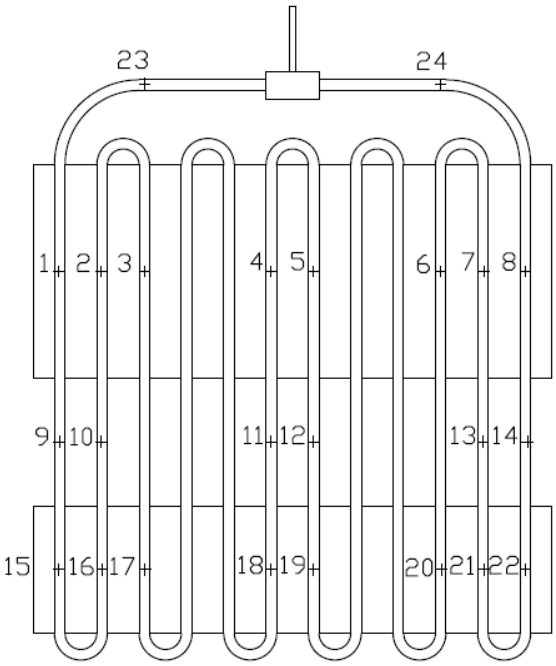

(a) Positions of thermocouples along with identification numbers. The crosses indicate the positions where the thermocouples were attached (Wilson, 2008a).

(b) Photo of an OHP with thermocouples attached.

Figure 3.12. Drawing and photo of OHP with thermocouples.

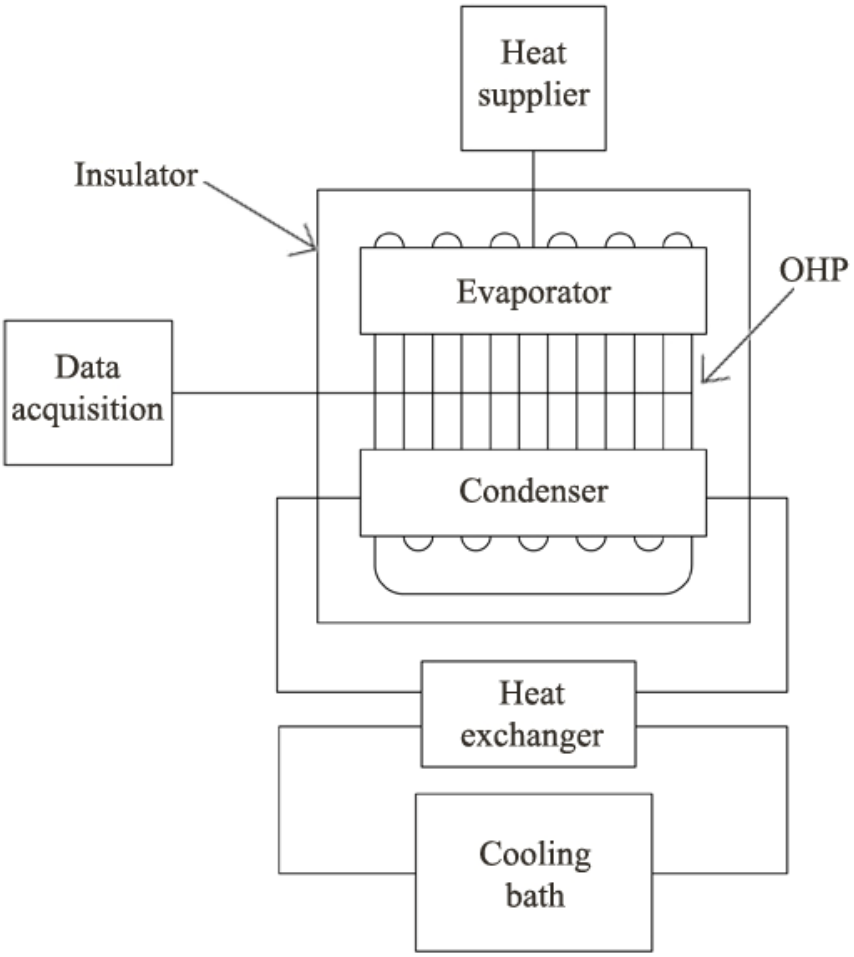

Figure 3.13. Conceptual diagram of the experimental setup for heating and cooling the OHPs

Figure 3.14 shows the OHP positioned on the sampled holder after the experimental setup was completed. Figure 3.15 shows a conceptual drawing of the completed experimental setup. The evaporator was on the right and the condenser was on the left in a view from the detector. The working fluid was allowed to be distributed naturally throughout the tubing and to achieve thermal equilibrium with the temperature set using the cooling bath.

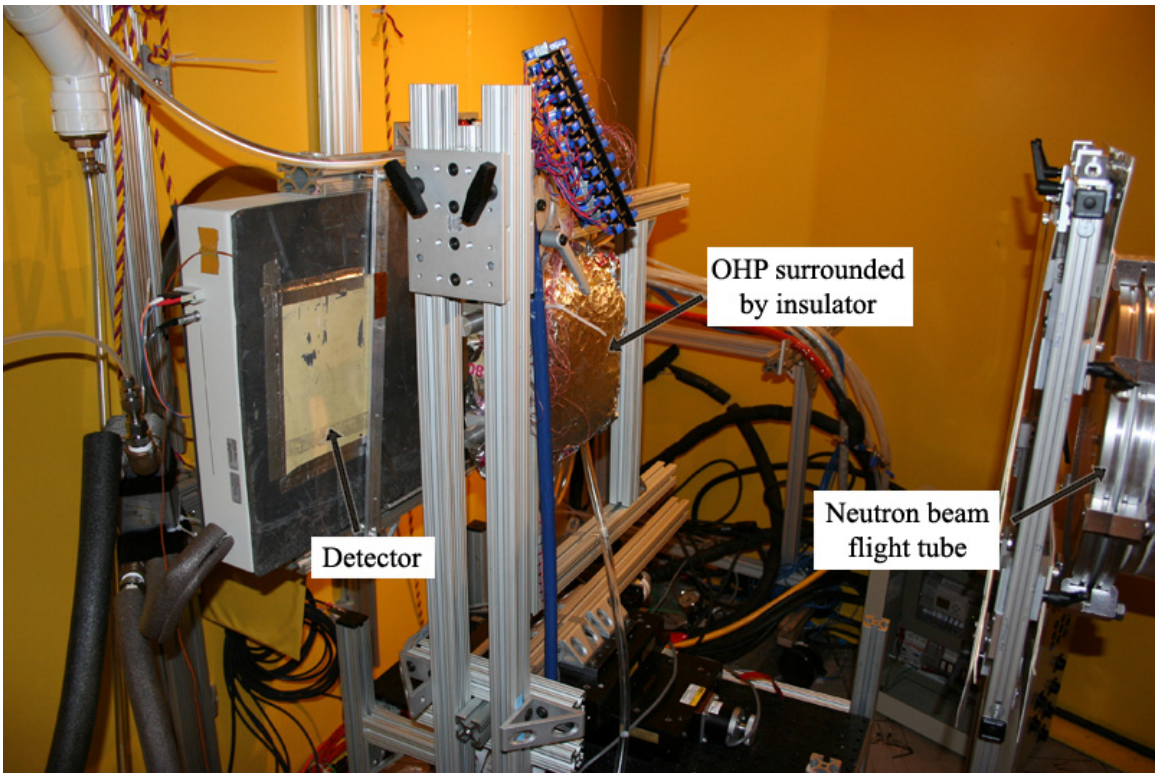

Figure 3.14. OHP positioned on the sample holder after experimental setup was completed.

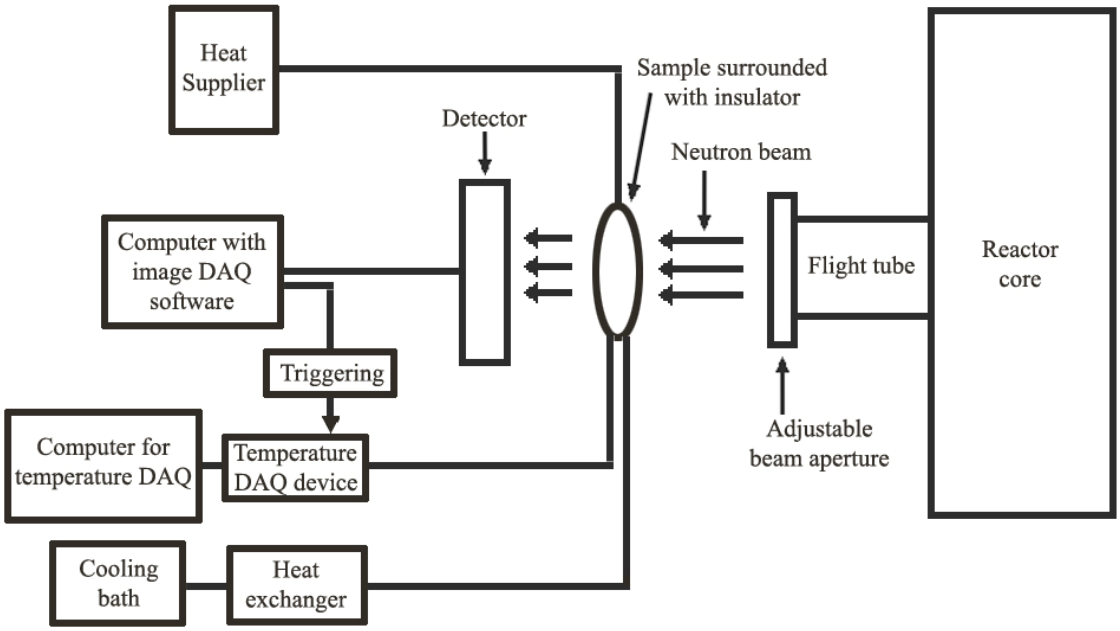

Figure 3.15. Conceptual drawing of the completed experimental setup.

The cooling bath temperature was regulated at 20 °C. The temperature sampling rate was 60 Hz for both water-OHP and acetone-OHP. The L/D ratio for the neutron beam was 300 with a total neutron rate of 3.3×10^7 n/s. The distance from the sample to the sensor was approximately 3 inches. A frame rate of 30 fps was used for image collection. The image data and temperature data were obtained with two separate computers. The image data and temperature data collection were synchronized in time by triggering the temperature DAQ using the image acquisition software.

There were two types of power input experiments: transient and steady-state power input. Transient power input tests were for observing the movement of liquid and temperature change immediately after the power input was increased or decreased. Between each transient test, steady-state power input tests were performed after the response of the OHPs stabilized. For steady-state power input tests, the power input was not changed. Table 3.2 shows the power input values and their corresponding image acquisition times for the water-OHP and the acetone-OHP.

Table 3.2. Heat inputs used for OHPs and the corresponding data acquisition times.

Water-OHP			Acetone-OHP		
Heat input (watt)	Image acquisition time (Sec)	Heat Input Type	Heat input (Watts)	Image acquisition time (Sec)	Heat Input Type
0	10	Steady-state	24	600	Transient
26	600	Transient	24	120	Steady-state
26	300	Steady-state	51	420	Transient
50	300	Transient	51	120	Steady-state
50	300	Steady-state	73	420	Transient
99	300	Transient	73	120	Steady-state
99	180	Steady-state			
149	300	Transient			
149	120	Steady-state			
197	180	Transient			
200	120	Steady-state			
297	120	Transient			
300	120	Steady-state			

Bright field images were collected for brightfield correction. With no sample in place, 100 images were collected and averaged to create a brightfield image. Darkfield correction was imbedded in image acquisition software and taken during a calibration procedure by NIST scientists, so, there was no need to collect the darkfield images.

Chapter 4 Analysis Methods

The total image intensity in a region where there is no moving fluid, such as vapor or liquid, changes with time or frame number. It is assumed that this is because of variations in the incident beam intensity. The reactor power changes slowly with time, changing the incident intensity. Image sequences show more rapid changes in intensity whose source is not currently known but is being investigated at NIST. To correct for this variation, a scaling correction was applied to the images analyzed. A monitor detector would be the ideal method of accounting for this variation but one is not installed at this facility. Thus, the following method was used to correct for this variation.

For this correction, a target intensity was first calculated. To find this target intensity a region of the image where there was no moving fluid was chosen. This region was called a 'no-fluid patch'. It is a rectangular region defined by four corner points. The target intensity was assigned as a 32 bit unsigned integer class in Matlab to prevent overflow. The target intensity was determined as the average value of the total intensity in the no-fluid patch for one of the early tests of a given heat pipe for a large number of frames, typically thousands of images. Each image file was opened, one after another and a median filter, with a 3 by 3 neighborhood, was applied to the no-fluid patch, and the sum of the intensity in all the pixels in the patch was calculated. After all files were filtered and summed, the average value of all the sum of intensity in the patch was determined.

Next, a flat field image was needed for flat field correction of the test images. A flat field image is one with no objects being radiographed which gives the system response including direct beam and detector nonuniformities. Dividing each test image by the flat field image removes these nonuniformities from the test images. A sequence of flat field images was taken on the Neutron Imaging Station before the experimental apparatus was placed in the beam. Only one set of flat field images was taken for an experimental session of about a week. Before averaging the images, a median filter with a 3 by 3 neighborhood was applied to all the flat field images individually. Then, an average image of all flat field images was made. The number of flat field images was 1000. The average flat field image had some zero intensity pixels around the periphery of the detector. These pixels were corrected by replacing the zero value with the average intensity of the surrounding pixels. None of these pixels were in areas subsequently used in the analysis.

Initial processing of the images was done by opening each in turn, processing and rewriting as a new Tiff file. After each image was opened, they were median filtered with 3 by 3 neighborhoods. The total intensity of the no-fluid patch in each image was obtained and the whole image multiplied by a factor such that the no-fluid patch had the target intensity obtained previously. After this, each image was rotated counterclockwise by 90°, as the files are written with the images rotated 90° from the actual test orientation. The images were then flat field corrected by dividing, pixel-by-pixel, by the 90° rotated average flat field image produced previously. To further reduce noise, a Wiener filter was next applied to each image. Processing was done with Matlab double

class variables. After this processing, each image was converted to16-bit unsigned integer class and saved in the16-bit TIFF format.

In order to accurately specify paths following the copper tubing in the neutron radiographs, an averaged image was used to eliminate noise without blurring with a filter. This eliminates information about the fluids in the tubing, but this information is not needed for determining the paths which are determined by the location of the copper tubing of the heat pipe. An averaged image was made by averaging several hundred consecutive images of the heat pipe of interest.

This average image was opened, and Matlab used to draw a path down the centerline of the heat pipe tubing by manually selecting arbitrary points placed at the center of the pipe with the computer mouse. Figure 4.1 shows a sample preliminary path. The circular markers are the points selected. Two adjacent path lines were made automatically with a Matlab m-file program made for this purpose. For the narrow tubing, the gaps between the three path lines are basically 1 pixel unit. At some points in curved areas primarily, points on the adjacent path lines were located in the same pixel. In this case, the gap was modified to have a 1.42 pixel distance to avoid locating two separate paths in the same pixel. Such a case is shown in Figure 4.2. In some instances the paths were unrealistically twisted and these were corrected manually. Figure 4.3 shows three path lines in a curved area after the adjacent two path lines were drawn automatically adjacent to the central path and modified manually. Next, two background paths were drawn on the images outside of the copper tubing around the length of the heat pipe. After finishing the drawing of all of the five paths, some additional placement corrections were done at some points. Figure 4.4 shows the five paths for a heat pipe.

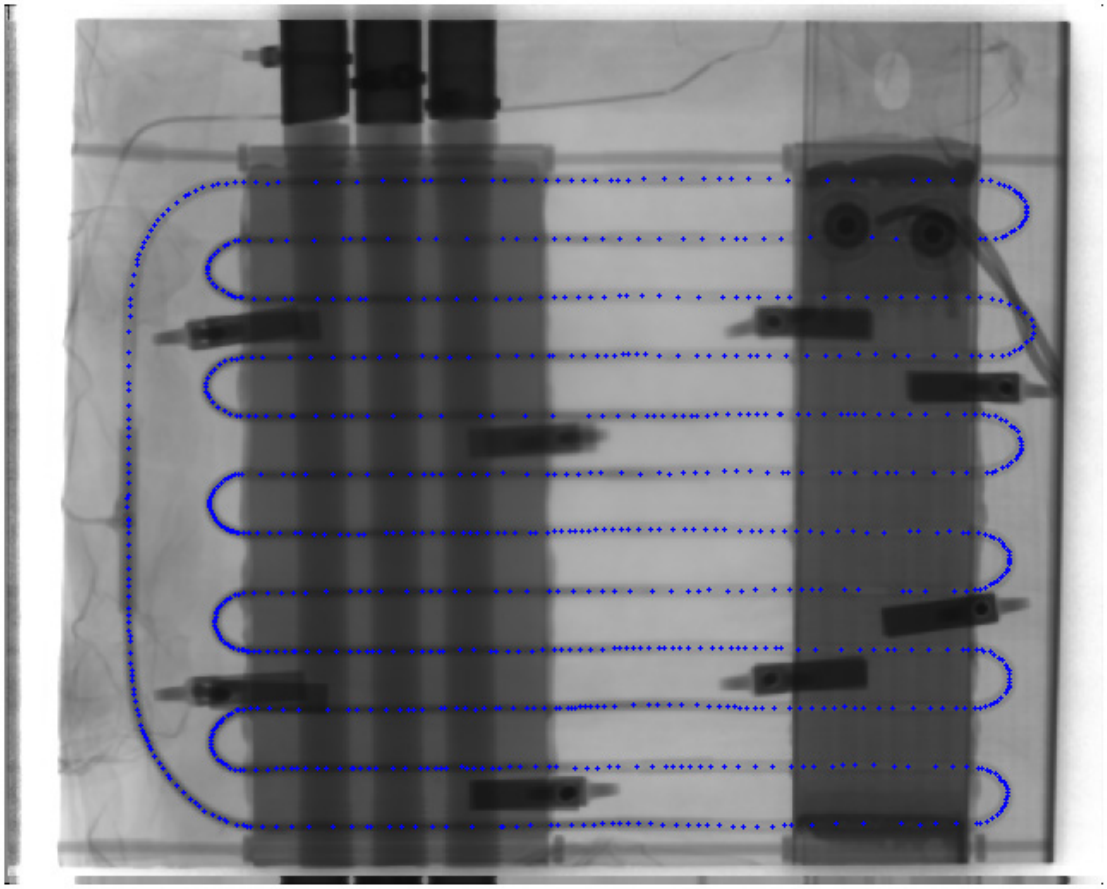

Figure 4.1. The points along the center of the pipe marked on an average reference image. The circular shaped dots are the points selected with the computer mouse.

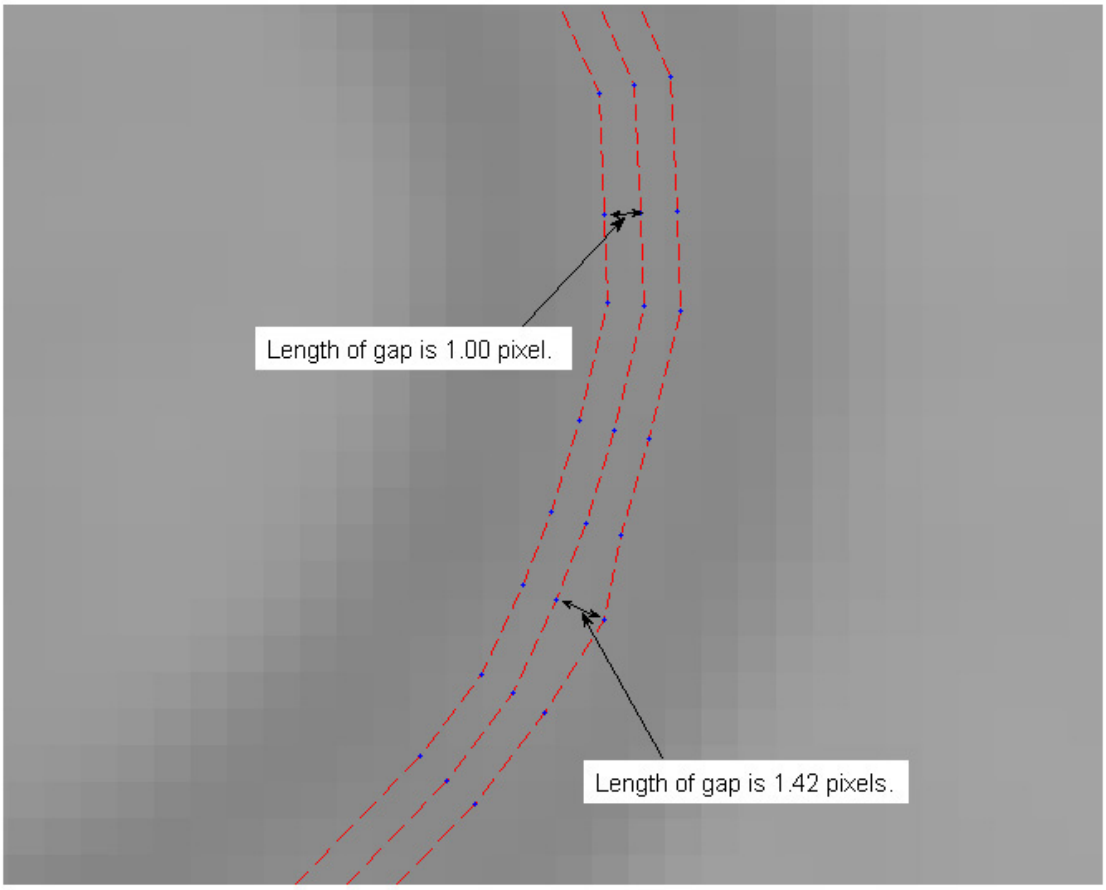

Figure 4.2. Close-up of image showing the length of the gap between corresponding points on each path in the copper tubing.

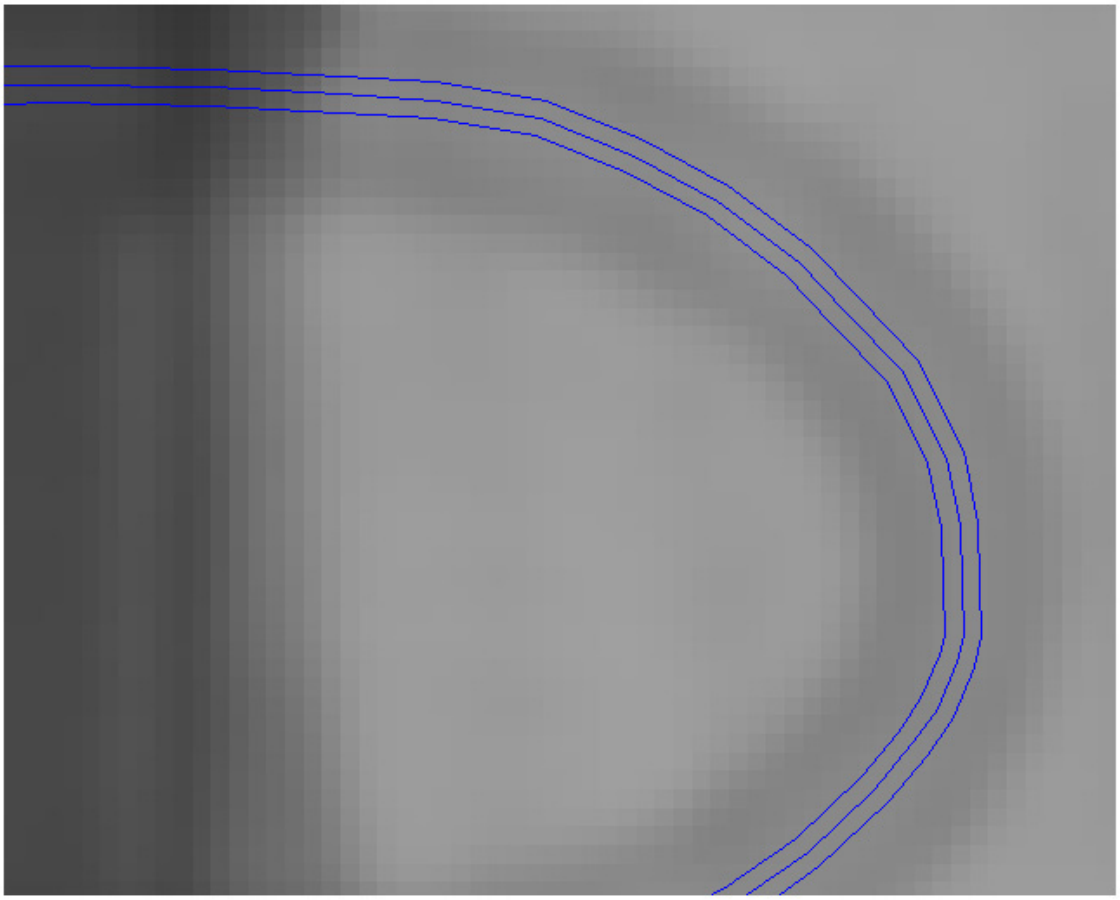

Figure 4.3. A section of an image showing three paths after the creation and modification of two path lines adjacent to the center path line.

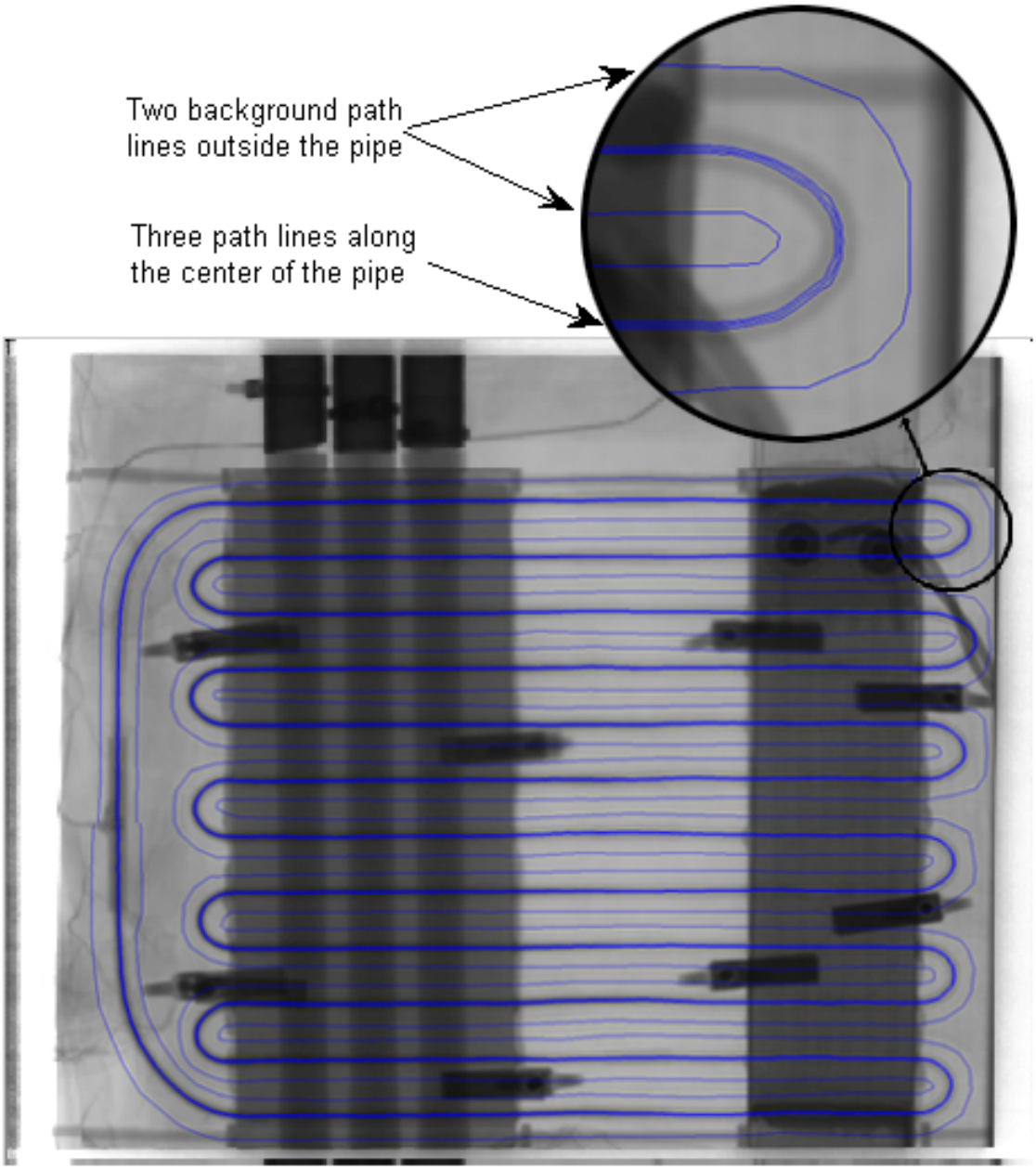

Figure 4.4. Image with the five path lines superimposed. The three central path lines are located inside the tubing and the outer two path lines are located outside the pipe on the image. The circular inset shows a magnified view better showing the three central path lines.

After completing the drawing of all five paths, the gaps between the original points in each path was filled with points, whose spacings were usually 1 pixel distance, by the interpolation method. Paths in curved areas were divided into three to five sections because points with indices corresponding to each other did not line up perpendicular to the path if the points were not added without first dividing the area into sections. The paths in different sections were then joined to create a continuous path around the whole heat pipe. Numbering of the paths is as follows: the three paths at center of pipe were labeled 1, 2, and 3, with 2 being the central path, and the two background paths outside of the tubing were labeled B1 and B2. The total numbers of coordinate points defining the paths are the same for each path. Placement of the path-defining coordinate points was confirmed by connecting points with the same index on each path with lines as shown in Figure 4.5. These line segments were used to confirm that the number of points was the same and that they were roughly perpendicular to the direction of the path at each position along the path. Path-defining points with the same index on each of the paths defined a position along the path for later processing. The central path (path 2) was used for determining distances along the heat pipe's fluid loop.

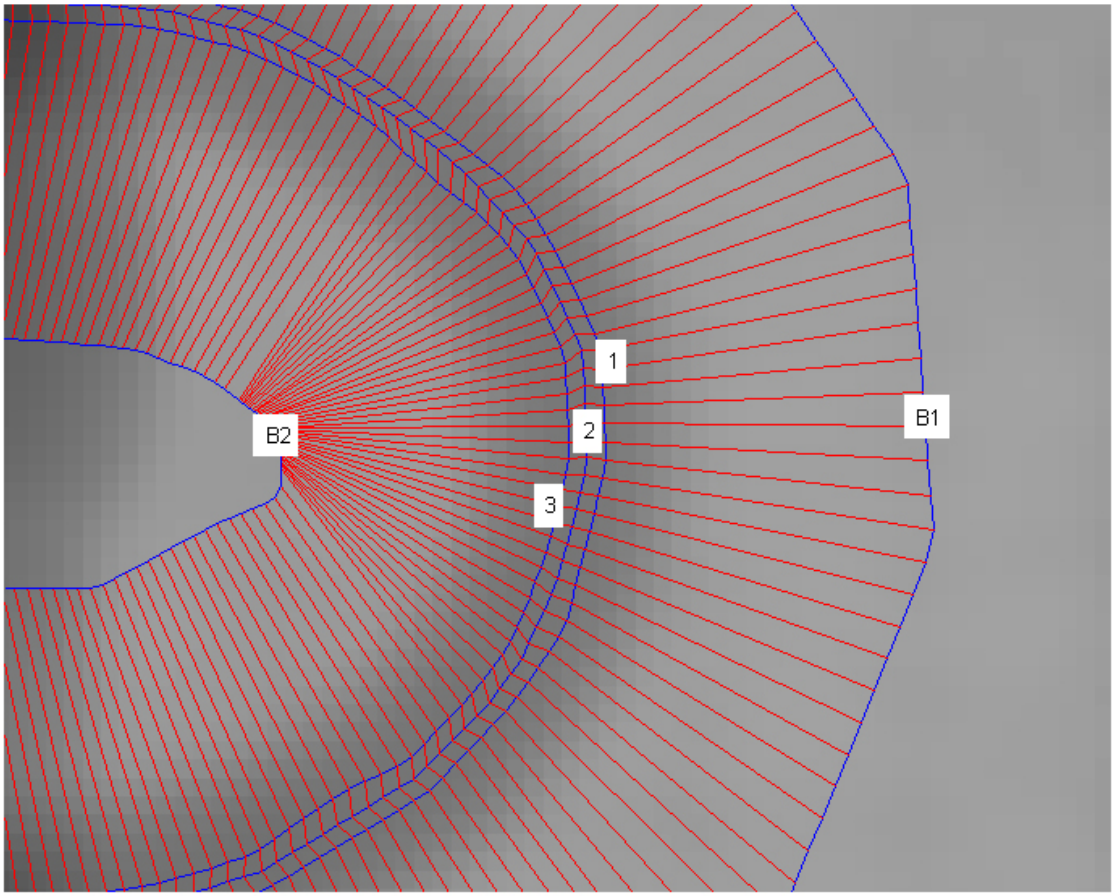

Figure 4.5. Close-up of an image with corresponding index points connected to one another. Labels give the path numbers used.

The intensity value of all the pixels corresponding to each point on the paths was next obtained. Among the five paths, the outer two ones are for background intensity. The two intensity values corresponding to each other at a certain position along the pipe are averaged to get the background intensity. The background intensity can be represented as

$$\begin{aligned} \mathrm{I_b} &= \frac{\mathrm{I_{b1}} + \mathrm{I_{b2}}}{2} = \left(\frac{1}{2}\right)\left(I_0 \exp\left[-\left(\mu_{ins} x_{ins} + \mu_{cb} x_{cb.b1}\right)\right] + I_0 \exp\left[-\left(\mu_{ins} x_{ins} + \mu_{cb} x_{cb.b2}\right)\right]\right) \\ &= I_0 \exp\left[-\left(\mu_{ins} x_{ins} + \mu_{cb} x_{cb.b}\right)\right] \end{aligned} \tag{4.1}$$

where I_b is the background intensity at a certain position, I_{b1} and I_{b2} are the background intensities from paths B1 and B2 at this position, respectively, I_0 is the intensity before attenuation, μ_{ins} and x_{ins} is the attenuation coefficient and the thickness of insulation materials respectively, $\mu_{cb.b1}$ and $x_{cb.b1}$ are the attenuation coefficient and the thickness of copper block at background path B1, respectively, and $\mu_{cb.b2}$ and $x_{cb.b2}$ are the attenuation coefficient and the thickness of copper block at background path B2, respectively. The values for the background intensities are based on the average image to reduce noise. At certain locations along the paths, only one of the two background paths could be used to obtain the background intensity due to a thermocouple wire or other object appearing that was not located in paths 1, 2, or 3 and thus making the intensity level there not representative of the true background. Although it was anticipated that the background level of intensity would be useful in further calculations, it was not subsequently used.

To calculate volume fractions of liquid and vapor at each position along the paths, the intensities of equivalent points along the three paths in the pipe were multiplied by one another. This was called 'intensity in'. The intensity reaching the detector to make this I_{in} value can be modeled as

$$\begin{aligned} I_{in} &= I_1 \times I_2 \times I_3 = I_0 \exp\left[-\left(\mu_{ins}x_{ins} + \mu_{cb}x_{cb1} + \mu_p x_{p1} + \mu_v f_{v1}x_1 + \mu_l f_{l1}x_1\right)\right] \\ &\times I_0 \exp\left[-\left(\mu_{ins}x_{ins} + \mu_{cb}x_{cb2} + \mu_p x_{p2} + \mu_v f_{v2}x_2 + \mu_l f_{l2}x_2\right)\right] \\ &\times I_0 \exp\left[-\left(\mu_{ins}x_{ins} + \mu_{cb}x_{cb3} + \mu_p x_{p3} + \mu_v f_{v3}x_3 + \mu_l f_{l3}x_3\right)\right] \end{aligned} \quad (4.2)$$

where I_1, I_2, and I_3 are the intensities at paths 1, 2, and 3 in the pipe, I_0 is the intensity before attenuation, μ_{ins}, μ_{cb}, μ_p, μ_v, and μ_l are the attenuation coefficients for the insulation material, copper block, heat pipe wall, vapor in the pipe and liquid in the pipe,

respectively, x_{ins}, x_{cb}, x_p, x_v, and x_l are the thickness of insulation material, copper block, heat pipe wall, vapor in the pipe and liquid in the pipe, respectively, and f_v and f_l are the volume fractions of vapor and liquid. The subscript numbers 1, 2, and 3 designate the path numbers. The distances x_1, x_2, and x_3 are the distances neutrons travel through the inside of the pipe at the locations of paths 1, 2, and 3, respectively, at each position along the paths. Note that the 'intensity in' does not mean the intensity in the pipe. It is just a term introduced to be convenient for calculation. The volume fractions are defined as

$$f_v = \frac{\int\int_{V\ t} v_v dV dt}{V\Delta t} \ . \tag{4.3}$$

Here V is the effective volume in the heat pipe seen by a pixel, v_v is the volume fraction of vapor at a point within the effective volume, t is time, and Δt is the time increment for which the detector accumulates neutrons for the pixel. A similar relation holds for f_l. Equation (4.3) states that the volume fraction is both spatially and temporally averaged.

It was assumed that $f_{l1}=f_{l2}=f_{l3}$ and $f_{v1}=f_{v2}=f_{v3}$. This assumption is justified by the slug flow observed in the heat pipes and the Bond number for the system. Then, Equation (4.2) becomes

$$\begin{aligned} \mathrm{I_{in}} &= \mathrm{I_1} \times \mathrm{I_2} \times \mathrm{I_3} \\ &= {I_0}^3 \exp[-(3\mu_{ins}x_{ins} + 3\mu_{cb}x_{cb} + \mu_p(x_{p1} + x_{p2} + x_{p3}) \\ &\qquad + \mu_v f_v(x_1 + x_2 + x_3) + \mu_l f_l(x_1 + x_2 + x_3))]. \end{aligned} \tag{4.4}$$

Secondly, the background intensity was cubed and called 'intensity out'.

$${I_b}^3 = \left(I_0 \exp\left[-\left(\mu_{ins}x_{ins} + \mu_{cb}x_{cb.b}\right)\right]\right)^3 = {I_0}^3 \exp\left[-\left(3\mu_{ins}x_{ins} + 3\mu_{cb}x_{cb.b}\right)\right] \tag{4.5}$$

Like ‘intensity in’ is just a concept introduced to be convenient for calculation, ‘intensity out’ is a term made to the purpose of calculation from background intensity, not the background intensity itself.

The sum of vapor volume fraction and liquid volume fraction is one:

$$f_v + f_l = 1 \tag{4.6}$$

Then we can write Equation (4.4) as

$$\ln(I_{in}) = 3\ln(I_o) - \begin{bmatrix} 3\mu_{ins}x_{ins} + 3\mu_{cb}x_{cb} + \mu_p(x_{p1} + x_{p2} + x_{p3}) \\ + \mu_v f_v(x_1 + x_2 + x_3) + \mu_l(1 - f_v)(x_1 + x_2 + x_3) \end{bmatrix} \tag{4.7}$$

The only changing value for a particular position in Equation (4.7) is f_v and it can be seen that $\ln(I_{in})$ depends on f_v. Thus, $\ln(I_{in})$ can be used as a measure of the volume fraction at a certain position along the heat pipe for a certain frame. All the volume fraction values for all positions along the pipe for all frames were calculated using the method above.

At this stage we have time series intensity data for each position along the heat pipe path. This data was filtered to remove noise in the data. The filter applied was a simple running average:

$$x_{i,filtered} = \frac{x_{i-1} + x_i + x_{i+1}}{3} \tag{4.8}$$

The number of values in the window for the running average was 3. The filter was applied to all the frames in the time sequence. The values of the first and last points in time were just divided by 2 because they just have one adjacent value. Figure 4.6 shows an example of the effect of filtering on the time sequence at one position.

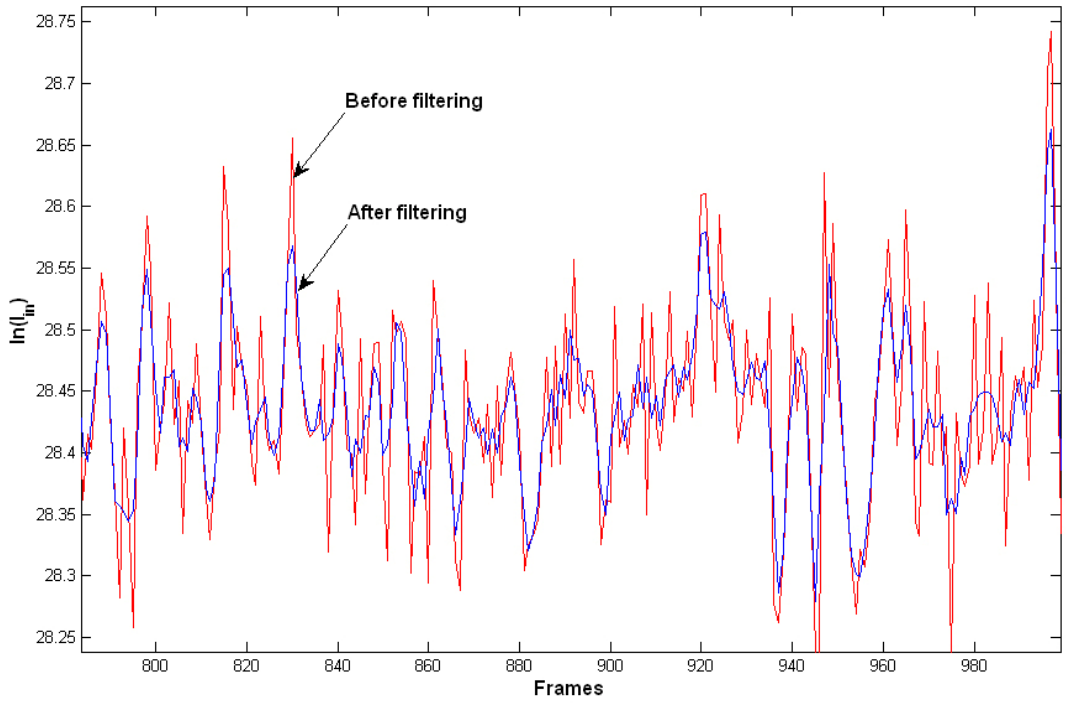

Figure 4.6. Time sequence data at one location on the heat pipe path before and after filtering.

Before further proceeding, two terms were introduced for computation. The value of I_{in} was called the 'vapor intensity' or I_v when vapor fully occupies a certain position in the pipe. When liquid fully occupies the pipe at a certain position, its value was called the 'liquid intensity' or I_l. The value of I_{in} was called just 'intensity' when vapor and liquid coexisted at a location over the time sampled for a frame. To determine the average vapor and liquid intensities at a certain position the 30 maximum and 30 minimum values of a time sequence were chosen at the position. Figure 4.7 shows the 30 maximum and 30 minimum values that were selected for a position along the path. Then, 15 intensity values before and 15 intensity values after each of the 30 maximum values chosen were also selected. Figure 4.8 shows a few sets of 15 intensity values before and 15 intensity values after the same maximum values. After this, the average intensity of all the selected

values was taken as the 'vapor intensity' for that position. This process was repeated for the 30 minimum points in a time sequence to obtain the average 'liquid intensity' for the same position. The red and green lines in Figure 4.7 show the resulting vapor and liquid intensity values resulting for that position. This method was repeated for all the positions along the heat pipe path.

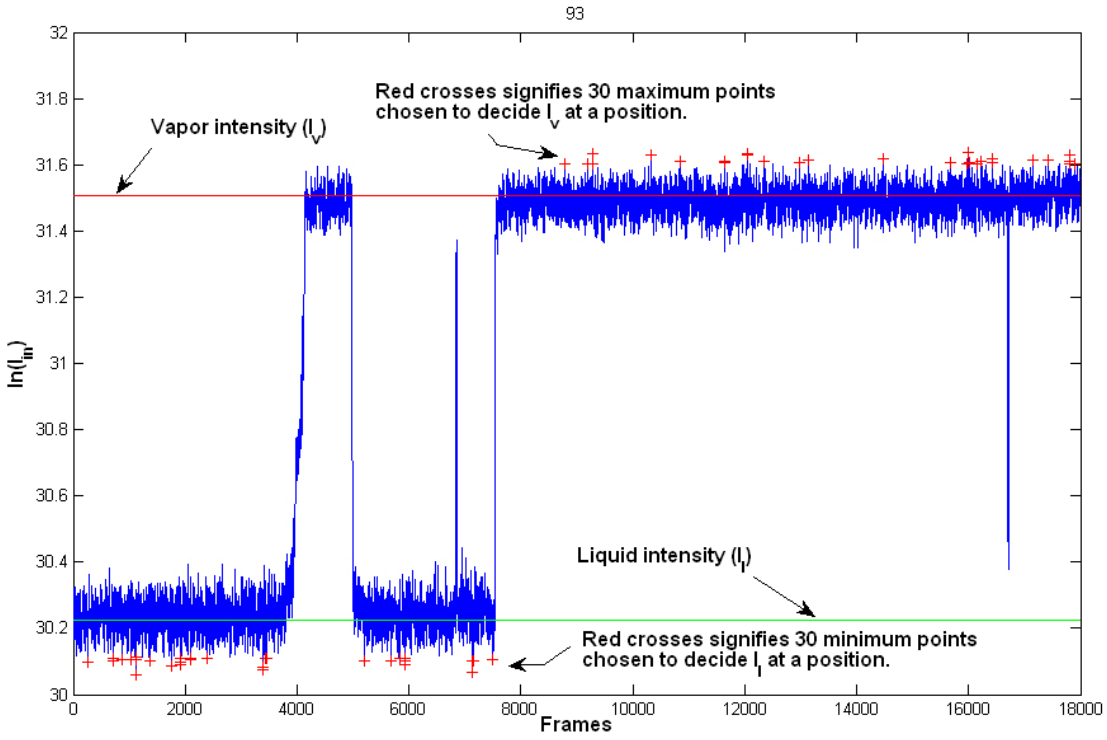

Figure 4.7. 30 maximum and 30 minimum points to decide I_v and I_l at one position. The red crosses are the points chosen.

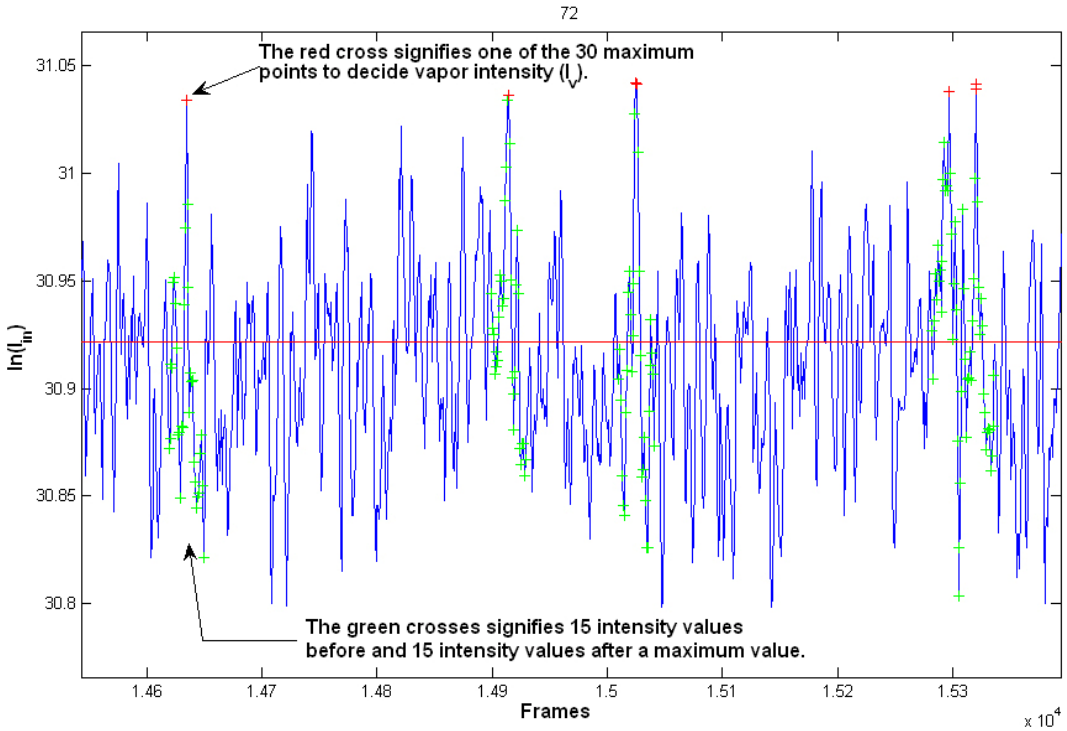

Figure 4.8. The 15 intensity values before and 15 intensity values after the maximum values shown with green crosses. The maximum values are shown with red crosses.

To confirm the liquid and vapor intensity values computed as valid, the following two ratios were computed:

$$\frac{\ln(I_{\max})-\ln(I_v)}{\ln(I_{\max})-\ln(I_{\min})}, \tag{4.9}$$

$$\frac{\ln(I_l)-\ln(I_{\min})}{\ln(I_{\max})-\ln(I_{\min})}. \tag{4.10}$$

I_{max} and I_{min} are the maximum and minimum intensities in the data set and I_v and I_l are the liquid and vapor intensities determined by the averaging. Both ratios had to be less than 0.14 to be considered valid. The value 0.14 was chosen based on experience in working with the data. These terms are illustrated in Figure 4.9 with data illustrating a case where the initial value of I_v was judged not valid and the initial value of I_l was judged valid by this criterion.

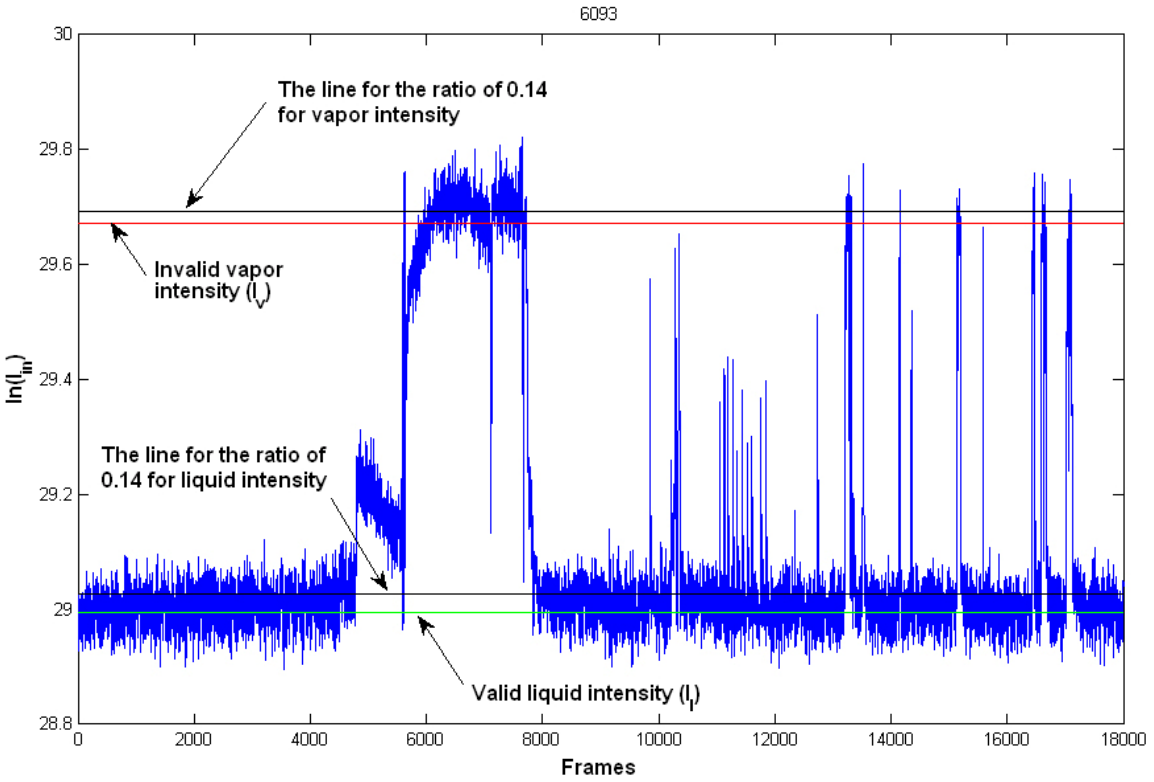

Figure 4.9. Time sequence data at one location that has an invalid I_v, the red line below the ratio of 0.14, the upper black line, and a valid I_l, the green line under the ratio of 0.14, the lower black line.

For the positions where the data were not judged to be valid, additional processes were needed. Each position that had invalid data was examined in turn and averaging range parameters were set manually. The range parameters set the ranges where data was included in averages to use for I_v and I_l. The range parameters were named I_A for the vapor, and I_B for the liquid for convenience. All data values above I_A were averaged to determine I_v and all data values below I_B were averaged to determine I_l. Figure 4.10 shows a data set with initially invalid I_v and valid I_l values with the range parameter I_A for I_v and a new I_v value. The new I_v was calculated by averaging all data values above I_A.

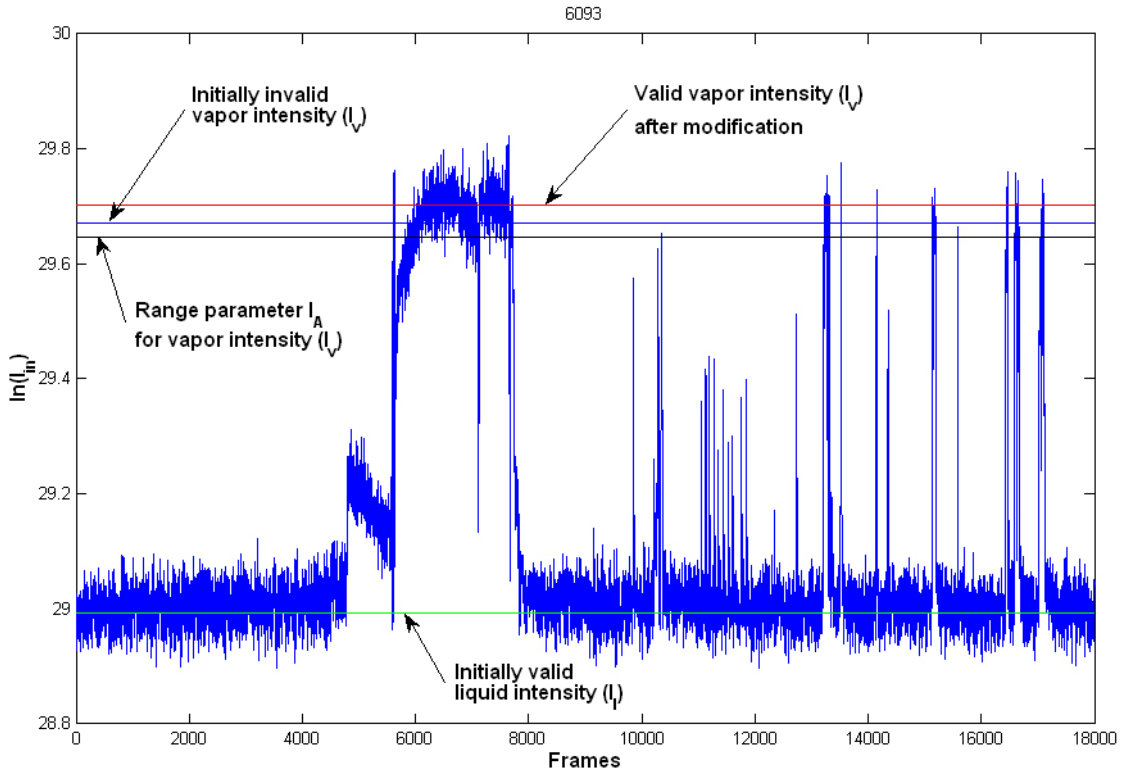

Figure 4.10. Time sequence data at one location that has an initially invalid I_v, the blue line, a range parameter I_A for I_v, the black line, and a new I_v, the red line and a initially valid I_l, the green line.

Although valid intensity values for pure vapor and liquid were obtained for most positions with these two methods, they were not valid for some positions in the heat pipe. This was because there were sometimes positions where the liquid or vapor did not move at all. These were called stagnant positions. For a position where only liquid was present, the value of I_l was computed as the average of the observed intensities and a value of I_v was assigned based on the average difference between I_v and I_l. For positions where only vapor was present, the opposite was done. I_v was computed as the average of the observed intensities and a value of I_l assigned from the average difference. In order to calculate I_C, the difference between the logarithms of the vapor and liquid intensities, we make use of

$$\ln(I_v) = 3\ln(I_o) - \left[3\mu_{ins}x_{ins} + 3\mu_{cb}x_{cb} + \mu_p(x_{p1} + x_{p2} + x_{p3}) + \mu_v(x_1 + x_2 + x_3)\right] \quad (4.11)$$

when f_v is 1 and,

$$\ln(I_l) = 3\ln(I_o) - \left[3\mu_{ins}x_{ins} + 3\mu_{cb}x_{cb} + \mu_p(x_{p1} + x_{p2} + x_{p3}) + \mu_l(x_1 + x_2 + x_3)\right] \quad (4.12)$$

when f_v is 0. Then,

$$I_C = \ln(I_v) - \ln(I_l) = (\mu_l - \mu_v)(x_1 + x_2 + x_3) \quad (4.13)$$

This shows that I_C should be constant regardless of position, if the attenuation coefficients of liquid and vapor and the tube thicknesses are constant along the path. The value of I_C was computed for all positions as shown in Figure 4.11. Here zero values are the stagnant or nearly stagnant positions where both I_v and I_l cannot be determined by the prior methods. It can be seen that I_C was not a constant value for the other points. This is probably due to a variety of factors. The locations of the pixels across the tubing varied from position to position, giving some variation in the thickness (the x_i in Equation 4.13). It can also be seen in Figure 4.11 that there is a systematic variation in I_c designated by the arrows. The peaks in the plot all correspond to the turns in the tubing. Caliper measurements confirmed that the bending of the tubing to make the turns results in a slight thickening of the tubing in the direction of radiographic projection (and thinning in the plane of the heat pipe). Thus, the two average I_C values were calculated; one for the turns and, the other for the straight sections.

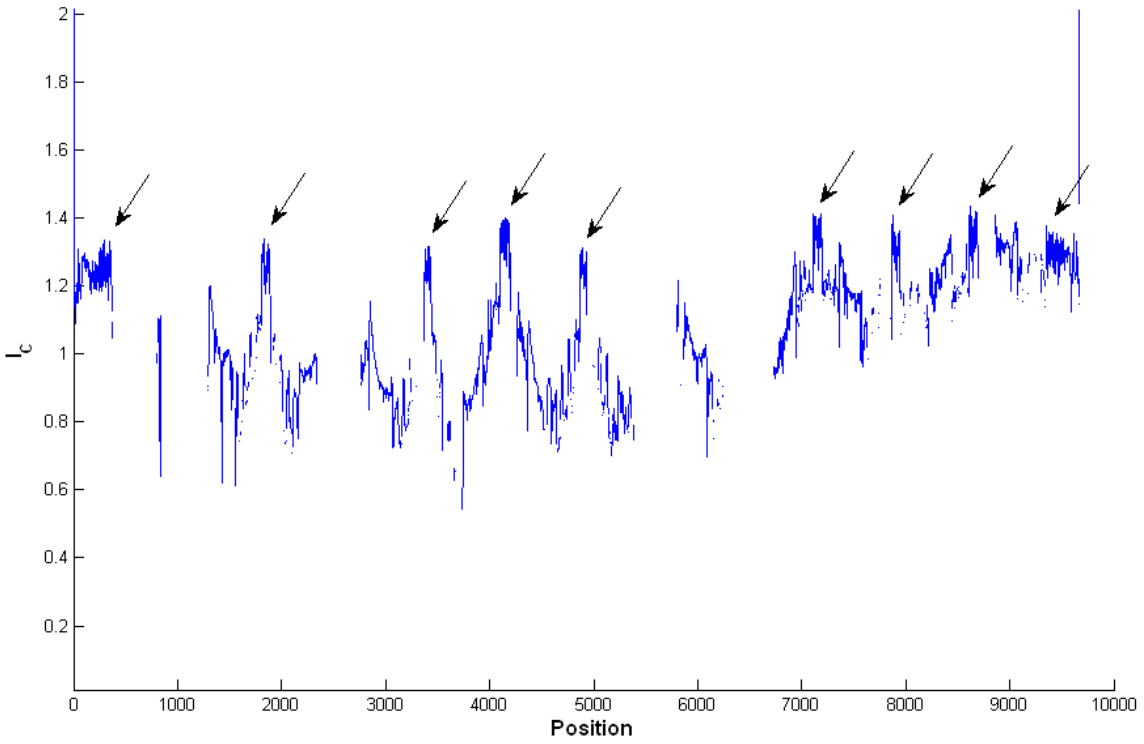

Figure 4.11. I_C data plotted according to the position along the path. The peaks indicated by arrows are the I_C data occurred systematically.

The positions whose I_C in Figure 4.11 are zero are stagnant positions. Their states, i.e., fully vapor or liquid, were determined by visual observation. At stagnant positions, when the position was fully occupied by vapor, vapor intensity values were set to the average intensity of the data at those positions. Then, liquid intensity was calculated using Equation (4.13). When the position was fully occupied by liquid, liquid intensity values were set to the average intensity of the data at those positions. Then, vapor intensity was calculated using Equation (4.13). In those positions, I_A and I_B were not further used.

The oscillating heat pipe consists of evaporator, condenser, and adiabatic regions. To determine which path positions belonged to which region a reference image, i.e., an average image of all images in a particular test, was opened in PhotoShop software and

the condenser, evaporator, and adiabatic regions were determined and three mask images created, one for each region. In the mask images a value of 1 was assigned to pixels within the region defined by that mask and a value of 0 to pixels outside that region. Figure 4.12 shows the reference image divided into the 3 regions. The mask images were used for separating the data from the three regions in later processing.

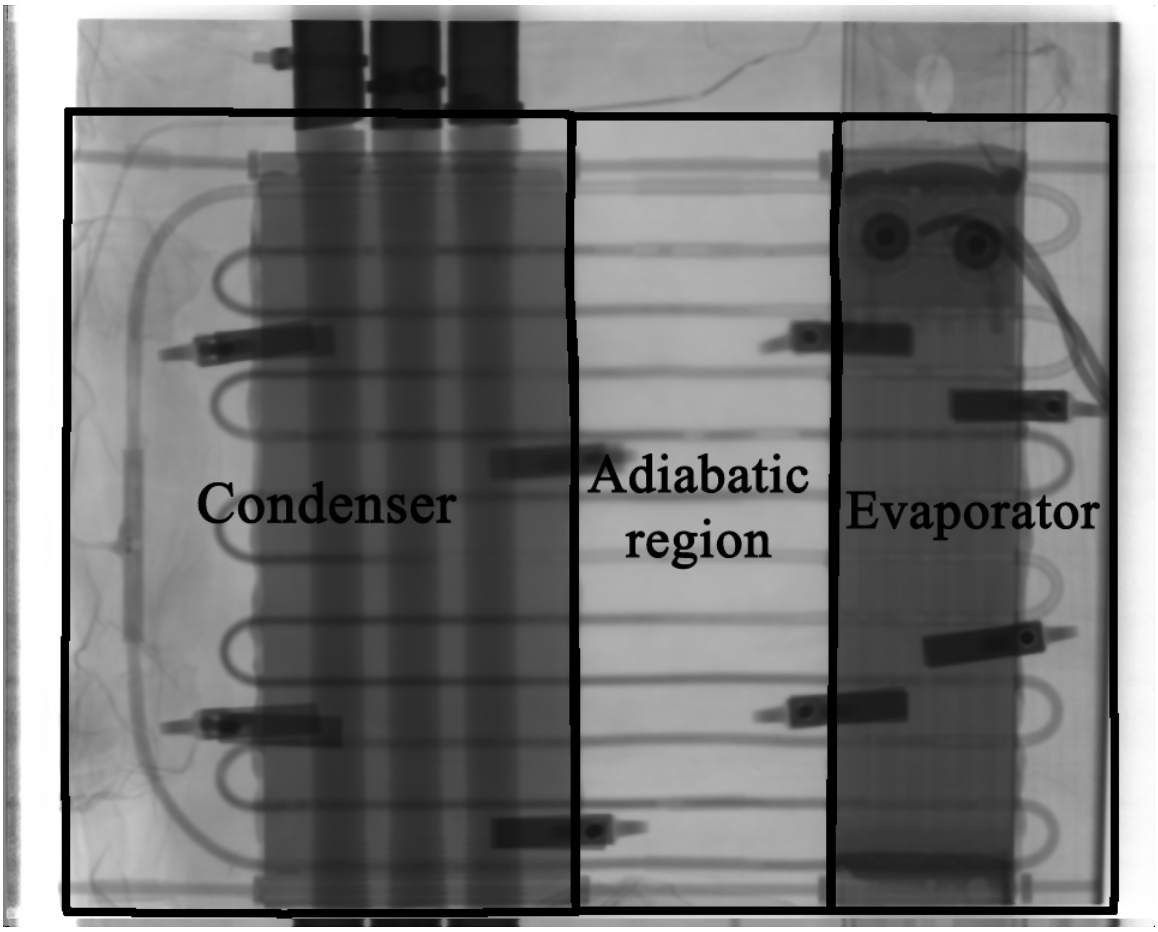

Figure 4.12. Average image of an oscillating heat pipe divided into regions.

The distance between the positions on the path line was based on the measurement of distance between the points on the center line, i.e., path number 2, among the five path lines. The path distance occupied by a position along the path, Δs_i,

was computed as the distance between the midpoint to the previous path position and the midpoint to the next path position using

$$\Delta s_i = \frac{1}{2}\sqrt{(x_i - x_{i-1})^2 + (y_i - y_{i-1})^2} + \frac{1}{2}\sqrt{(x_{i+1} - x_i)^2 + (y_{i+1} - y_i)^2} \tag{4.14}$$

Next, the volume fraction of vapor and liquid at each position needed to be calculated. We begin with Equation (4.2) (or Equation (4.4)), which models the parameter I_{in} and contains the volume fractions f_v and f_l. It is assumed that the volume fractions at a given position are the same for all three paths, $f_{l1}=f_{l2}=f_{l3}$ and $f_{v1}=f_{v2}=f_{v3}$. This assumption is justified by the Bond number of the system

$$Bo = \frac{(\rho_l - \rho_v)gD^2}{\sigma} \tag{4.15}$$

where σ is the surface tension, g is the gravitational acceleration, ρ_v and ρ_l are the vapor and liquid densities, and D is the inside diameter of the tube. When the Bond number is below 4.0, surface tension forces dominate the gravity forces and the liquid forms slugs which remain while the fluids are flowing. For this system the Bond number shown in Figure 4.13 is below 4.0 for temperatures seen in this work (Wilson, 2008a) and slug flow is confirmed by visual observation of the data.

We also make the substitutions $x_1+x_2+x_3=x$, $x_{cb1}+x_{cb2}+x_{cb3}=x_{cb}$, and $x_{p1}+x_{p2}+x_{p3}=x_p$. These substitutions replace neutron path lengths on the individual paths with a collective distance which is the sum for the three paths through the inside of the tube, the copper block, and the pipe wall. Making these substitutions in Equation (4.4) gives

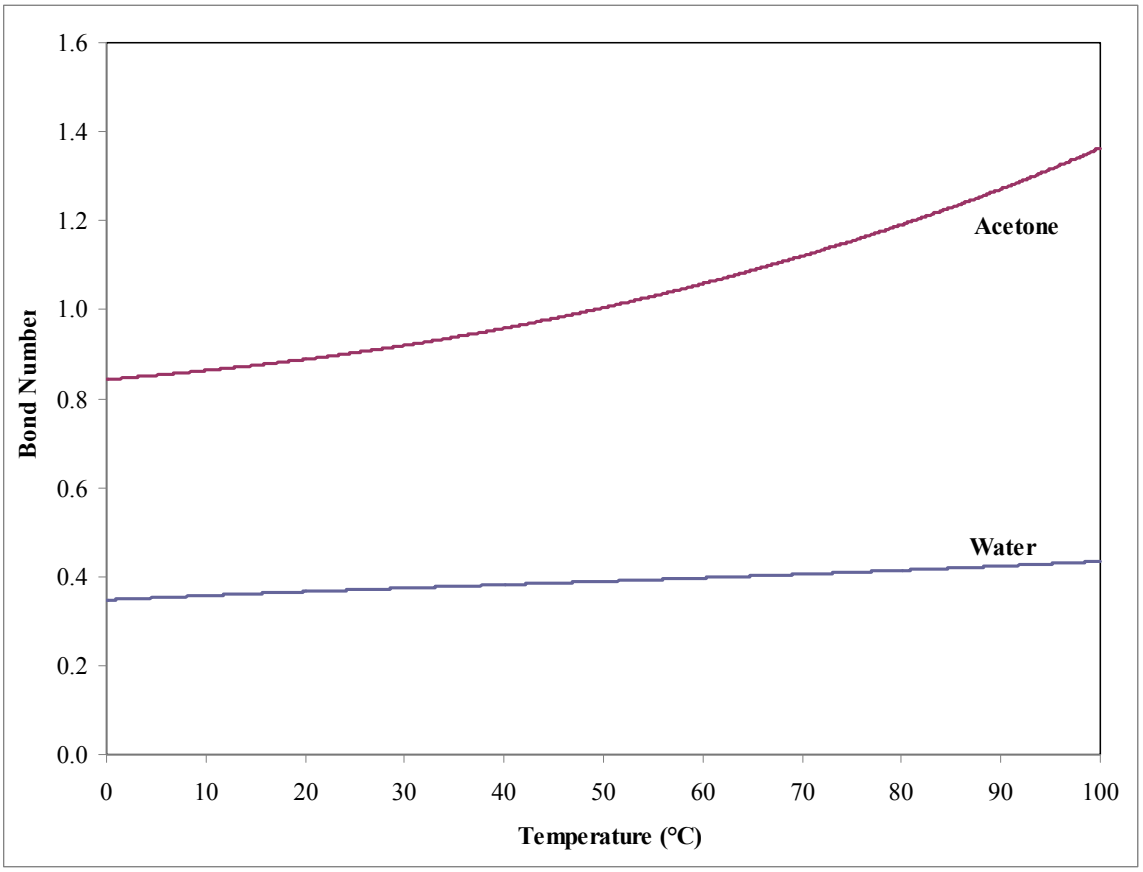

Figure 4.13. Bond number for water and acetone with temperature (Wilson, 2008a) showing that all bond numbers in these studies are below 4.0.

$$
\begin{aligned}
\mathrm{I}_{\mathrm{in}} &= I_0{}^3 \exp[-(3\mu_{ins}x_{ins} + \mu_{cb}x_{cb} + \mu_p x_p + \mu_v f_v x + \mu_l f_l x)] \\
&= I_0{}^3 \exp[-(3\mu_{ins}x_{ins} + \mu_{cb}x_{cb} + \mu_p x_p + \mu_v f_v x + \mu_l (1-f_v)x)] \\
&= I_0{}^3 \exp[-(3\mu_{ins}x_{ins} + \mu_{cb}x_{cb} + \mu_p x_p + f_v(\mu_v x - \mu_l x) + \mu_l x)]
\end{aligned}
\tag{4.16}
$$

When $f_v = 1$ we have the vapor intensity

$$
\mathrm{I}_{\mathrm{v}} = I_0{}^3 \exp[-(3\mu_{ins}x_{ins} + \mu_{cb}x_{cb} + \mu_p x_p + \mu_v x)] \tag{4.17}
$$

and when, f_v=0 we have the liquid intensity

$$
\mathrm{I}_{\mathrm{l}} = I_0{}^3 \exp[-(3\mu_{ins}x_{ins} + \mu_{cb}x_{cb} + \mu_p x_p + \mu_l x)] \tag{4.18}
$$

Using Equations (4.16), (4.17), and (4.18), we can then determine the volume fraction of vapor at a position along the path with the ratio

$$
f_v = \frac{\ln(I_{in}) - \ln(I_l)}{\ln(I_v) - \ln(I_l)}. \tag{4.19}
$$

Then, f_l is calculated as 1-f_v.

Next volume fractions characterizing the whole heat pipe volume, and the evaporator, condenser, and adiabatic regions were computed. The incremental volume of the pipe at a certain position, i, was calculated using

$$
\Delta V_i = A \times \Delta s_i \tag{4.20}
$$

where ΔV_i is the fractional volume of the pipe at a i^{th} position, A is the cross section area of the pipe, and Δs_i is the path length associated with the i^{th} position. The volume fraction of vapor and liquid at a certain position are thus expressed as

$$
\Delta V_{v,i} = A \times \Delta s_i \times f_{v,i} \tag{4.21}
$$

$$\Delta V_{l,i} = A \times \Delta s_i \times f_{l,i} \tag{4.22}$$

where $\Delta V_{v,i}$ is the volume increment of vapor at the i^{th} position, $\Delta V_{l,i}$ is the volume increment of liquid at the i^{th} position, $f_{v,i}$ is the volume fraction of vapor at the i^{th} position, and $f_{l,i}$ is the volume fraction of liquid at the i^{th} position.

With the volume increments, the volume fraction of vapor and liquid in the three regions of the heat pipe were computed with

$$F_{v,ee} = \frac{\text{Volume of vapor in evaporator}}{\text{Volume of evaporator}} = \frac{\sum_i A\Delta s_{e,i} f_{v,i}}{\sum_i A\Delta s_{e,i}} = \frac{\sum_i \Delta s_{e,i} f_{v,i}}{\sum_i \Delta s_{e,i}} \tag{4.23}$$

$$F_{l,ee} = \frac{\text{Volume of liquid in evaporator}}{\text{Volume of evaporator}} = \frac{\sum_i A\Delta s_{e,i} f_{l,i}}{\sum_i A\Delta s_{e,i}} = \frac{\sum_i \Delta s_{e,i} f_{l,i}}{\sum_i \Delta s_{e,i}} \tag{4.24}$$

$$F_{v,cc} = \frac{\text{Volume of vapor in condenser}}{\text{Volume of condenser}} = \frac{\sum_i A\Delta s_{c,i} f_{v,i}}{\sum_i A\Delta s_{c,i}} = \frac{\sum_i \Delta s_{c,i} f_{v,i}}{\sum_i \Delta s_{c,i}} \tag{4.25}$$

$$F_{l,cc} = \frac{\text{Volume of liquid in condenser}}{\text{Volume of condenser}} = \frac{\sum_i A\Delta s_{c,i} f_{l,i}}{\sum_i A\Delta s_{c,i}} = \frac{\sum_i \Delta s_{c,i} f_{l,i}}{\sum_i \Delta s_{c,i}} \tag{4.26}$$

$$F_{v,aa} = \frac{\text{Volume of vapor in adiabatic region}}{\text{Volume of adabatic region}} = \frac{\sum_i A\Delta s_{a,i} f_{v,i}}{\sum_i A\Delta s_{a,i}} = \frac{\sum_i \Delta s_{a,i} f_{v,i}}{\sum_i \Delta s_{a,i}} \tag{4.27}$$

$$F_{l,aa} = \frac{\text{Volume of liquid in adiabatic region}}{\text{Volume of adabatic region}} = \frac{\sum_i A\Delta s_{a,i} f_{l,i}}{\sum_i A\Delta s_{a,i}} = \frac{\sum_i \Delta s_{a,i} f_{l,i}}{\sum_i \Delta s_{a,i}} \tag{4.28}$$

Here subscripts *e*, *c*, and *a* stand for path positions along the evaporator, condenser, and adiabatic regions, respectively. Key in these equations is the assumption that the liquid and vapor volume fractions for each of the three paths inside the pipe at a given location along the path will be the same and thus they can be summed as in Equation (4.4). The Bond number and visual observations of the data support this assumption.

In addition, it was of interest to compute the ratios of the vapor and liquid volumes in the different regions to the volume of the entire heat pipe. These were computed as

$$F_{v,et} = \frac{\text{Volume of vapor in evaporator}}{\text{Volume of entire pipe}} = \frac{\sum_i A\Delta s_{e,i} f_{v,i}}{\sum_i A\Delta s_i} = \frac{\sum_i \Delta s_{e,i} f_{v,i}}{\sum_i \Delta s_i} \tag{4.29}$$

$$F_{l,et} = \frac{\text{Volume of liquid in evaporator}}{\text{Volume of entire pipe}} = \frac{\sum_i A\Delta s_{e,i} f_{l,i}}{\sum_i A\Delta s_i} = \frac{\sum_i \Delta s_{e,i} f_{l,i}}{\sum_i \Delta s_i} \tag{4.30}$$

$$F_{v,ct} = \frac{\text{Volume of vapor in condenser}}{\text{Volume of entire pipe}} = \frac{\sum_i A\Delta s_{c,i} f_{v,i}}{\sum_i A\Delta s_i} = \frac{\sum_i \Delta s_{c,i} f_{v,i}}{\sum_i \Delta s_i} \tag{4.31}$$

$$F_{l,ct} = \frac{\text{Volume of liquid in condenser}}{\text{Volume of entire pipe}} = \frac{\sum_i A\Delta s_{c,i} f_{l,i}}{\sum_i A\Delta s_i} = \frac{\sum_i \Delta s_{c,i} f_{l,i}}{\sum_i \Delta s_i} \tag{4.32}$$

$$F_{v,at} = \frac{\text{Volume of vapor in adiabatic region}}{\text{Volume of entire pipe}} = \frac{\sum_i A\Delta s_{a,i} f_{v,i}}{\sum_i A\Delta s_i} = \frac{\sum_i \Delta s_{a,i} f_{v,i}}{\sum_i \Delta s_i} \tag{4.33}$$

$$F_{l,at} = \frac{\text{Volume of liquid in adiabatic region}}{\text{Volume of entire pipe}} = \frac{\sum_i A\Delta s_{a,i} f_{l,i}}{\sum_i A\Delta s_i} = \frac{\sum_i \Delta s_{a,i} f_{l,i}}{\sum_i \Delta s_i} \tag{4.34}$$

Finally, the ratios of the volume of vapor and liquid in the evaporator, condenser, and adiabatic regions to the volume of vapor in entire heat pipe were calculated as

$$R_{v,et} = \frac{\text{Volume of vapor in evaporator}}{\text{Volume of vapor in entire pipe}} = \frac{\sum_i A\Delta s_{e,i} f_{v,i}}{\sum_i A\Delta s_i f_{v,i}} = \frac{\sum_i \Delta s_{e,i} f_{v,i}}{\sum_i \Delta s_i f_{v,i}} \tag{4.35}$$

$$R_{l,et} = \frac{\text{Volume of liquid in evaporator}}{\text{Volume of liquid in entire pipe}} = \frac{\sum_i A\Delta s_{e,i} f_{l,i}}{\sum_i A\Delta s_i f_{l,i}} = \frac{\sum_i \Delta s_{e,i} f_{l,i}}{\sum_i \Delta s_i f_{l,i}} \tag{4.36}$$

$$R_{v,ct} = \frac{\text{Volume of vapor in condenser}}{\text{Volume of vapor in entire pipe}} = \frac{\sum_i A\Delta s_{c,i} f_{v,i}}{\sum_i A\Delta s_i f_{v,i}} = \frac{\sum_i \Delta s_{c,i} f_{v,i}}{\sum_i \Delta s_i f_{v,i}} \tag{4.37}$$

$$R_{l,ct} = \frac{\text{Volume of liquid in condenser}}{\text{Volume of liquid in entire pipe}} = \frac{\sum_i A\Delta s_{c,i} f_{l,i}}{\sum_i A\Delta s_i f_{l,i}} = \frac{\sum_i \Delta s_{c,i} f_{l,i}}{\sum_i \Delta s_i f_{l,i}} \tag{4.38}$$

$$R_{v,at} = \frac{\text{Volume of vapor in adiabatic region}}{\text{Volume of vapor in entire pipe}} = \frac{\sum_i A\Delta s_{a,i} f_{v,i}}{\sum_i A\Delta s_i f_{v,i}} = \frac{\sum_i \Delta s_{a,i} f_{v,i}}{\sum_i \Delta s_i f_{v,i}} \tag{4.39}$$

$$R_{l,at} = \frac{\text{Volume of liquid in adiabatic region}}{\text{Volume of liquid in entire pipe}} = \frac{\sum_i A\Delta s_{a,i} f_{l,i}}{\sum_i A\Delta s_i f_{l,i}} = \frac{\sum_i \Delta s_{a,i} f_{l,i}}{\sum_i \Delta s_i f_{l,i}} \tag{4.40}$$

Chapter 5 Results

The results of volume fraction of vapor and liquid in the three regions, evaporator, condenser and adiabatic region, of the heat pipe for the water-OHP after analysis are shown in Table 5.1. These numbers are the average of all frames in a test. The results of volume fraction of vapor and liquid in the three regions of the heat pipe for the acetone-OHP after analysis are shown in Table 5.2. The data in Table 5.1 and Table 5.2 are plotted in Figure 5.1 for vapor and Figure 5.2 for liquid. In these studies, all the heat inputs are steady-state if there is no specific notation.

Table 5.1. Volume fraction of vapor and liquid in the different regions of the heat pipe for the water-OHP.

Heat input (Watts)	0	26	50	99	149	200	300
Volume of vapor in evaporator to volume of evaporator	0.446	0.995	0.998	0.999	0.996	0.992	0.978
Volume of liquid in evaporator to volume of evaporator	0.554	0.005	0.002	0.001	0.004	0.008	0.022
Volume of vapor in condenser to volume of condenser	0.392	0.255	0.114	0.113	0.117	0.128	0.167
Volume of liquid in condenser to volume of condenser	0.609	0.745	0.886	0.887	0.883	0.872	0.833
Volume of vapor in adiabatic region to volume of adiabatic region	0.440	0.411	0.679	0.693	0.699	0.698	0.657
Volume of liquid in adiabatic region to volume of adiabatic region	0.561	0.589	0.321	0.307	0.301	0.302	0.343

Table 5.2. Volume fraction of vapor and liquid in the different regions of the heat pipe for the acetone-OHP.

Heat input (Watts)	0	24	51	73
Volume of vapor in evaporator to volume of evaporator	0.776	0.998	0.844	0.832
Volume of liquid in evaporator to volume of evaporator	0.224	0.003	0.156	0.168
Volume of vapor in condenser to volume of condenser	0.417	0.207	0.355	0.376
Volume of liquid in condenser to volume of condenser	0.583	0.793	0.645	0.624
Volume of vapor in adiabatic region to volume of adiabatic region	0.536	0.700	0.666	0.671
Volume of liquid in adiabatic region to volume of adiabatic region	0.465	0.301	0.334	0.329

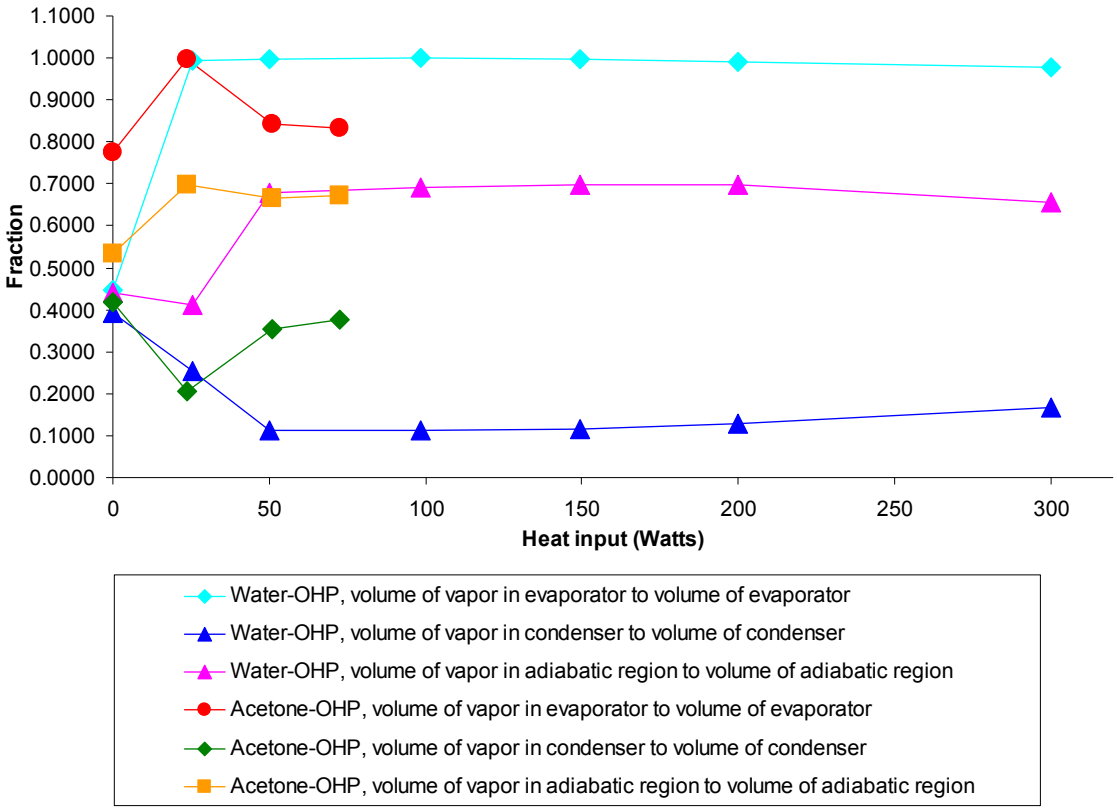

Figure 5.1. Plot of volume fraction of vapor in the different regions of the heat pipe for both the water-OHP and the acetone-OHP.

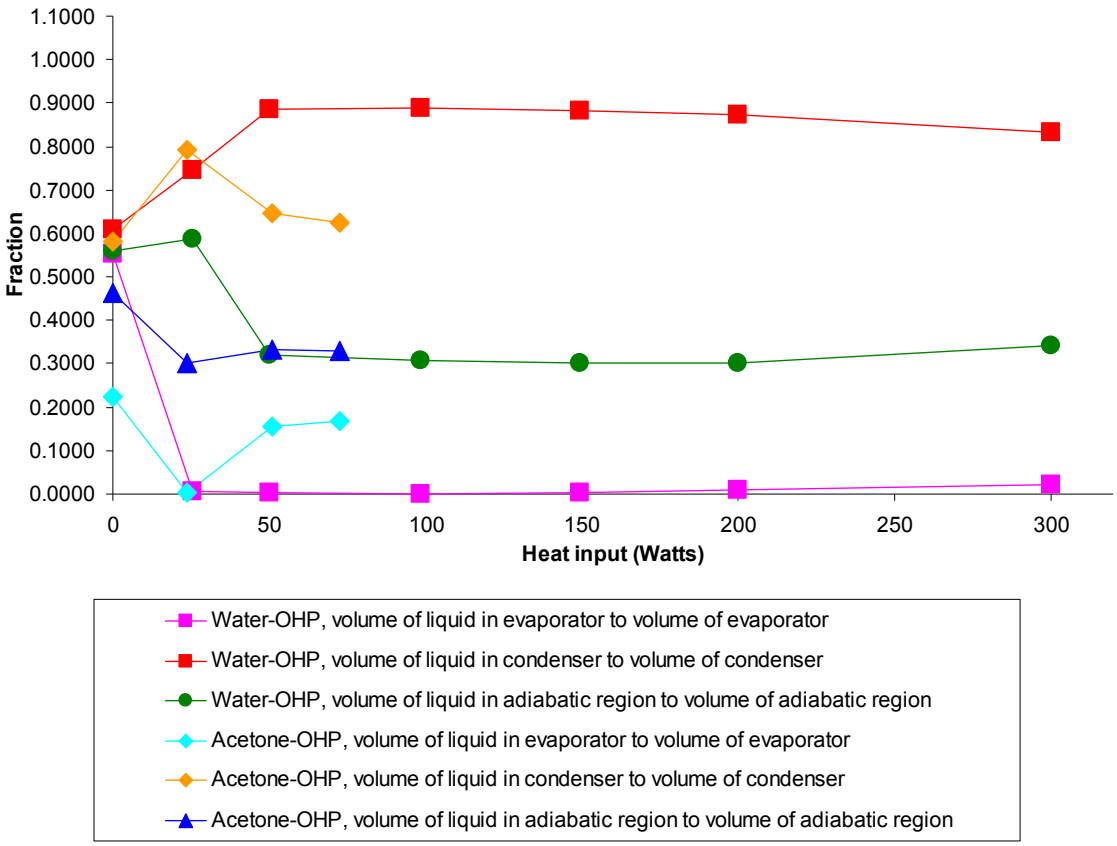

Figure 5.2. Plot of volume fraction of liquid in the different regions of the heat pipe for both the water-OHP and the acetone-OHP.

The ratios of the vapor and liquid volumes in the different regions to the volume of the entire heat pipe for the water-OHP and the acetone-OHP are shown in Tables 5.3 and 5.4, respectively. The data from Tables 5.3 and 5.4 are plotted in Figure 5.3 for vapor and in Figure 5.4 for liquid. In this table, all the tests are the steady-state response.

Table 5.3. The ratios of the vapor and liquid volumes in different regions to the volume of the entire heat pipe for the water-OHP.

Heat input (Watts)	0	26	50	99	149	200	300
Volume of vapor in evaporator to volume of entire pipe	0.119	0.265	0.266	0.266	0.265	0.264	0.261
Volume of liquid in evaporator to volume of entire pipe	0.148	0.001	0.001	0.000	0.001	0.002	0.006
Volume of vapor in condenser to volume of entire pipe	0.179	0.116	0.052	0.052	0.053	0.059	0.076
Volume of liquid in condenser to volume of entire pipe	0.278	0.340	0.405	0.405	0.403	0.398	0.381
Volume of vapor in adiabatic region to volume of entire pipe	0.122	0.114	0.188	0.192	0.194	0.193	0.182
Volume of liquid in adiabatic region to volume of entire pipe	0.155	0.163	0.089	0.085	0.083	0.084	0.095

Table 5.4. The ratios of the vapor and liquid volumes in different regions to the volume of the entire heat pipe for the acetone-OHP.

Heat input (Watts)	0	24	51	73
Volume of vapor in evaporator to volume of entire pipe	0.210	0.271	0.229	0.226
Volume of liquid in evaporator to volume of entire pipe	0.061	0.001	0.042	0.046
Volume of vapor in condenser to volume of entire pipe	0.191	0.095	0.163	0.172
Volume of liquid in condenser to volume of entire pipe	0.267	0.363	0.296	0.286
Volume of vapor in adiabatic region to volume of entire pipe	0.147	0.192	0.183	0.184
Volume of liquid in adiabatic region to volume of entire pipe	0.127	0.082	0.092	0.090

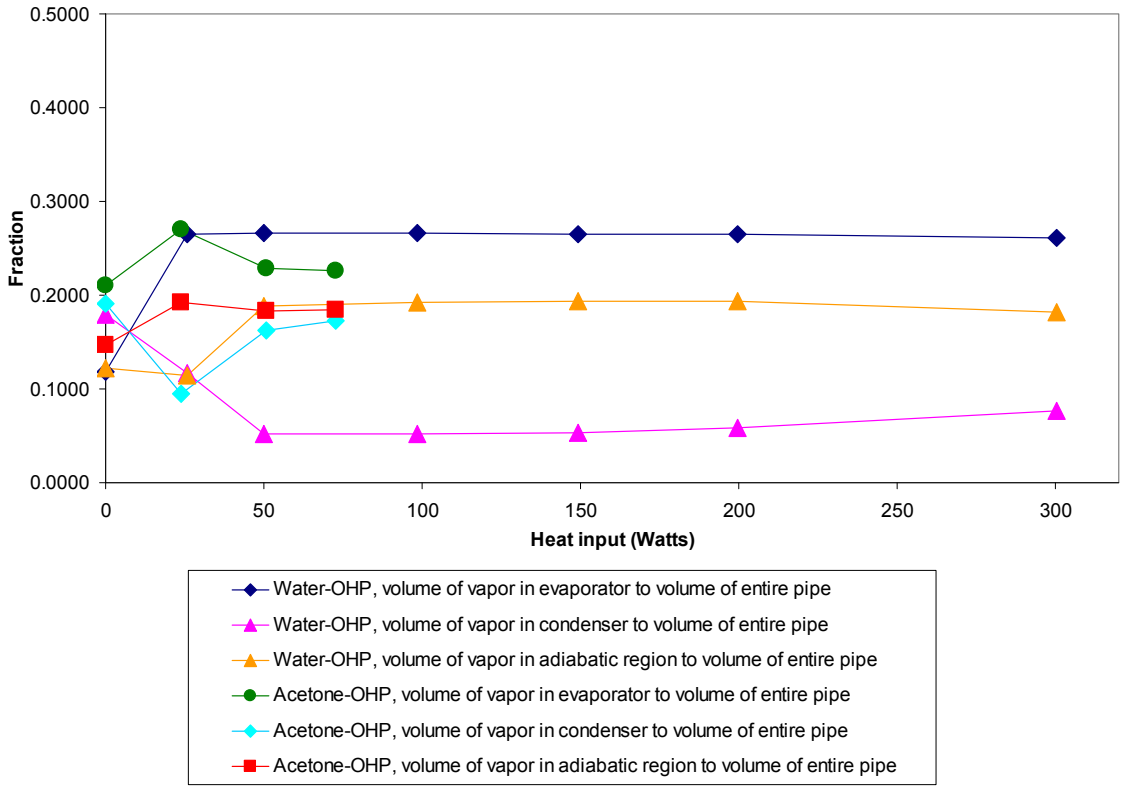

Figure 5.3. Plot of ratios of the vapor volume in the different regions to the volume of the entire heat pipe for both the water-OHP and the acetone-OHP.

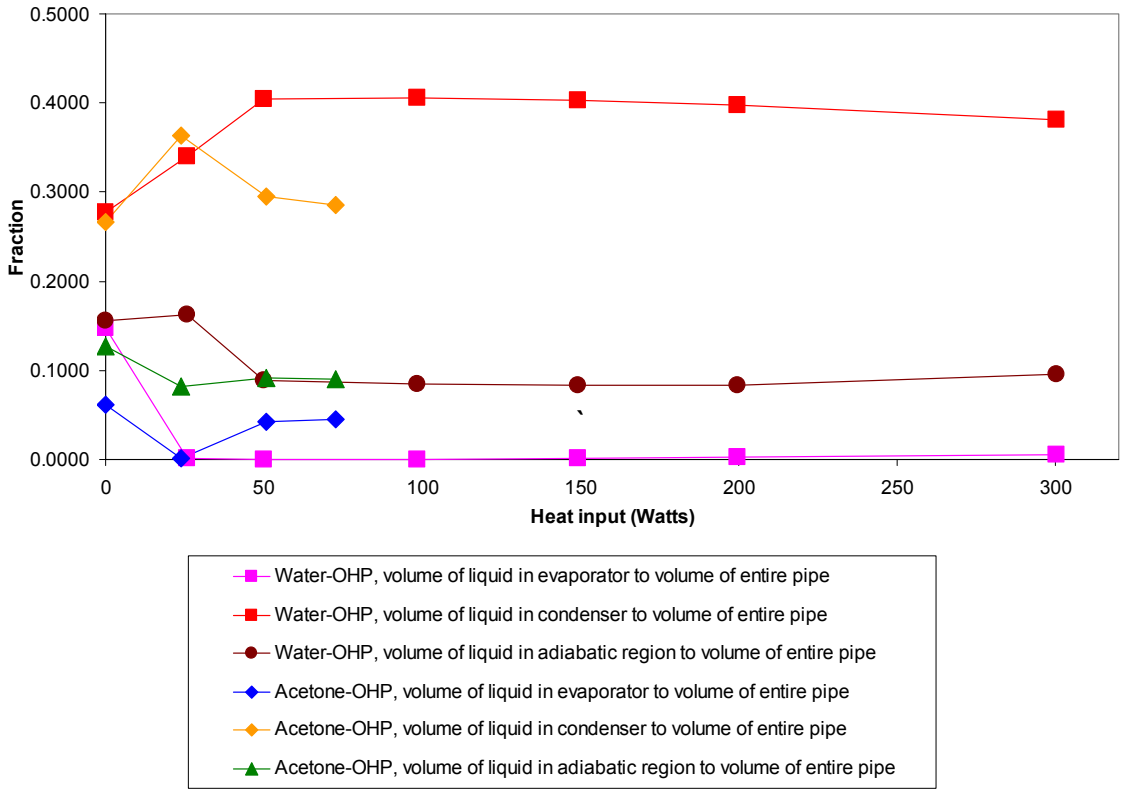

Figure 5.4. Plot of ratios of the liquid volume in the different regions to the volume of the entire heat pipe for both the water-OHP and the acetone-OHP

The ratios of the volume of vapor and liquid in the evaporator, condenser, and adiabatic regions to the volume of vapor and liquid in entire heat pipe for the water-OHP and the acetone-OHP are shown in Table 5.5 and Table 5.6, respectively. The plotted data from Table 5.5 and Table 5.6 are shown in Figure 5.5 for the vapor and Figure 5.6 for the liquid. In these tables all the tests are the steady-state response.

Table 5.5. The ratios of the volume of vapor and liquid in the evaporator, condenser, and adiabatic regions to the volume of vapor and liquid in the entire heat pipe for the water-OHP.

Heat input (Watts)	0	26	50	99	149	200	300
Volume of vapor in evaporator to volume of vapor in entire pipe	0.283	0.535	0.526	0.523	0.518	0.512	0.503
Volume of liquid in evaporator to volume of liquid in entire pipe	0.254	0.003	0.001	0.001	0.002	0.005	0.012
Volume of vapor in condenser to volume of vapor in entire pipe	0.426	0.235	0.103	0.101	0.104	0.113	0.147
Volume of liquid in condenser to volume of liquid in entire pipe	0.478	0.674	0.819	0.826	0.827	0.823	0.790
Volume of vapor in adiabatic region to volume of vapor in entire pipe	0.290	0.230	0.372	0.377	0.378	0.375	0.351
Volume of liquid in adiabatic region to volume of liquid in entire pipe	0.267	0.323	0.180	0.173	0.171	0.173	0.197

Table 5.6. The ratios of the volume of vapor and liquid in the evaporator, condenser, and adiabatic regions to the volume of vapor and liquid in the entire heat pipe for the acetone-OHP.

Heat input (Watts)	0	24	51	73
Volume of vapor in evaporator to volume of vapor in entire pipe	0.385	0.488	0.401	0.390
Volume of liquid in evaporator to volume of liquid in entire pipe	0.134	0.002	0.099	0.109
Volume of vapor in condenser to volume of vapor in entire pipe	0.350	0.171	0.284	0.297
Volume of liquid in condenser to volume of liquid in entire pipe	0.588	0.815	0.689	0.679
Volume of vapor in adiabatic region to volume of vapor in entire pipe	0.269	0.346	0.320	0.318
Volume of liquid in adiabatic region to volume of liquid in entire pipe	0.281	0.185	0.214	0.215

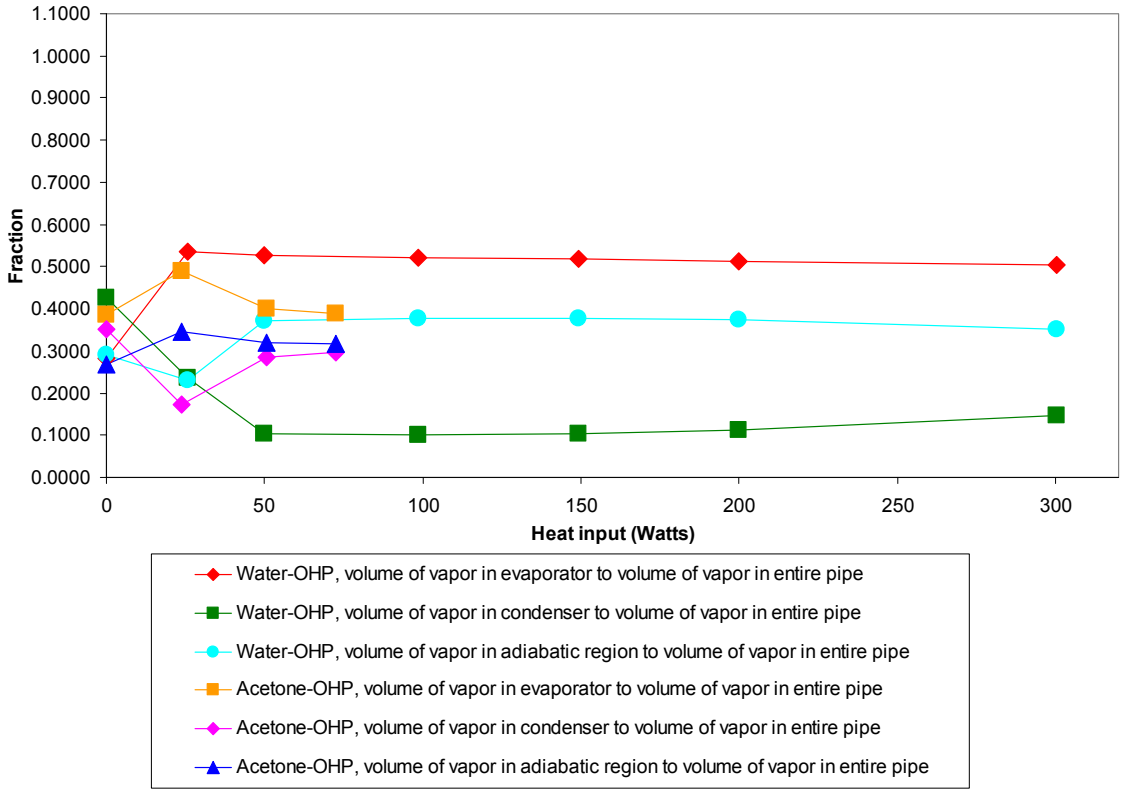

Figure 5.5. Plot of the ratios of the volume of vapor in the evaporator, condenser, and adiabatic regions to the volume of vapor in entire heat pipe for both the water-OHP and acetone-OHP.

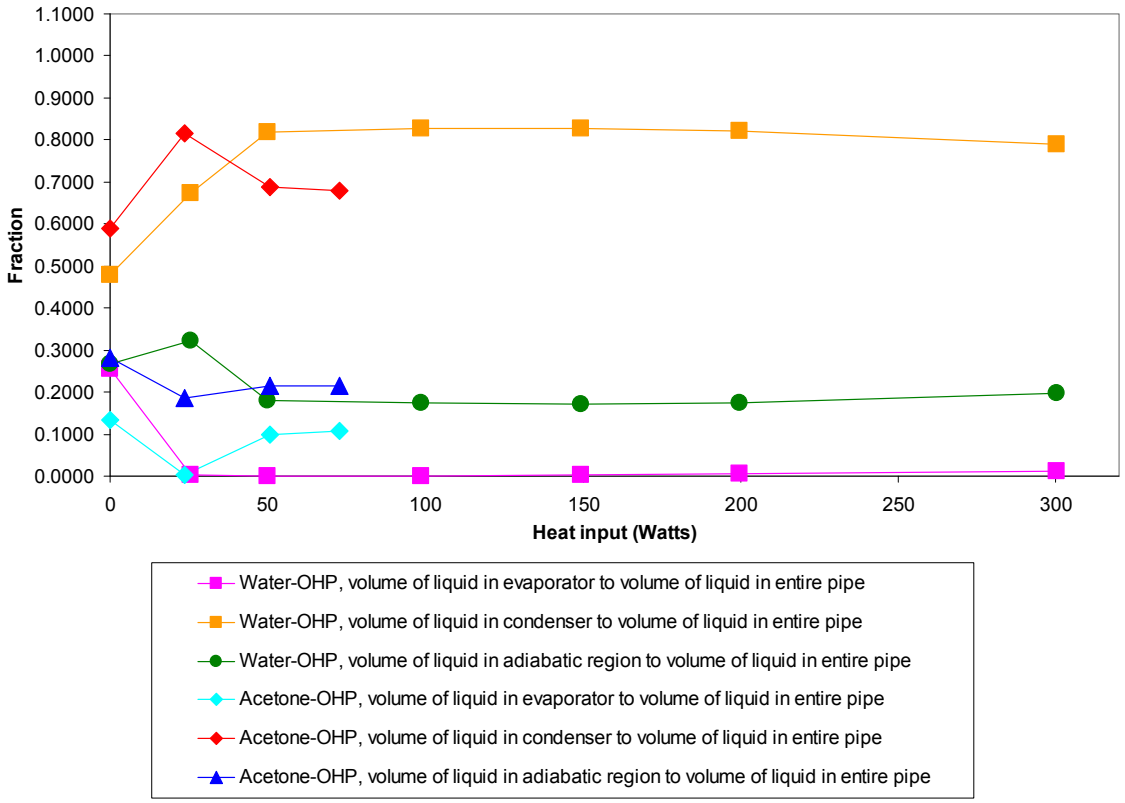

Figure 5.6. Plot of the ratios of the volume of liquid in the evaporator, condenser, and adiabatic regions to the volume of liquid in the entire heat pipe for both the water-OHP and acetone-OHP.

The thermal resistance, R, for an OHP is calculated with

$$R = \frac{\Delta T}{Q} \tag{5.1}$$

where ΔT is the temperature difference between the evaporator and the condenser and Q is the heat input. The temperature of the evaporator and condenser were determined by averaging the temperature readings of the eight thermocouples located in evaporator and condenser over the time of a steady state test. The thermal resistance for the water-OHP and the acetone-OHP are shown in Tables 5.7 and 5.8, respectively. Plotted data are shown with the data of liquid volume fraction in the evaporator in Figure 5.7. When

calculating results in these studies, temperature data from thermocouples 23 and 24 were excluded because they were not positioned on the cooling block area.

Table 5.7. The thermal resistance for the water-OHP.

Heat input (Watts)	Thermal resistance (°C/W)	Overall heat transfer coefficient (W/°C)
0	0.00	0.00
26	0.19	5.34
50	0.14	7.10
99	0.07	13.99
149	0.05	19.51
200	0.04	26.87
300	0.02	40.65

Table 5.8. The thermal resistance for the acetone-OHP.

Heat input (Watts)	Thermal resistance (°C/W)	Overall heat transfer coefficient (W/°C)
0	0.00	0.00
24	0.18	5.68
51	0.05	19.14
73	0.04	23.34

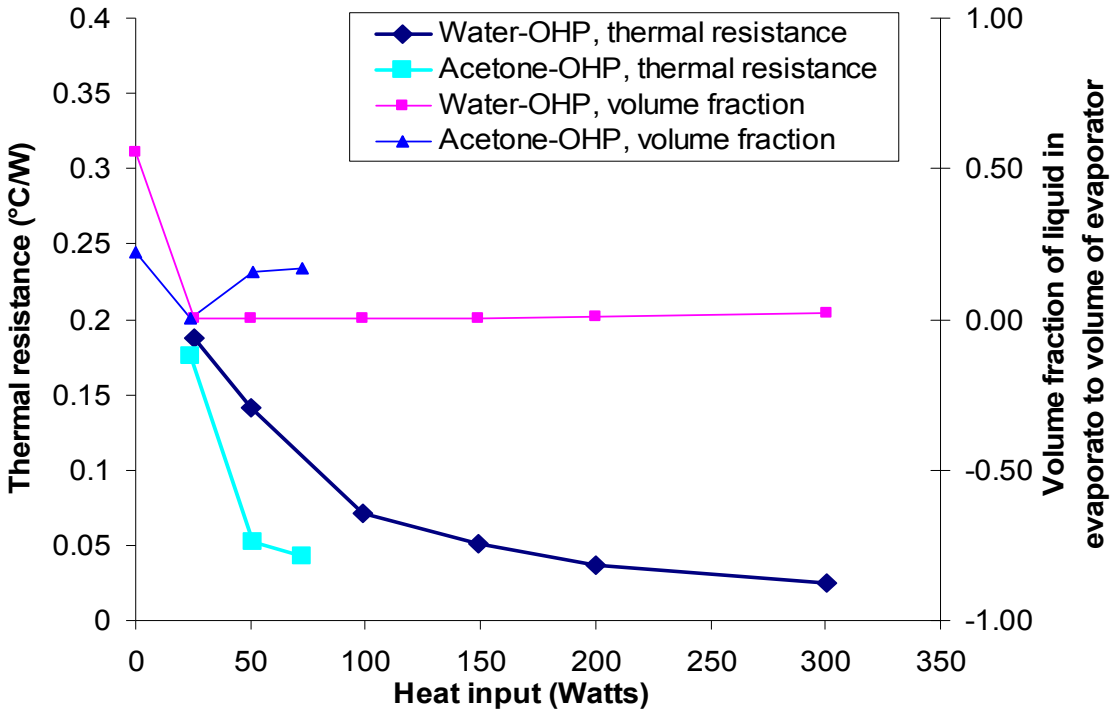

Figure 5.7. Plot of the thermal resistance for both the water-OHP and the acetone-OHP.

The overall heat transfer coefficient is calculated as the inverse of the thermal resistance. The overall heat transfer coefficient for the water-OHP and the acetone-OHP are shown in Tables 5.7 and Table 5.8, respectively. A plot of the data is shown along with the liquid volume fraction in the evaporator in Figure 5.8.

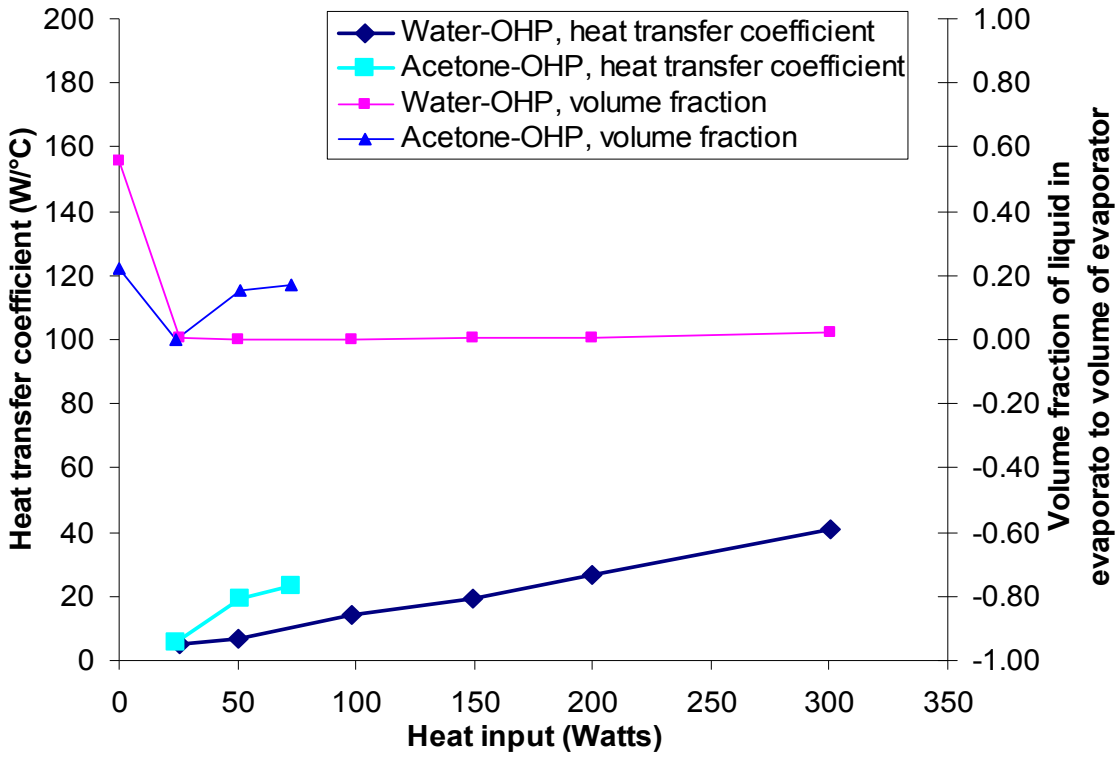

Figure 5.8. Plot of the overall heat transfer coefficient for both the water-OHP and the acetone-OHP.

The image data show that the startup time for the movement of liquid in the OHP is coincident with the startup time of the temperature fluctuations. That is, before liquid movement starts, the temperature rose slowly and stably as heat was input. When the liquid starts to move actively, the temperatures of the OHP begin to fluctuate.

At this point, some terms will be introduced for convenience. The period before the fluid movement startup is called the pre-startup period. When the liquid moves actively, it is called a macro-action period. Occasionally, after some amount of time, the liquid in the pipe stops moving or only moves a small amount. That is, in some areas in the tube, the liquid only moves slightly, but, usually does not move from the condenser to the evaporator or from the evaporator to the condenser. When the liquid does not move or moves little for more than 50 seconds after prior motion, it is called a macro-pause

period. It is ambiguous to define little movement of the liquid. Thus, if the volume fraction of liquid in the evaporator is less than 0.03 when liquid in the tubes moves, it is defined as little movement for these studies. Little movement is regarded as no movement although the liquid slugs move slightly. In Figure 5.9, an example of time series images with little movement of liquid are shown. The section shown in the images is the adiabatic region. As shown in Figure 5.9, it is hard to observe the movement of the liquid slugs although it is after the startup point. Actually, liquid slugs move but only very slightly. These three terms, pre-startup period, macro-action period, and macro-pause period are indicated in Figures 5.12, 5.13 and 5.14. It is observed that there are many small action periods and pause periods within a macro-action period. These are called micro-action periods and micro-pause periods. The liquid volume fraction in the evaporator versus the average temperatures of the evaporator, condenser and adiabatic regions for the water-OHP for all heat input tests are shown in Figures 5.10 to 5.21. The liquid volume fraction in the evaporator versus the average temperatures of the evaporator, condenser and adiabatic regions for the acetone-OHP for all heat input tests are shown in Figures 5.22 to 5.27. In Figure 5.28, the magnified macro-action period in Figure 5.12 is displayed. The horizontal line indicates where the volume fraction of liquid in the evaporator is 0.03. Liquid fraction data over this line were named micro-action periods and are indicated by arrows. The data under the line were named micro-pause periods.

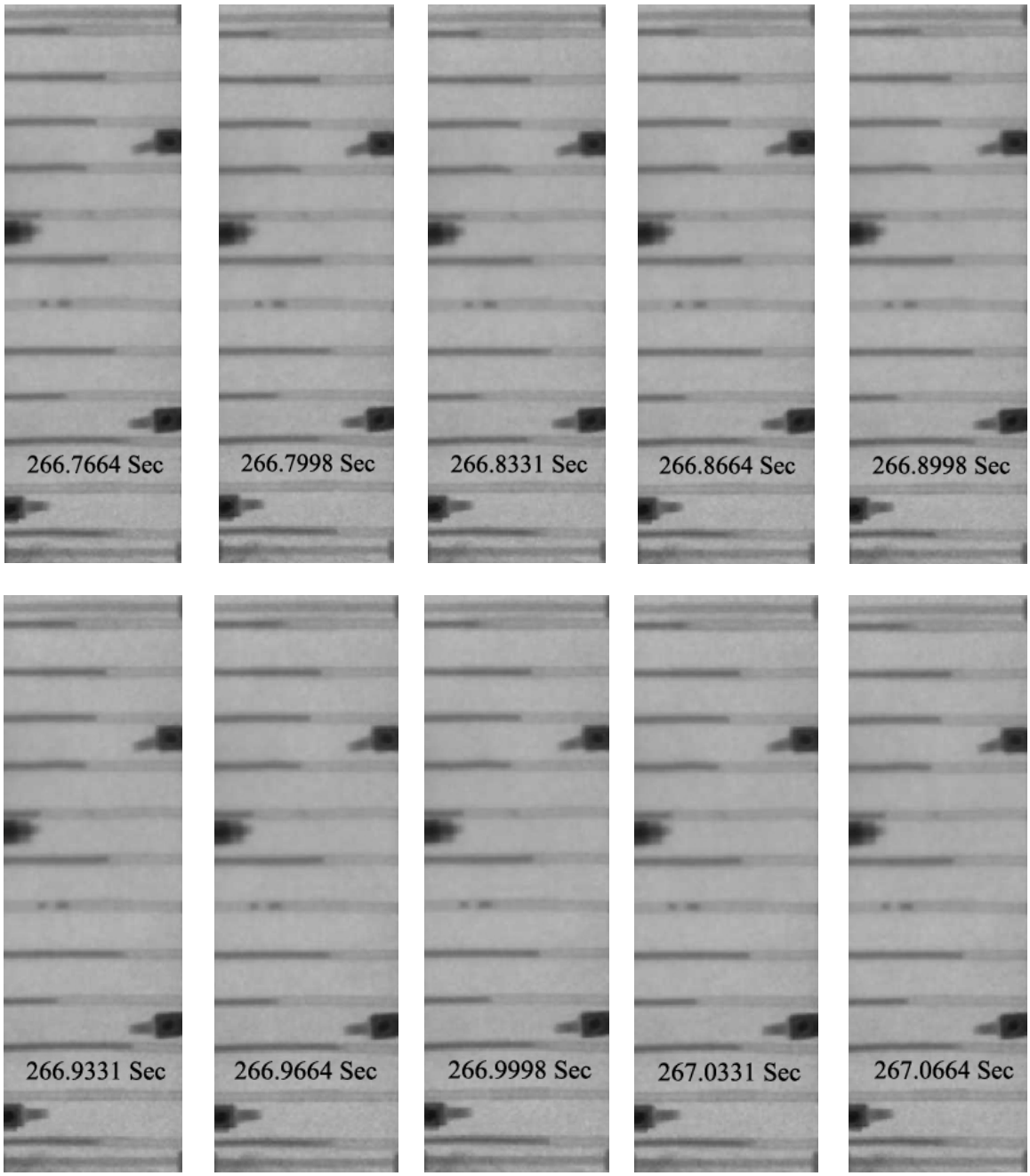

Figure 5.9. Sample time series images when liquid in the tubes only moves slightly.

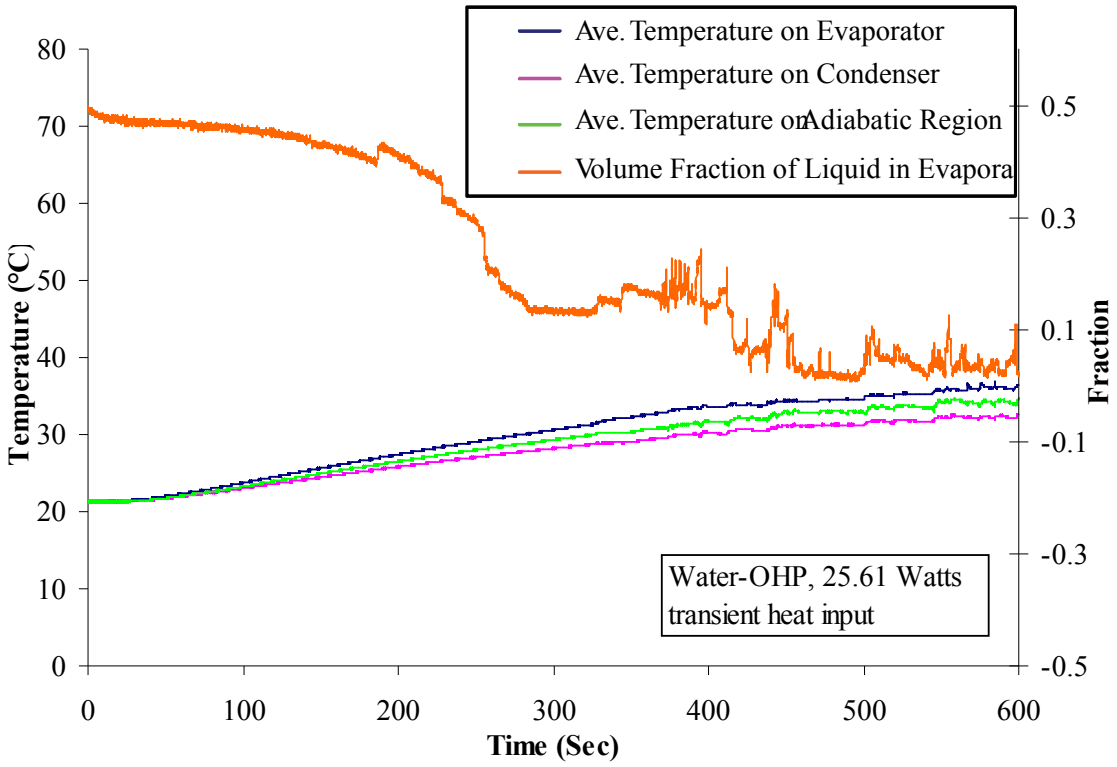

Figure 5.10. Transient response of the liquid volume fraction in the evaporator and the average temperature data for the evaporator, condenser and adiabatic region at 26 Watts heat input for the water-OHP.

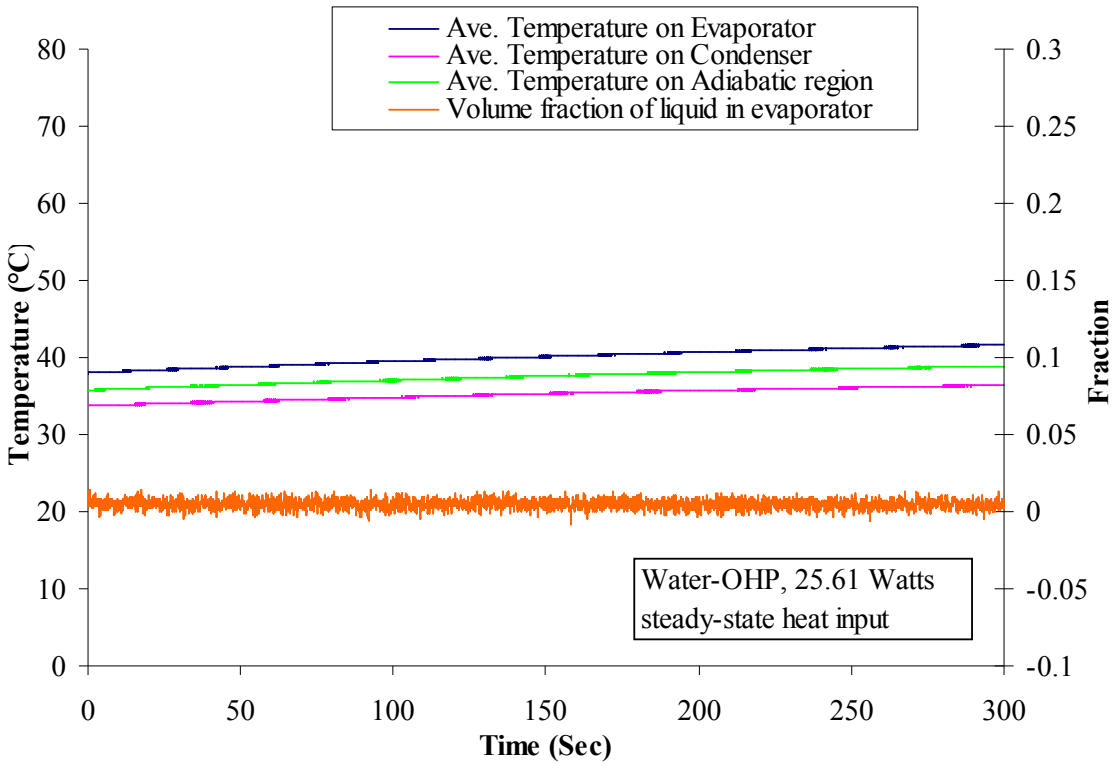

Figure 5.11. Steady-state response of the liquid volume fraction in the evaporator and the average temperature data for the evaporator, condenser and adiabatic region at 26 Watts heat input for the water-OHP.

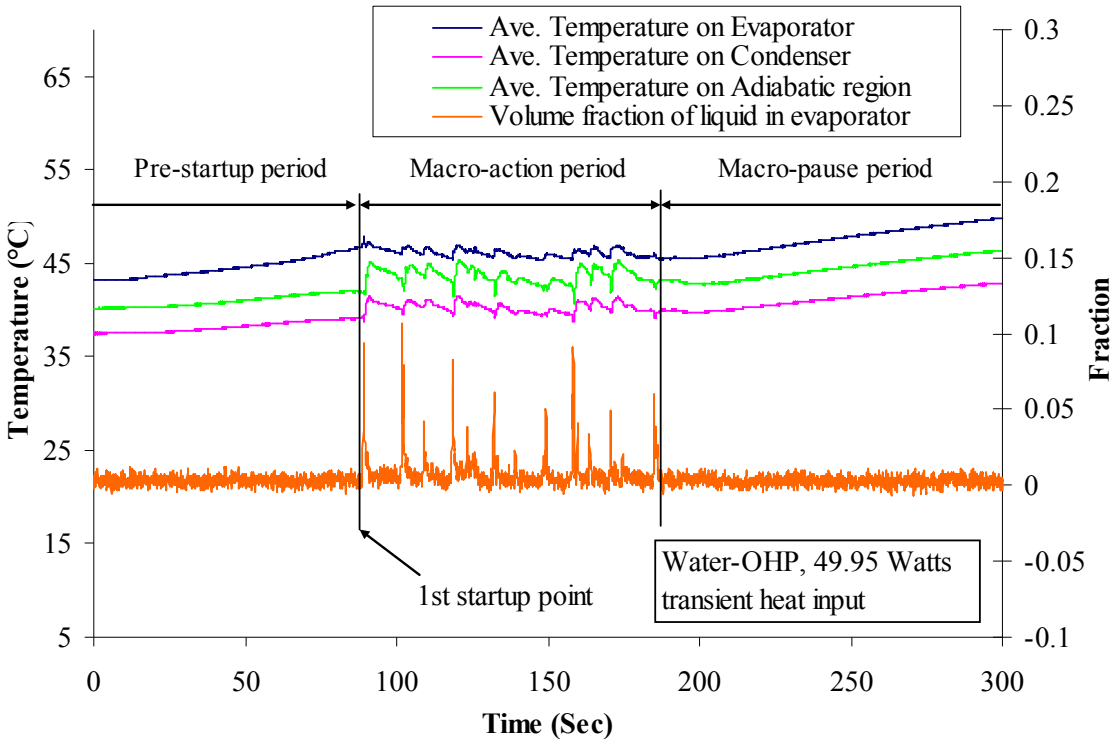

Figure 5.12. Transient response of the volume fraction of liquid in the evaporator and the average temperature data for the evaporator, condenser and adiabatic region at 50 Watts heat input for the water-OHP. The first startup point is indicated by an arrow. At this point, the liquid in the tube starts to move.

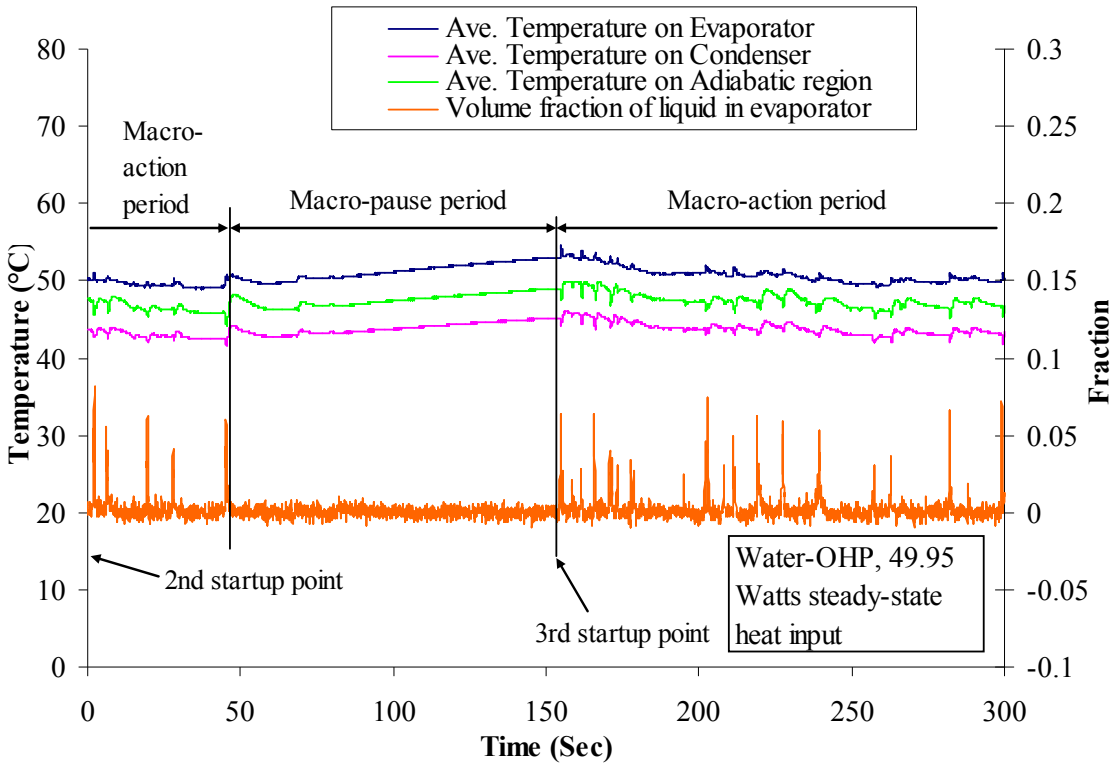

Figure 5.13. Steady-state response of the volume fraction of liquid in the evaporator and the average temperature data for the evaporator, condenser and adiabatic region at 50 Watts heat input for the water-OHP. The second and third startup points, indicated by arrows. Only the water movements in the macro-action periods are meaningful. In the macro-pause period, water in the tubes moves slightly, but is deemed negligible.

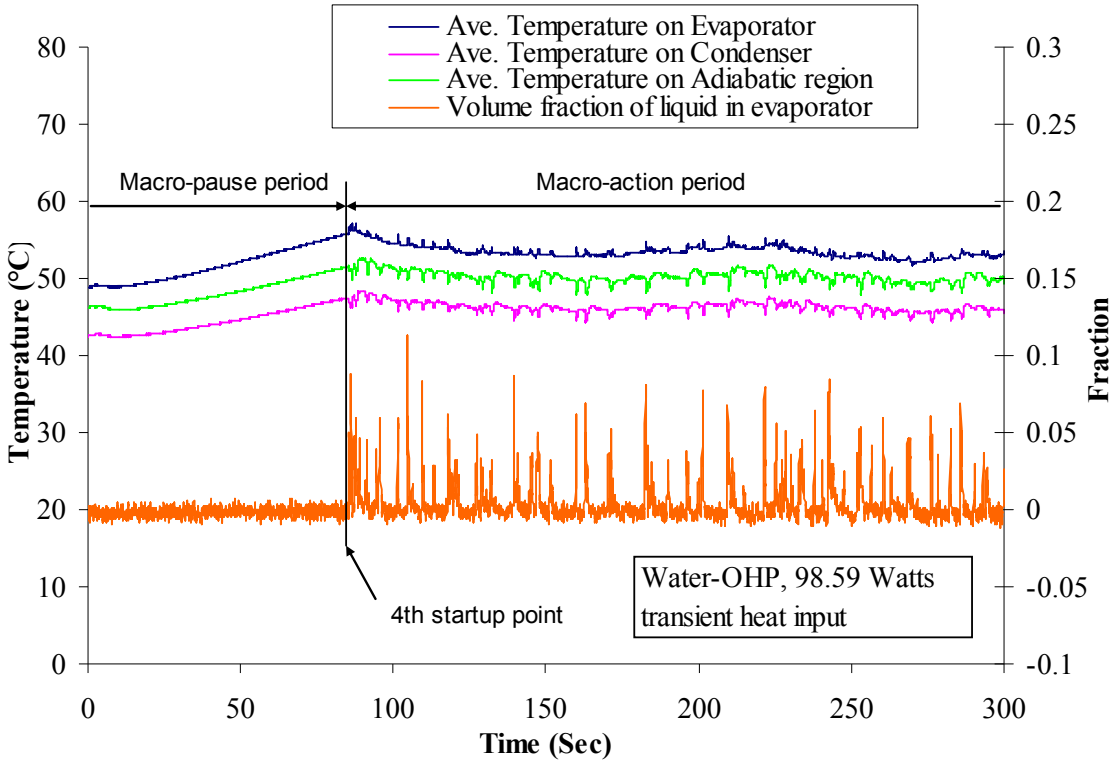

Figure 5.14. Transient response of the volume fraction of liquid in the evaporator and the average temperature data for the evaporator, condenser and adiabatic region at 99 Watts heat input for the water-OHP. The fourth startup point, indicated by an arrow.

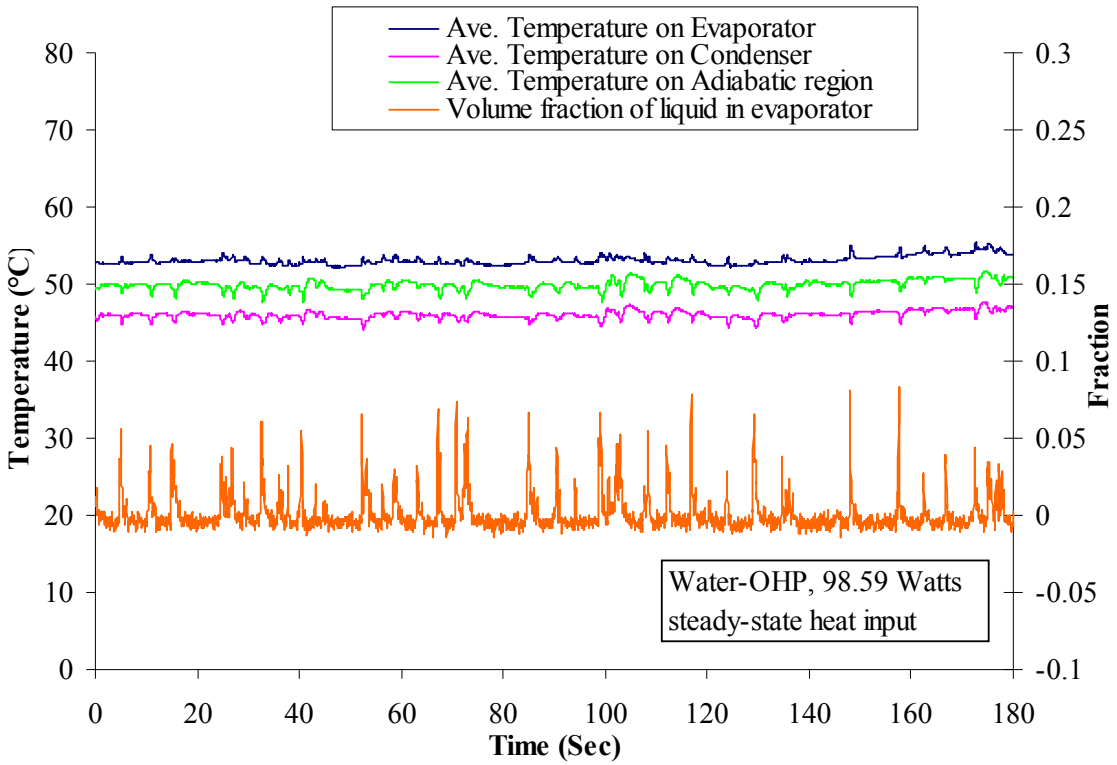

Figure 5.15. The steady-state response of the liquid volume fraction in the evaporator and average temperature data for the evaporator, condenser and adiabatic region at 99 Watts for the water-OHP.

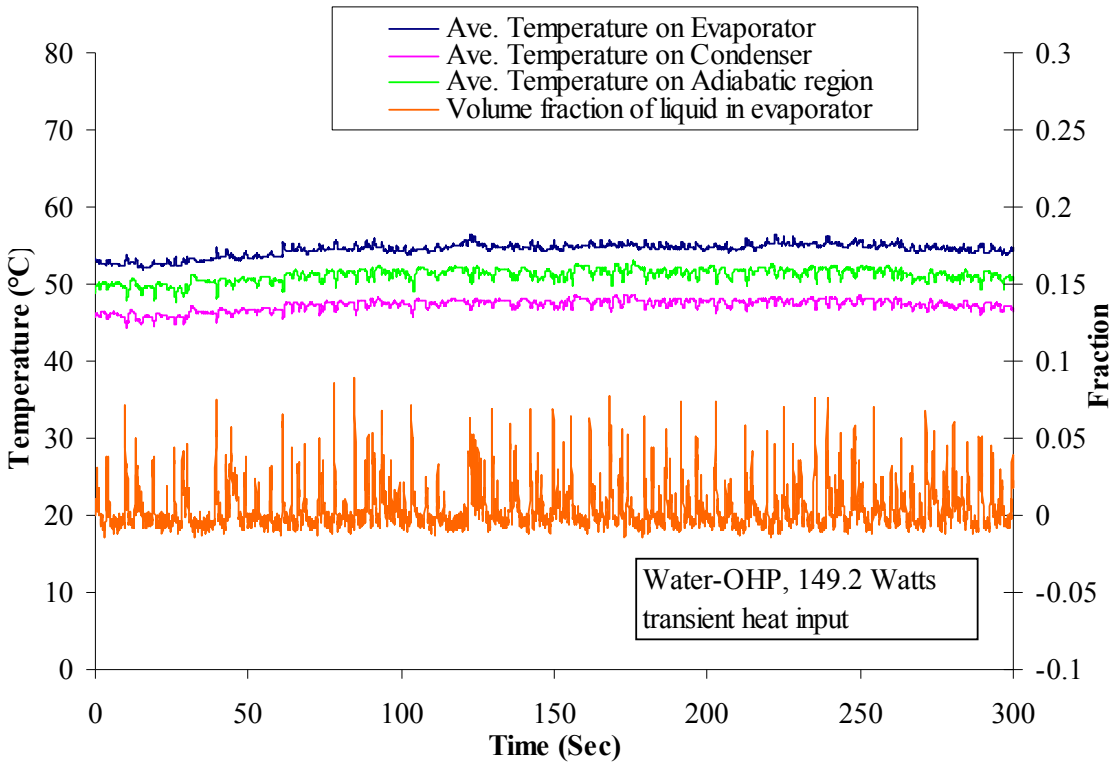

Figure 5.16. Transient response of the liquid volume fraction in the evaporator and the average temperature data for the evaporator, condenser and adiabatic region at 149 Watts heat input for the water-OHP.

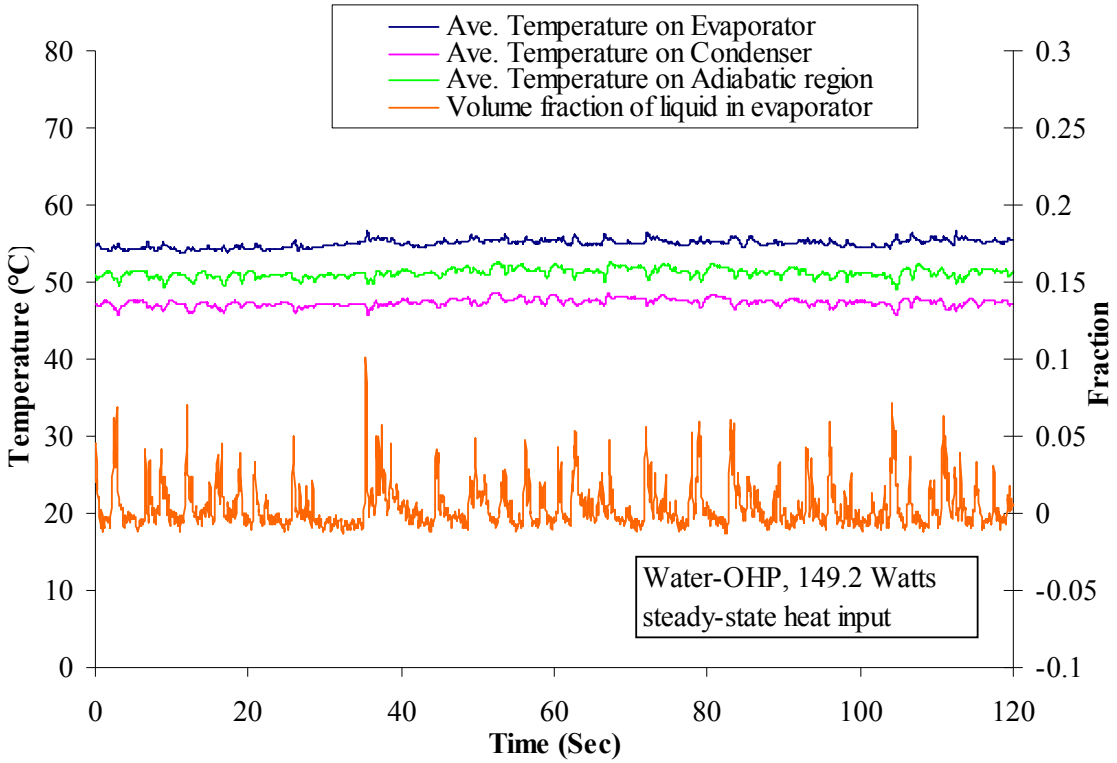

Figure 5.17. Steady-state response of the liquid volume fraction in the evaporator and the average temperature data for the evaporator, condenser and adiabatic region at 149 Watts heat input for the water-OHP.

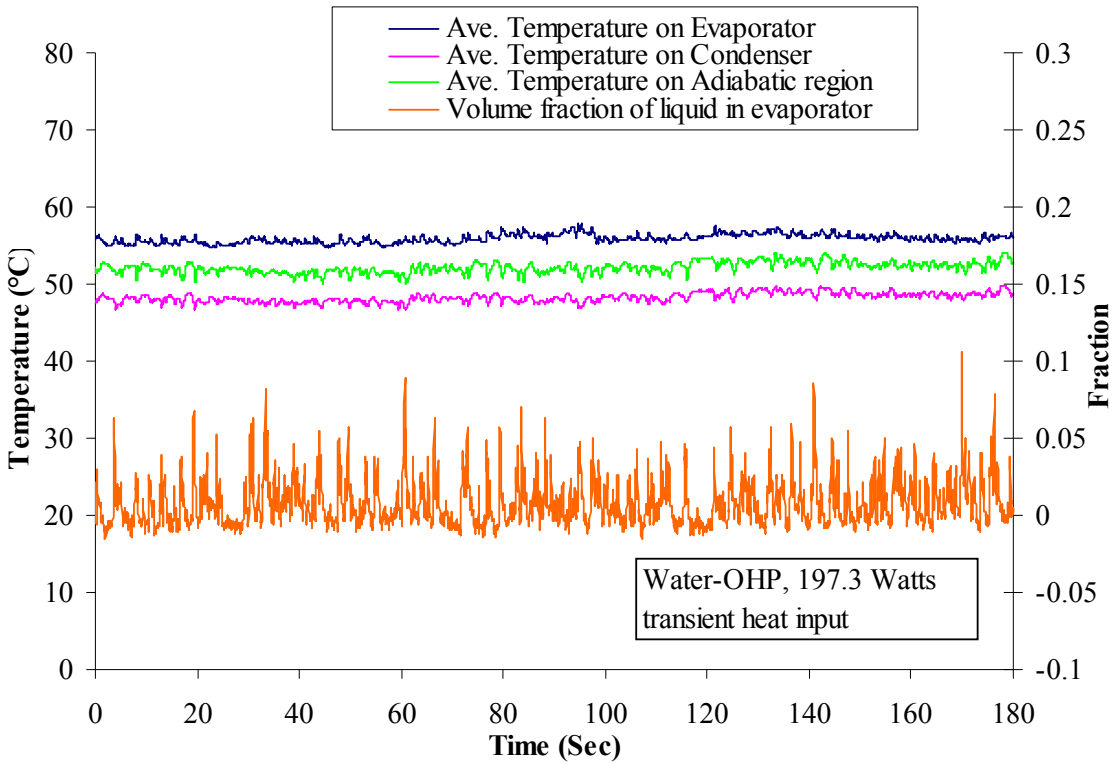

Figure 5.18. Transient response of the liquid volume fraction in the evaporator and the average temperature data for evaporator, condenser and adiabatic region at 197 Watts heat input for the water-OHP.

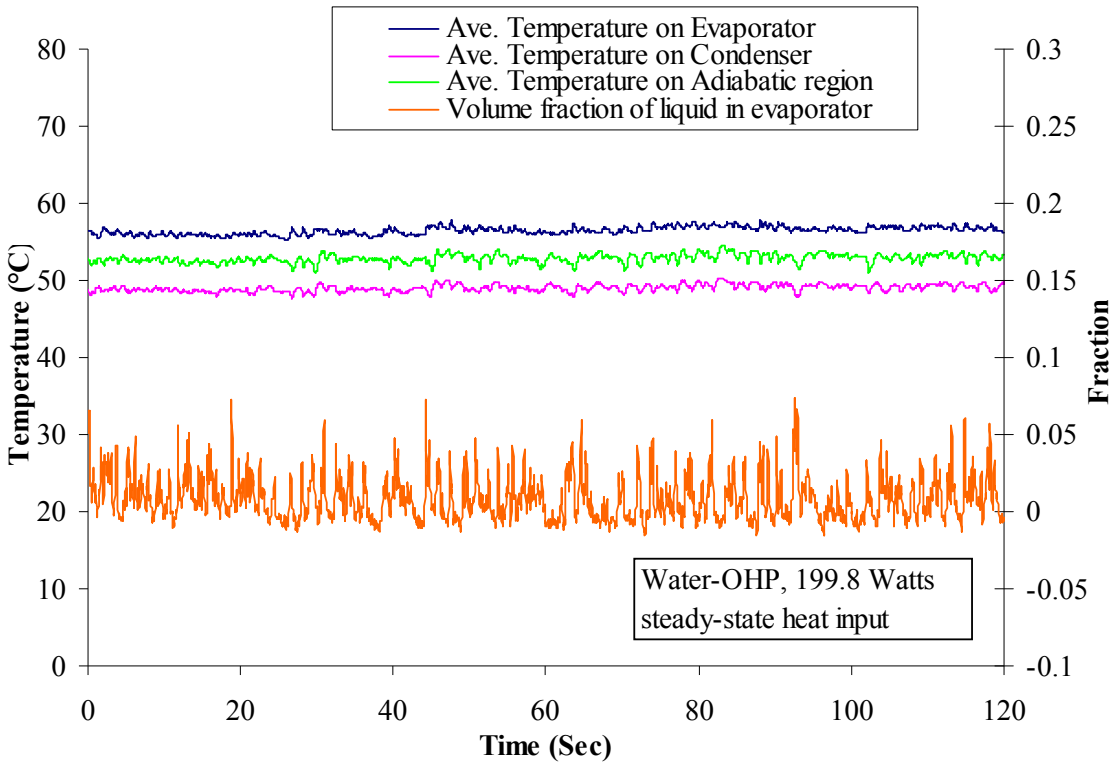

Figure 5.19. Steady-state response of the liquid volume fraction in the evaporator and the average temperature data for the evaporator, condenser and adiabatic region at 200 Watts heat input for the water-OHP.

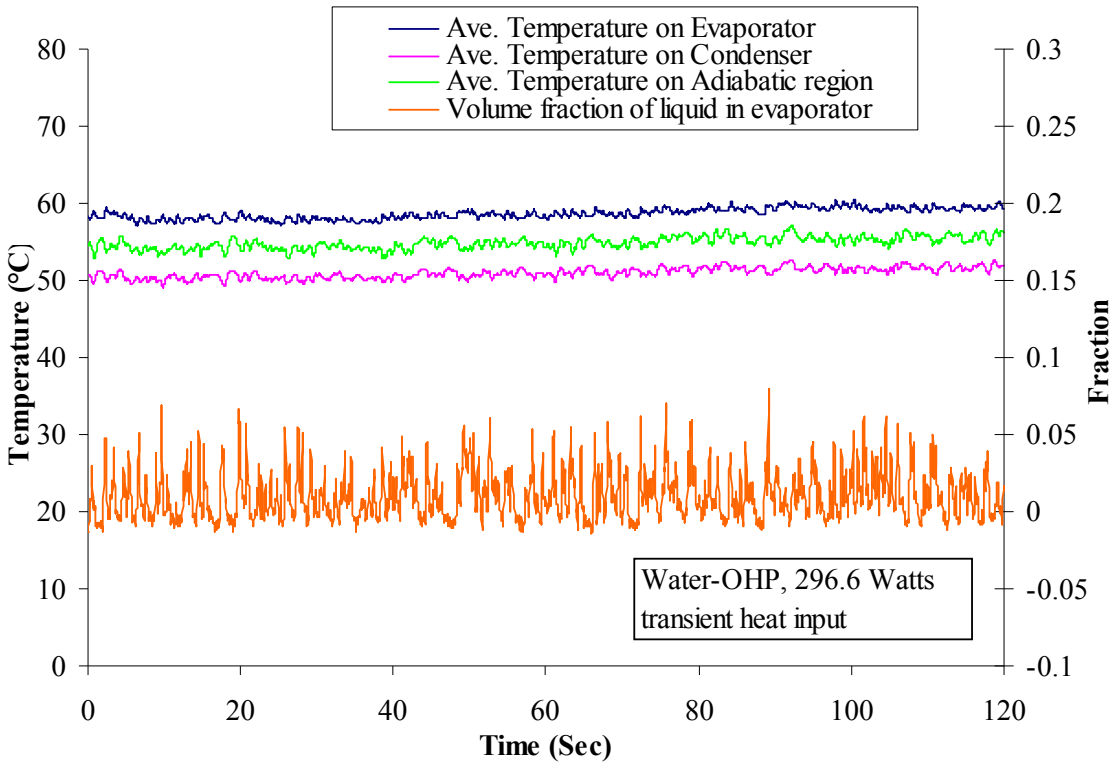

Figure 5.20. Transient response of the liquid volume fraction in the evaporator and the average temperature data for the evaporator, condenser and adiabatic region at 297 Watts heat input for the water-OHP.

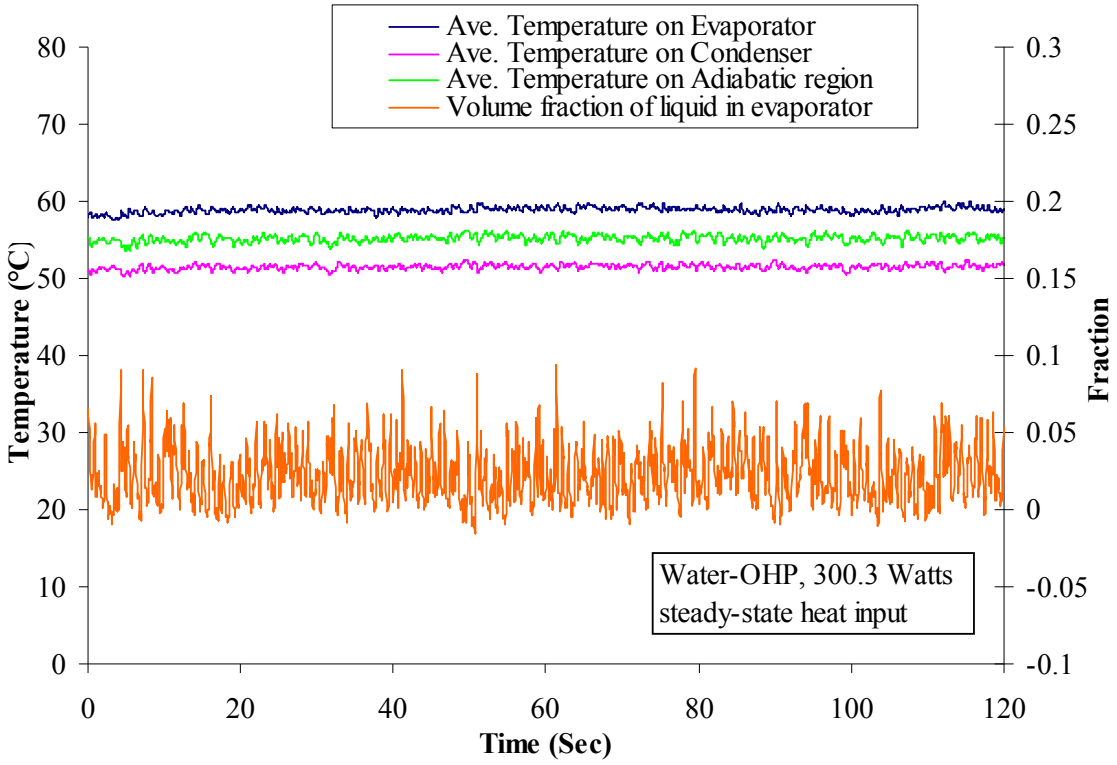

Figure 5.21. Steady-state response for the liquid volume fraction in the evaporator and the average temperature data for the evaporator, condenser and adiabatic region at 300 Watts heat input for the water-OHP.

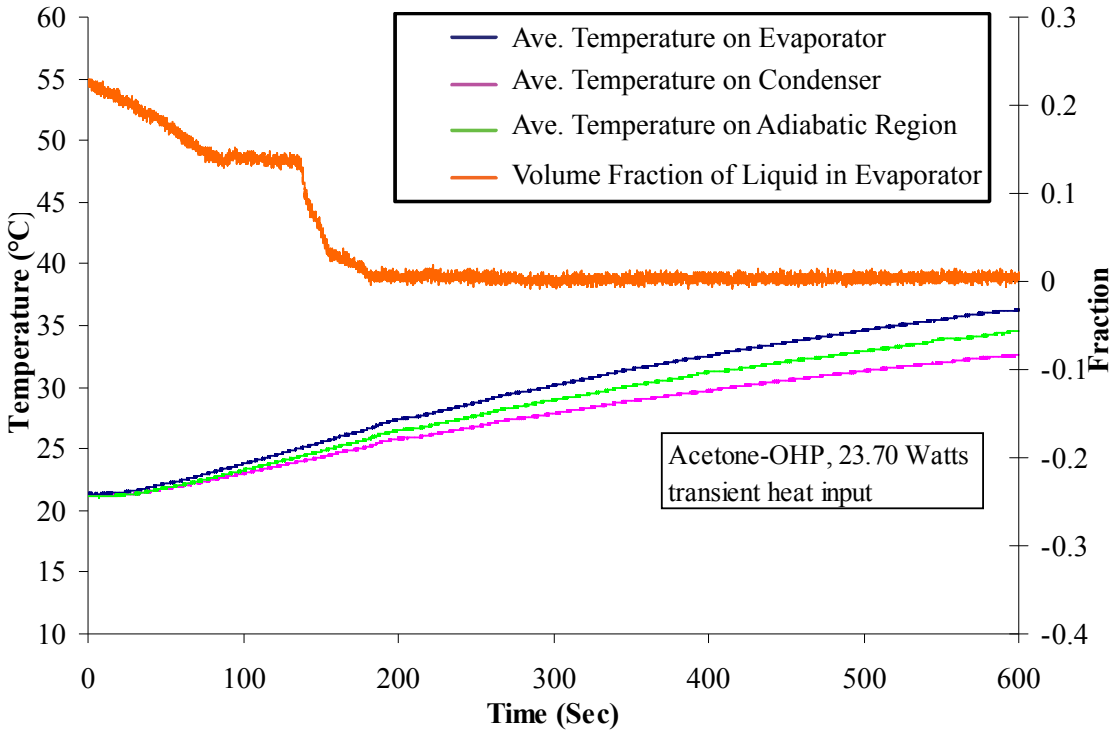

Figure 5.22. Transient response of the liquid volume fraction in the evaporator and the average temperature data for the evaporator, condenser and adiabatic region at 24 Watts heat input for the acetone-OHP.

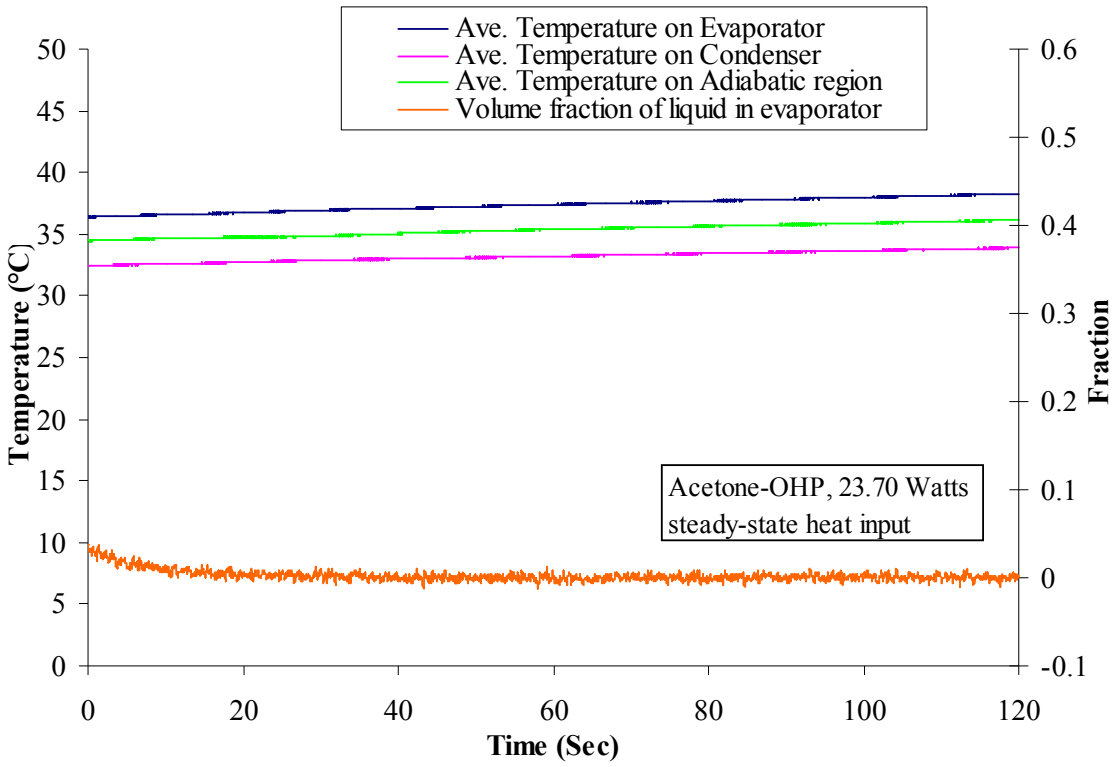

Figure 5.23. Steady-state response of the liquid volume fraction in the evaporator and the average temperature data for the evaporator, condenser and adiabatic region at 24 Watts heat input for the acetone-OHP.

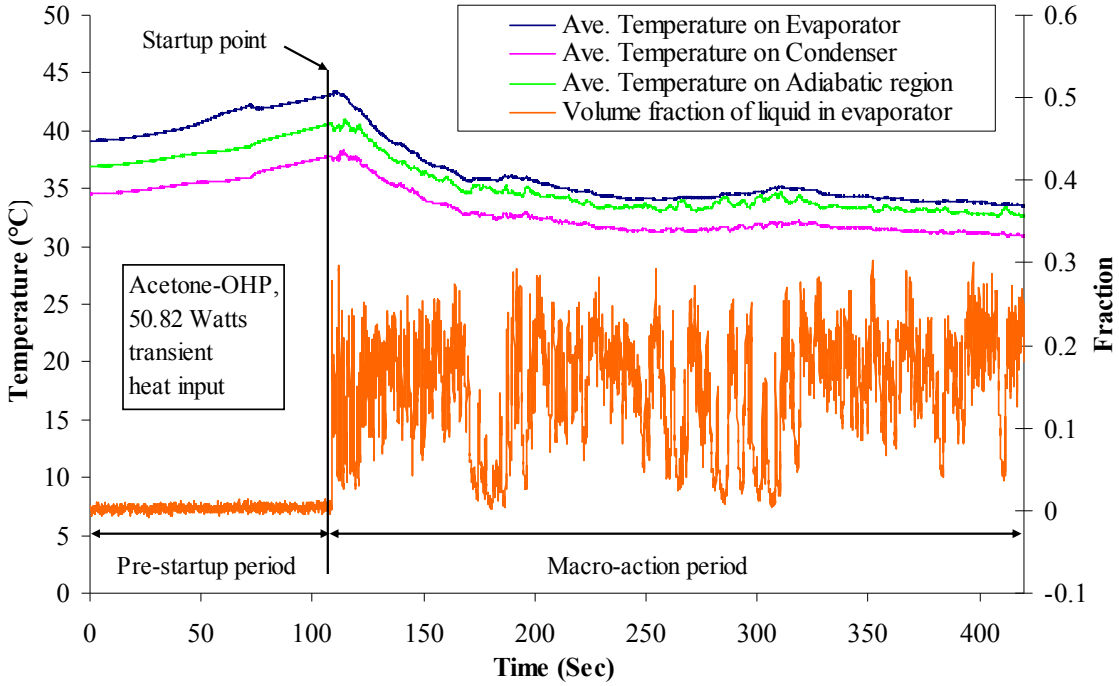

Figure 5.24. Transient response of the volume fraction of liquid in the evaporator and the average temperature data for the evaporator, condenser and adiabatic region at 51 Watts heat input for the acetone-OHP. The startup point, indicated by the arrow. At the startup point the liquid in the tube starts to move actively.

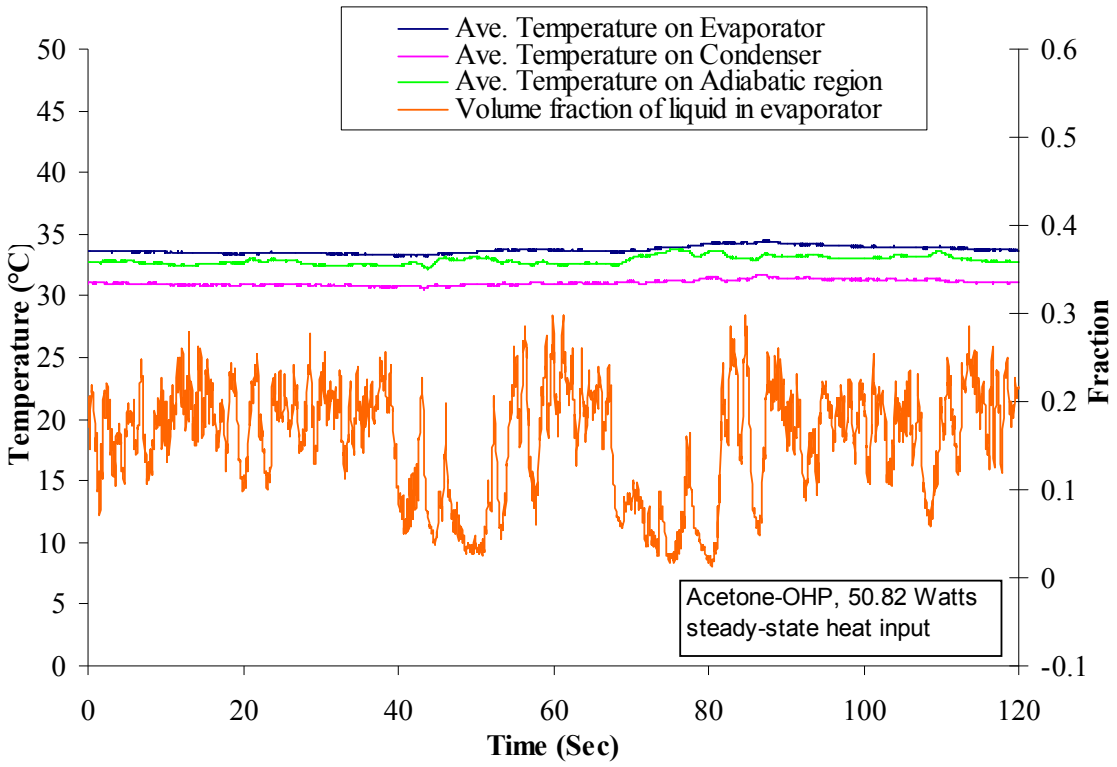

Figure 5.25. Steady-state response of the liquid volume fraction in the evaporator and the average temperature data for the evaporator, condenser and adiabatic region at 51 Watts heat input for the acetone-OHP.

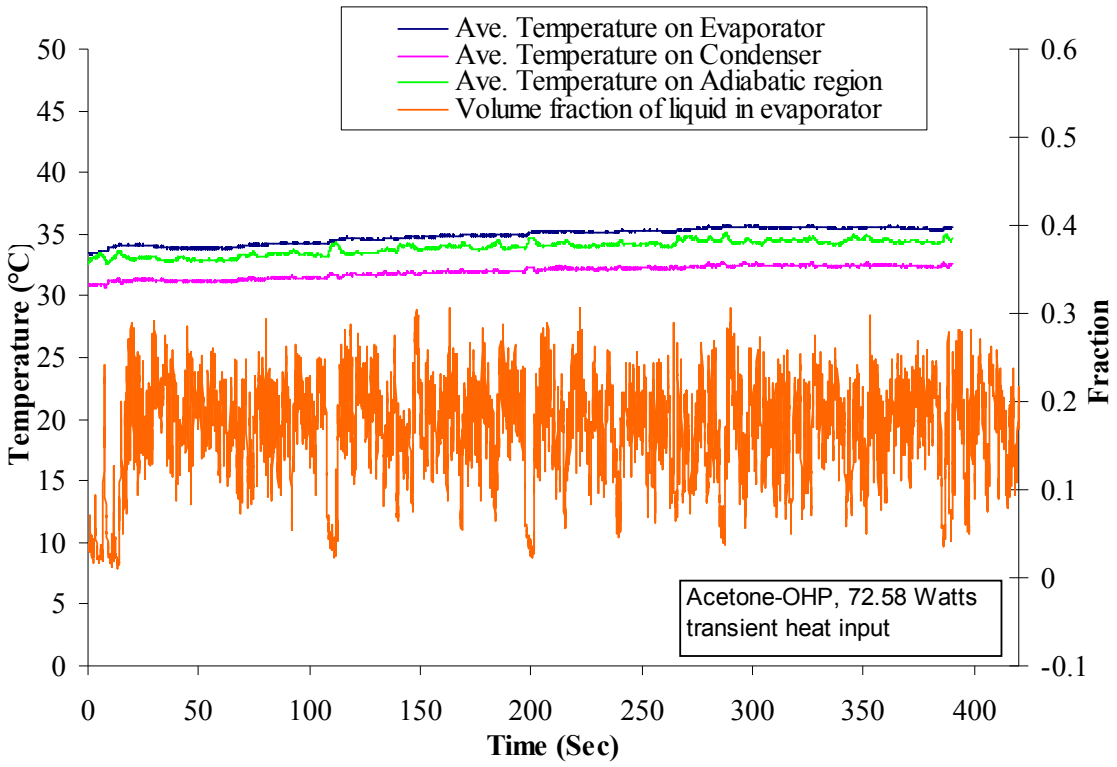

Figure 5.26. Transient response of the liquid volume fraction in the evaporator and the average temperature data for the evaporator, condenser and adiabatic region at 73 Watts heat input for the acetone-OHP.

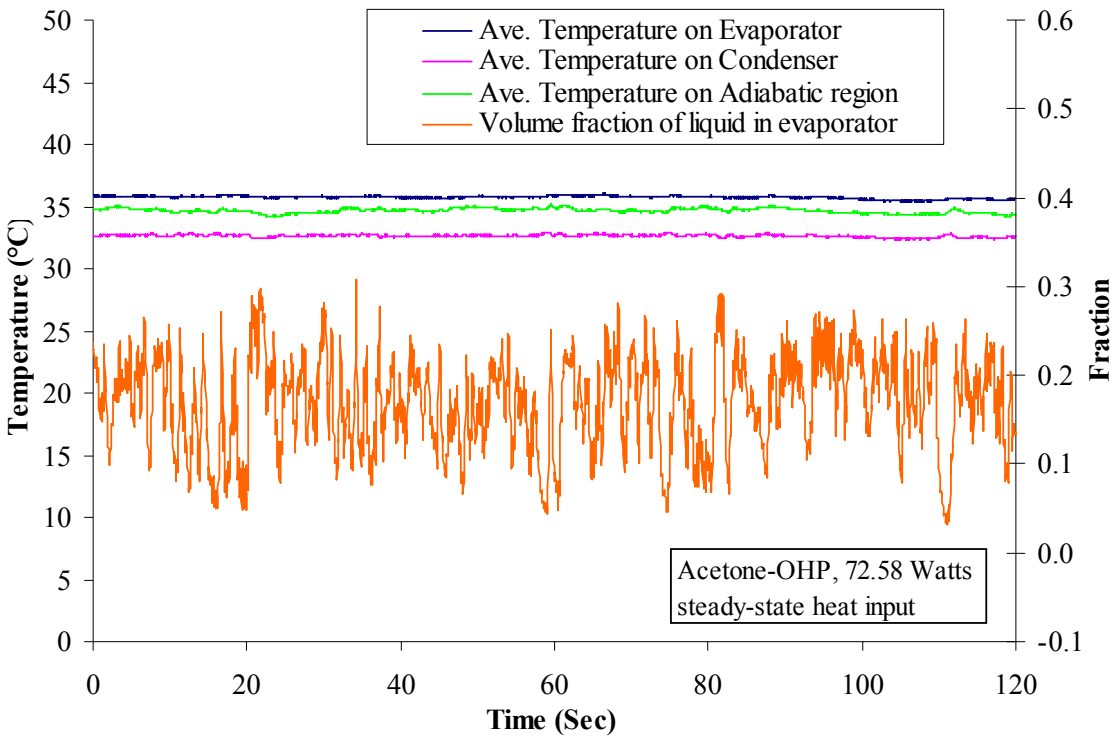

Figure 5.27. Steady-state response of the liquid volume fraction in the evaporator and the average temperature data for the evaporator, condenser and adiabatic region at 73 Watts heat input for the acetone-OHP.

For the water-OHP, there were four startup points observed in these studies. Actually, the second startup point is placed prior to the time range in Figure 5.13. The first startup point was observed during the transient after starting the 50 Watts heat input. Its movement lasted about 97 Sec. Following this, the liquid had almost no movement, i.e., it was in a macro-pause period. The second and the third startup points were observed during the 50 Watts heat input after it had reached steady-state conditions. The movements last more than 44 seconds for the second startup and more than 145 seconds for the third after their startup points. The second one is already moving when data for this test started recording. So, its starting time cannot be known exactly. The third and fourth ones last through the end of the measurement time, so their times cannot be known exactly. There is a short time gap between the end of the transient test and the beginning

of the steady-state test. It is assumed that the water-OHP continues with alternating macro-action and macro-pause periods.

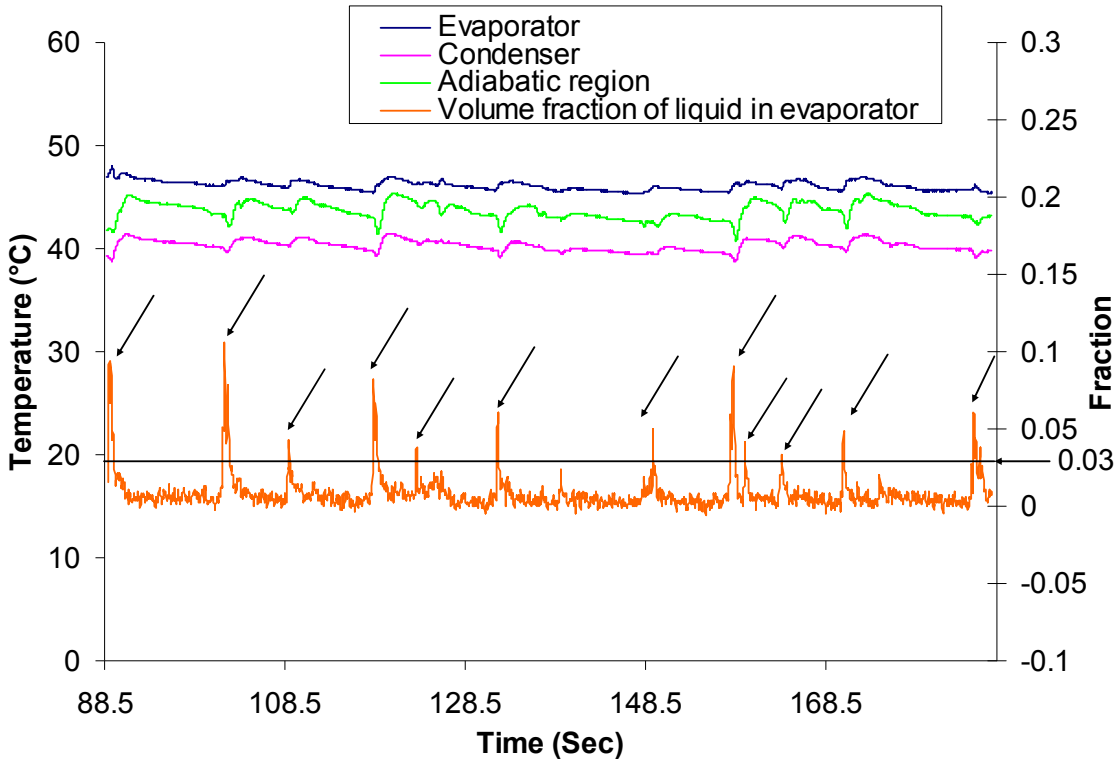

Figure 5.28. The micro-action periods and micro-pause periods in the water-OHP during transient test at 50 Watts heat input. The horizontal line indicates that the volume fraction of liquid in evaporator is 0.03. The data above this line, indicated by arrows, are micro-action periods and data below the line are micro-pause periods.

For the acetone-OHP, a startup point can be observed during the transient portion of the 51 Watts heat input test. Unlike the water-OHP, there is only one startup point for the acetone-OHP. That is, after the startup point, the liquid in the tubes moves constantly. The plotted average temperature data for the evaporator, condenser and adiabatic regions with time at this heat input and the volume fraction of liquid in the evaporator are shown in Figures 5.24 and 5.29 for the transient and steady-state tests, respectively. In Figure 5.30 there are sample images before and after the startup. Before the startup point, because of no or little movement of the acetone, the phase boundaries between the liquid

and the vapor are sharp in Figure 5.30(a). When the liquid starts to move actively, it moves fast and the boundaries are blurred. (Figure 5.30(b)) In Figure 5.29, it is shown that micro-pause periods are rare compared to the water-OHP at approximately same heat input because of the active acetone movement. From this and by the comparison of volume fraction of liquid in evaporator in Figures 5.12 and 5.24, it is inferred that the movement of liquid in the acetone-OHP is more active than in the water-OHP. This is also confirmed by observation of the videos of these tests.

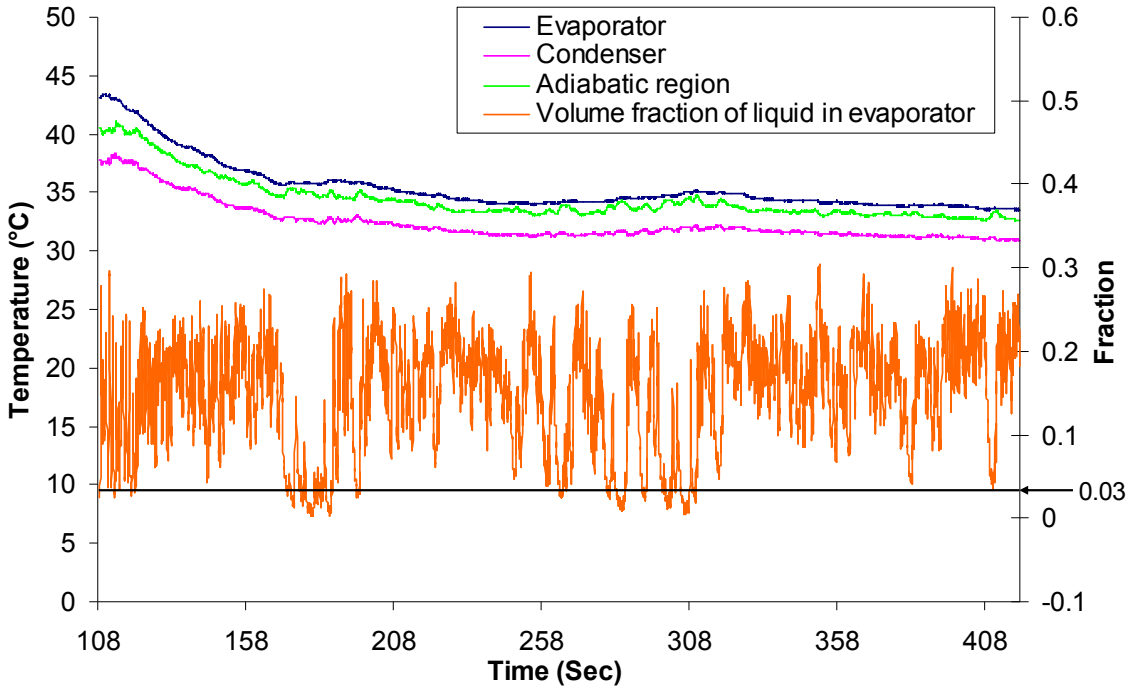

Figure 5.29. Volume fraction of liquid in the evaporator and the average temperature data for the evaporator, condenser and adiabatic region for the steady-state test at 51 Watts heat input for the acetone-OHP. The horizontal line indicates 0.03 of volume fraction of liquid in evaporator. The data under this horizontal line are the micro-pause periods.

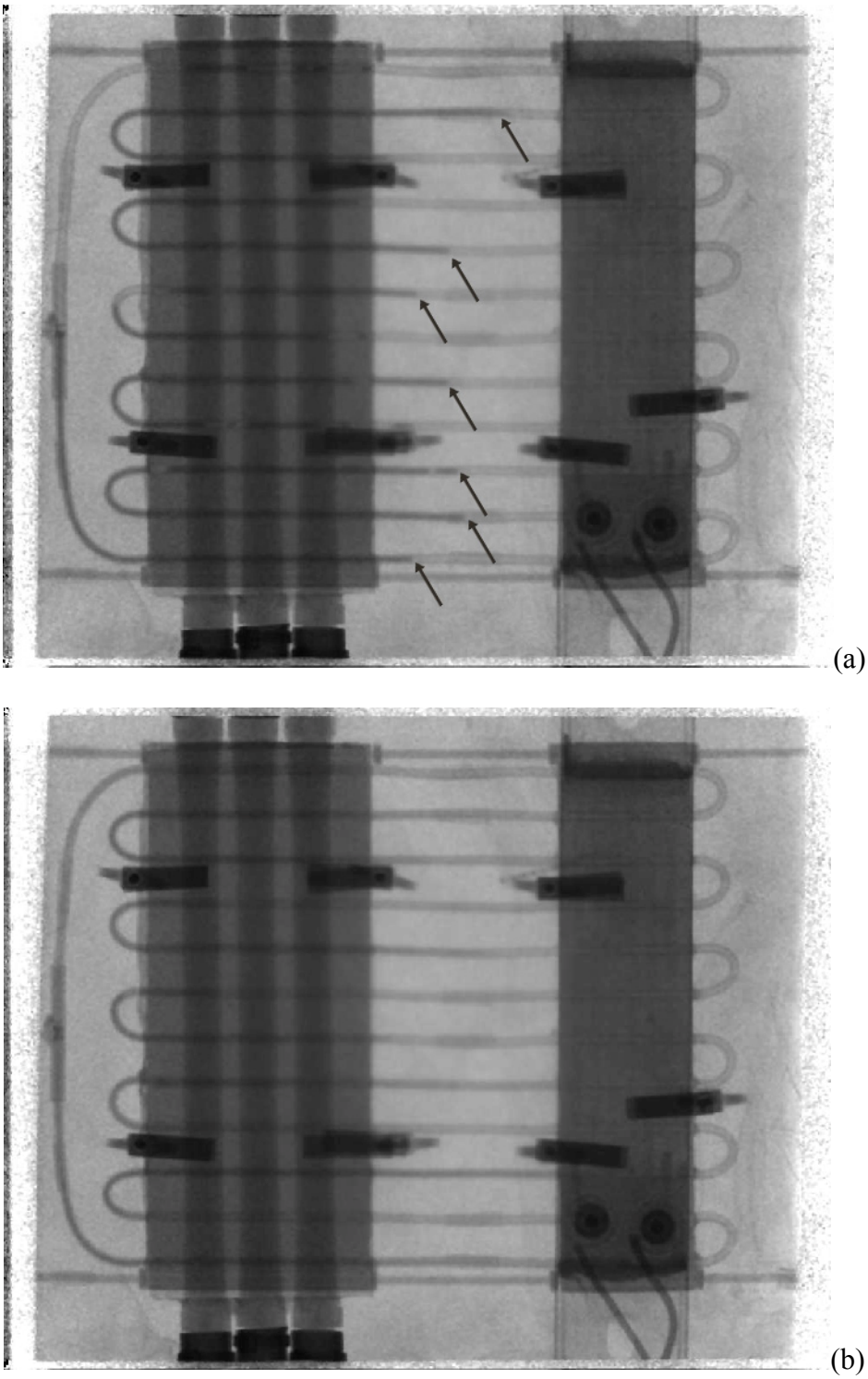

Figure 5.30. The images of acetone-OHP (a) before and (b) after the startup of liquid motion. In (a), at 108.27 s, the boundaries, indicated by arrows, between the vapor and liquid in the tubes are sharp meaning that the liquid in the tubes is not moving rapidly. In (b), at 110.13 s, the boundaries between the vapor and liquid in the tubes are not sharp because the liquid in the tubes is moving fast.

The liquid volume fraction on the positions where thermocouples were attached and the temperature data at the same positions were compared to see the temperature changes with the liquid movement. The data examined are from the transient and steady-state tests of the water-OHP at 50 Watts heat input and the acetone-OHP at 51 Watts heat input. Each OHP had 24 thermocouples. The data from thermocouples 23 and 24 were ignored because they were not positioned on the evaporator, condenser or adiabatic regions but on the long connecting loop (see Figure 3.12). Among the 22 thermocouples for each heat input, thermocouple number 19 from the evaporator, 5 from the condenser and 12 from the adiabatic region were analyzed. These thermocouples share a common leg on the OHPs.

In Figure 5.31, the liquid fraction and temperature data from the transient test of the water-OHP with 50 Watts heat input are displayed. The liquid fraction and temperature data from the steady-state test of the water-OHP with 50 Watts heat input are shown in Figure 5.32. The liquid fraction and temperature data from the transient and steady-state tests of the acetone-OHP with 51 Watts heat input are shown in Figures 5.33 and 5.34, respectively.

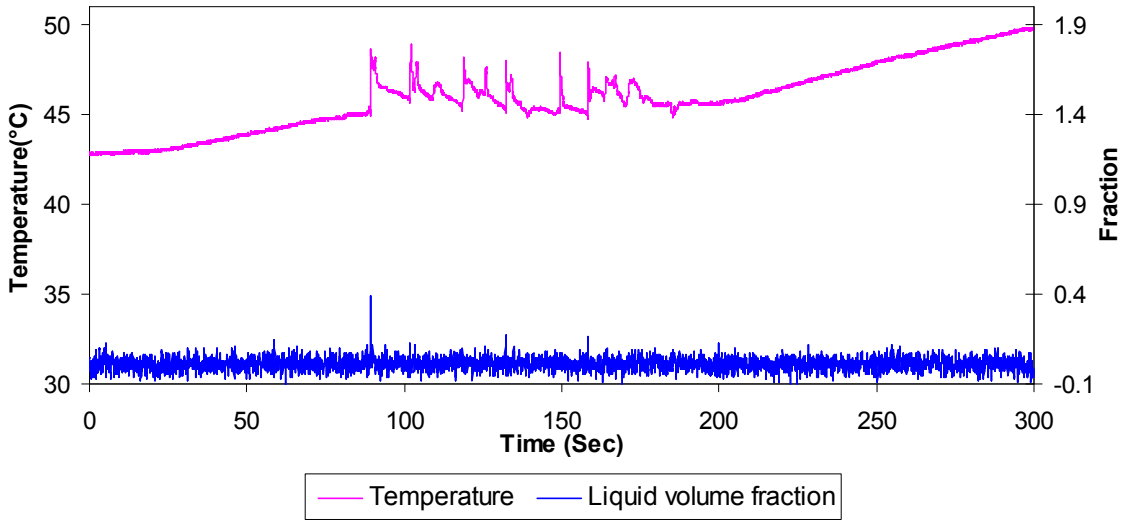

(a) Thermocouple number 16 in the evaporator

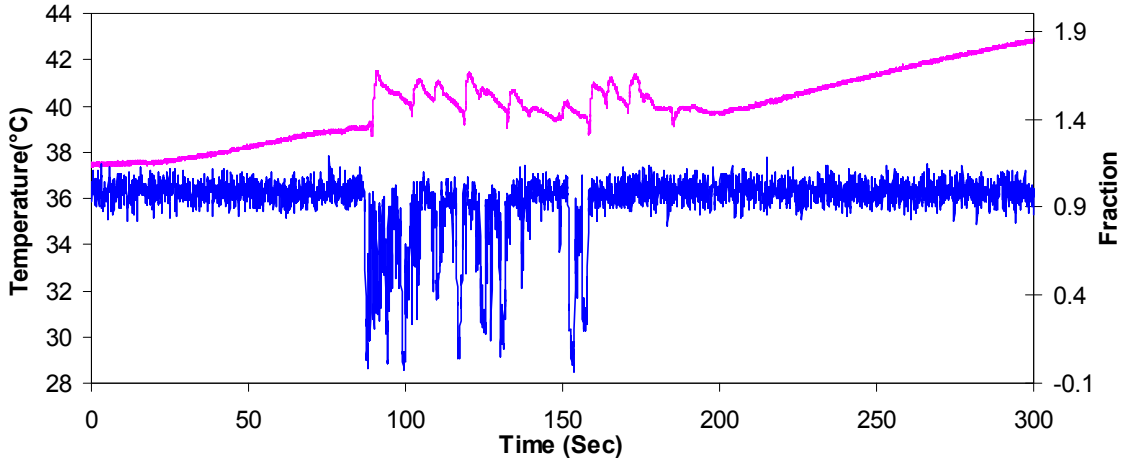

(b) Thermocouple number 2 in the condenser

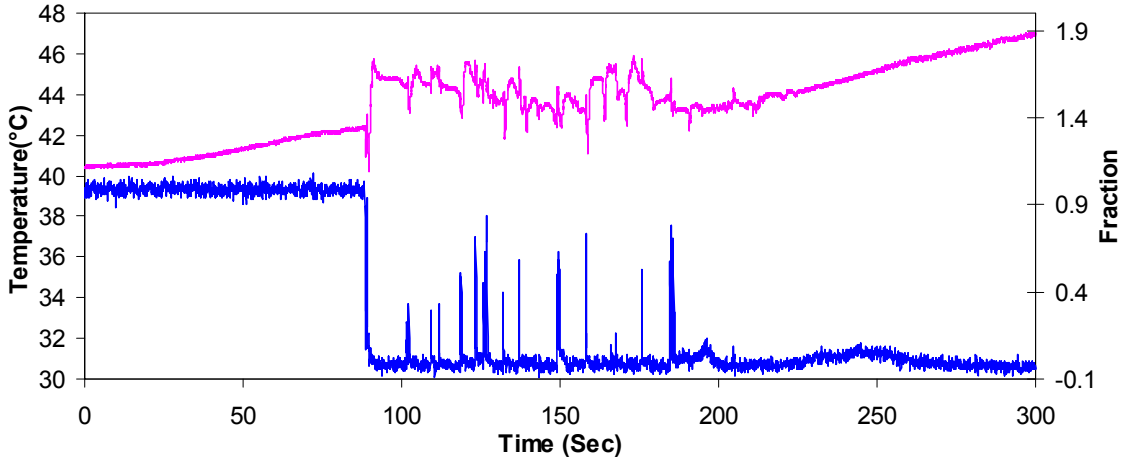

(c) Thermocouple number 10 in the adiabatic region

Figure 5.31. The liquid fraction data and temperature data from the transient test of the water-OHP with 50 Watts heat input.

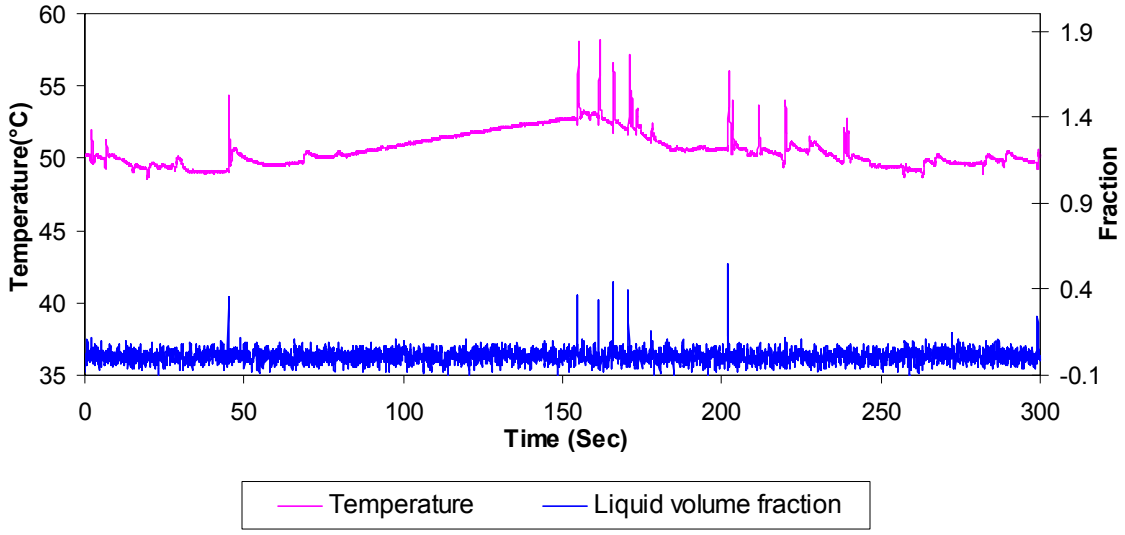

(a) Thermocouple number 16 in the evaporator

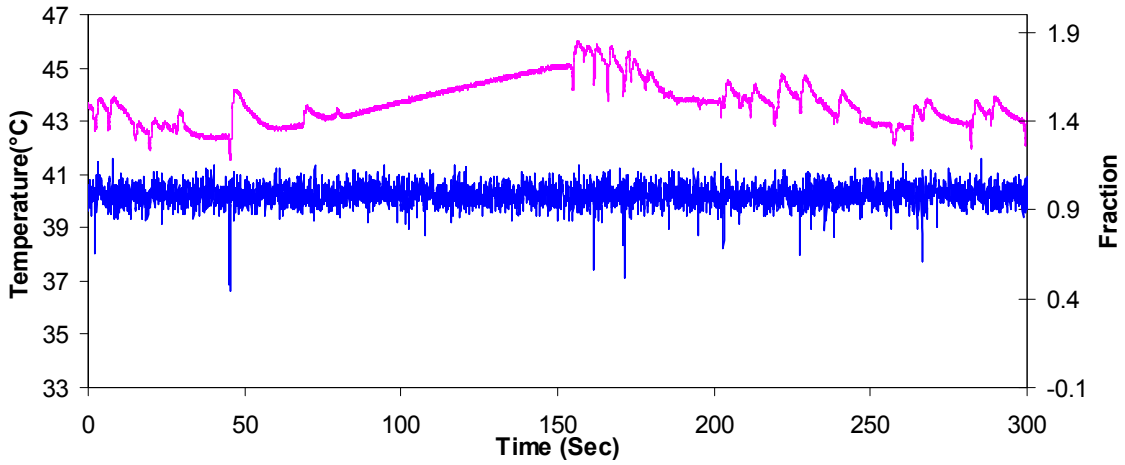

(b) Thermocouple number 2 in the condenser

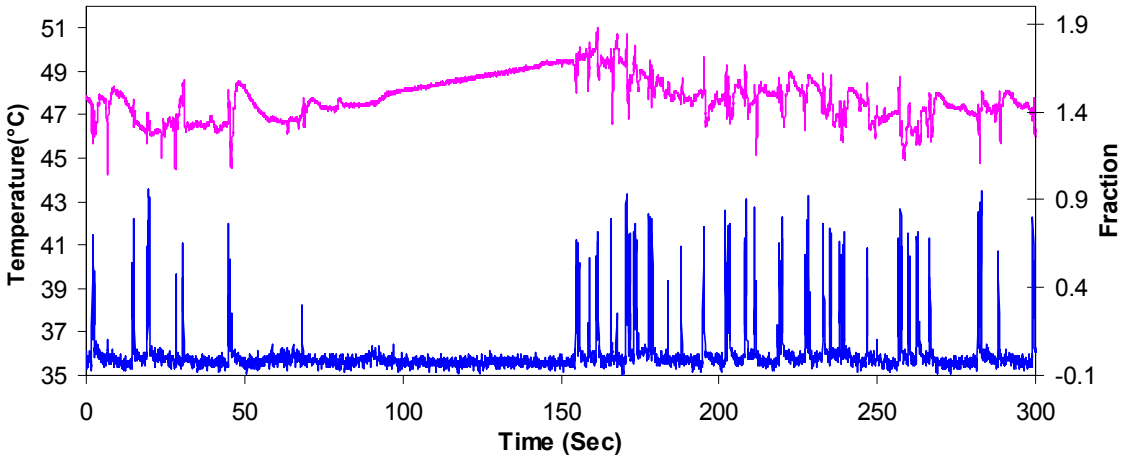

(c) Thermocouple number 10 in the adiabatic region

Figure 5.32. The liquid fraction data and temperature data from the steady-state test of the water-OHP with 50 Watts heat input.

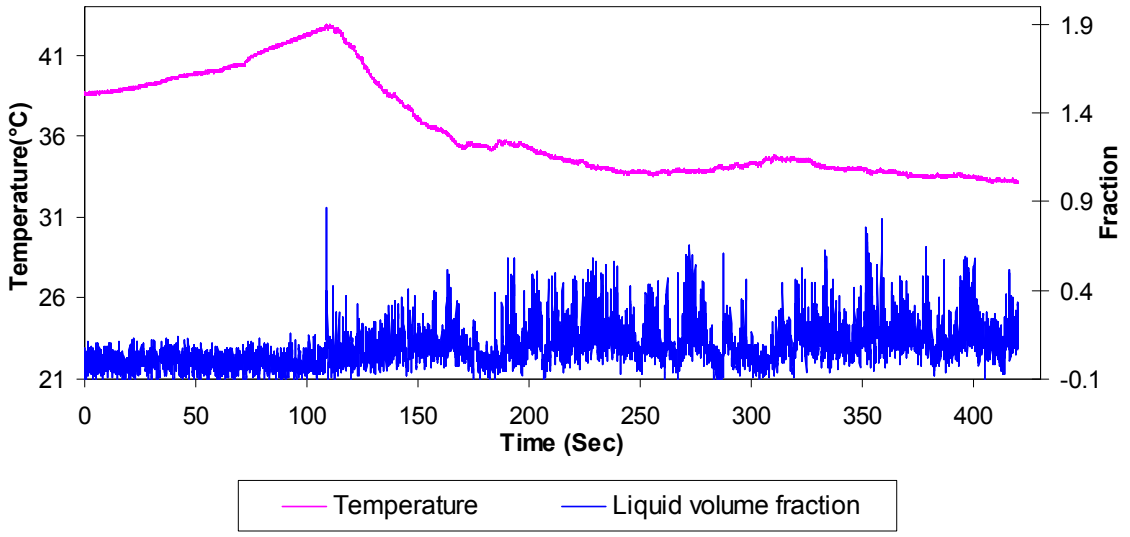

(a) Thermocouple number 16 in the evaporator

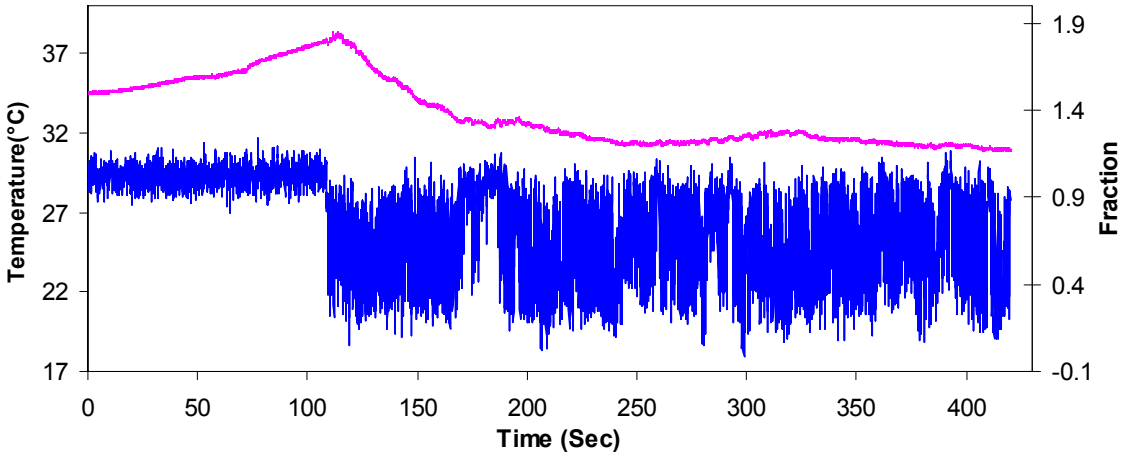

(b) Thermocouple number 2 in the condenser

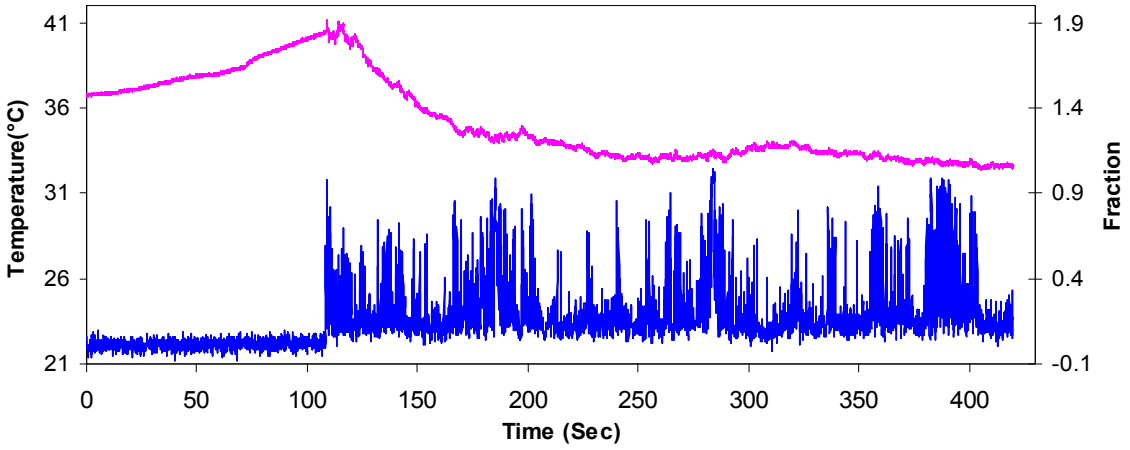

(c) Thermocouple number 10 in the adiabatic region

Figure 5.33. The liquid fraction data and temperature data from the transient test of the acetone-OHP with 51 Watts heat input.

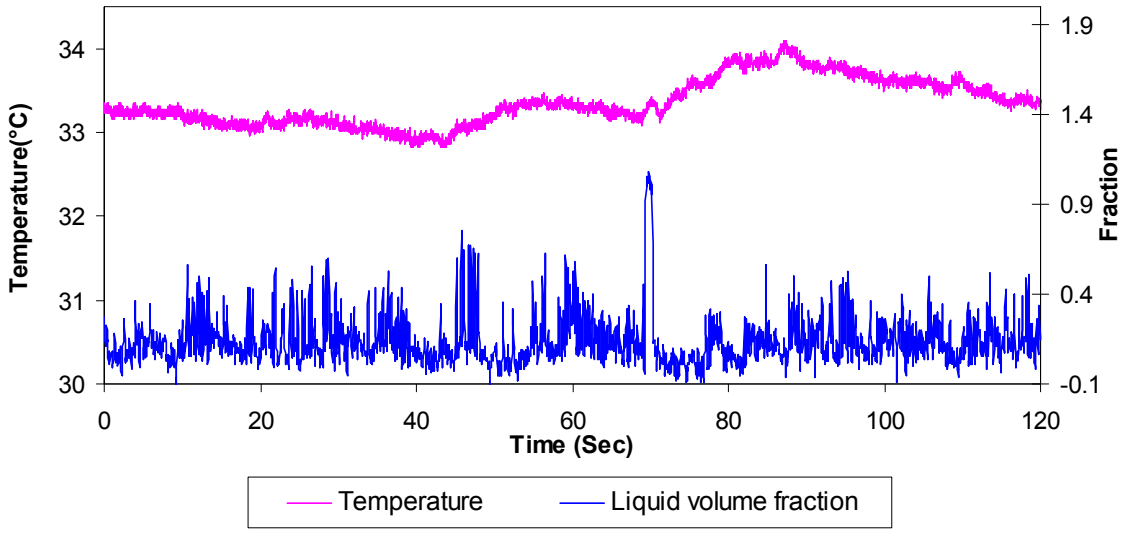

(a) Thermocouple number 16 in the evaporator

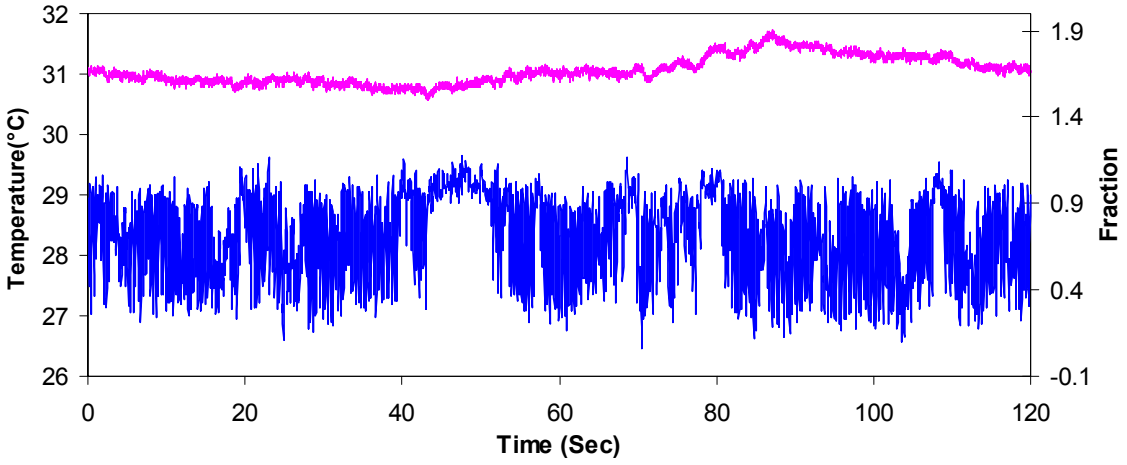

(b) Thermocouple number 2 in the condenser

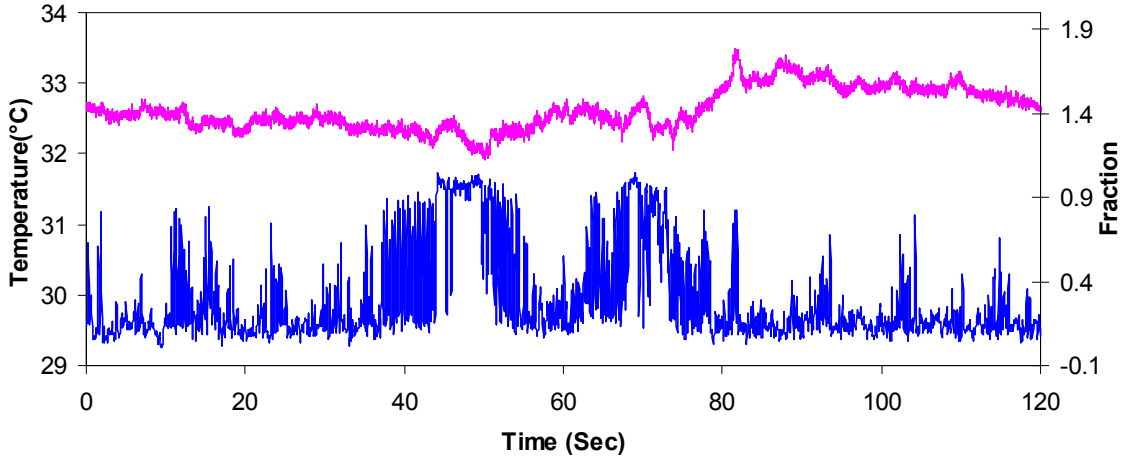

(c) Thermocouple number 10 in the adiabatic region

Figure 5.34. The liquid fraction data and temperature data from the steady-state test of the acetone-OHP with 51 Watts heat input.

To investigate the liquid circulation through the whole pipe, liquid volume fraction data at the end area of evaporator were calculated. Liquid in this region indicates that there is movement from one leg to another indicating circulation rather than just oscillation of the liquid. The end area of the evaporator is defined as shown in Figure 5.35. The calculated data for each heat input are shown in Tables 5.9 and 5.10. The plotted data are shown in Figure 5.36. Before the startup point for both the water-OHP and the acetone-OHP, and at macro-pause periods, liquid volume fraction at the end of evaporator is meaningless to know circulation. Thus, the data collected in Table 5.9 and 5.10 are from macro-action periods for each heat input test. The circulation in the acetone-OHP is much greater than in the water-OHP. This is also confirmed in watching the videos.

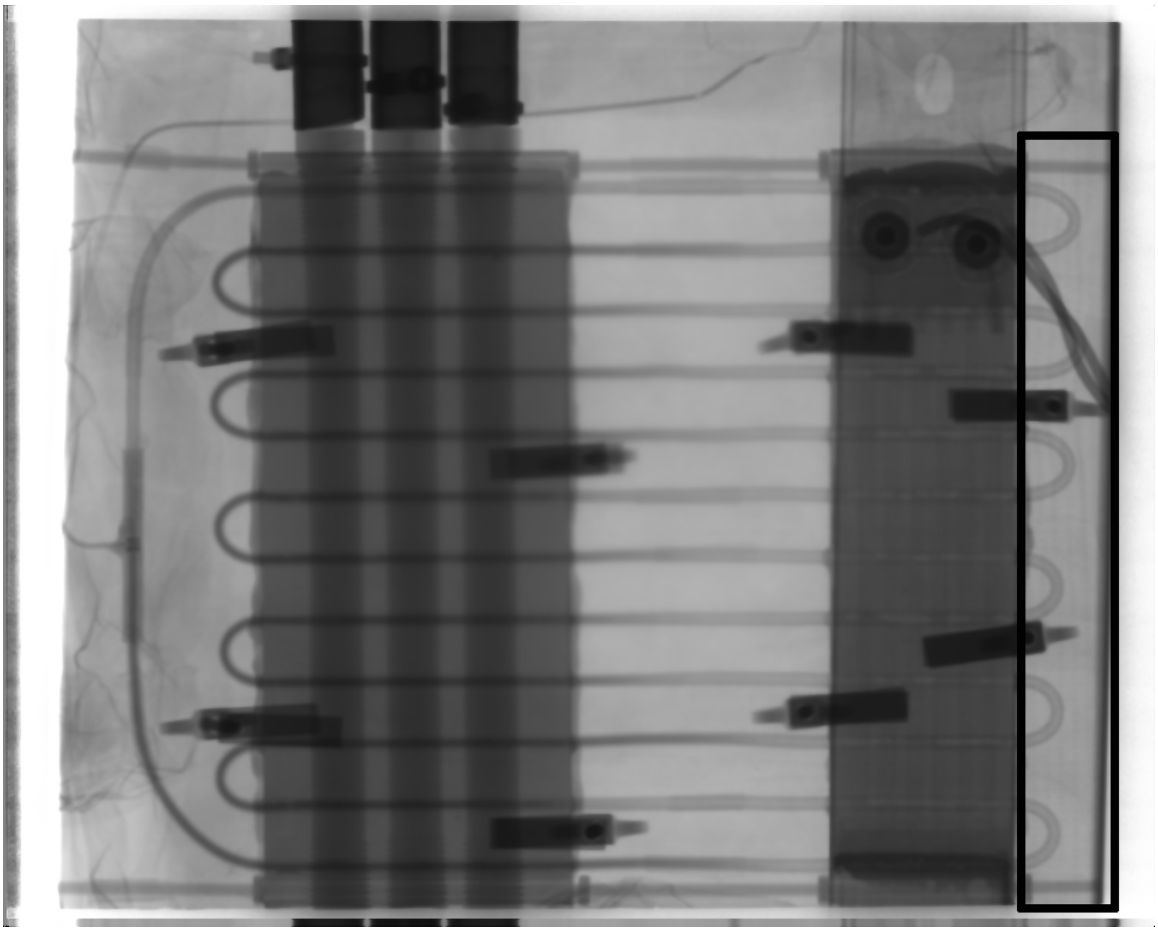

Figure 5.35. The end area of evaporator is defined to investigate the circulation of liquid through the whole pipe. The area within the box at the right side of the figure is the end area of evaporator.

Table 5.9. The liquid volume fraction data at the end of evaporator at each steady-state heat input for water-OHP

Heat input (Watts)	Type	Liquid volume fraction on the end of evaporator
50	Steady-state	0.0028
99	Steady-state	0.0016
149	Steady-state	0.0029
200	Steady-state	0.0072
300	Steady-state	0.0153

Table 5.10. The liquid volume fraction data at the end of evaporator at each steady-state heat input for acetone-OHP

Heat input (Watts)	Type	Liquid volume fraction on the end of evaporator
51	Steady-state	0.1399
73	Steady-state	0.1584

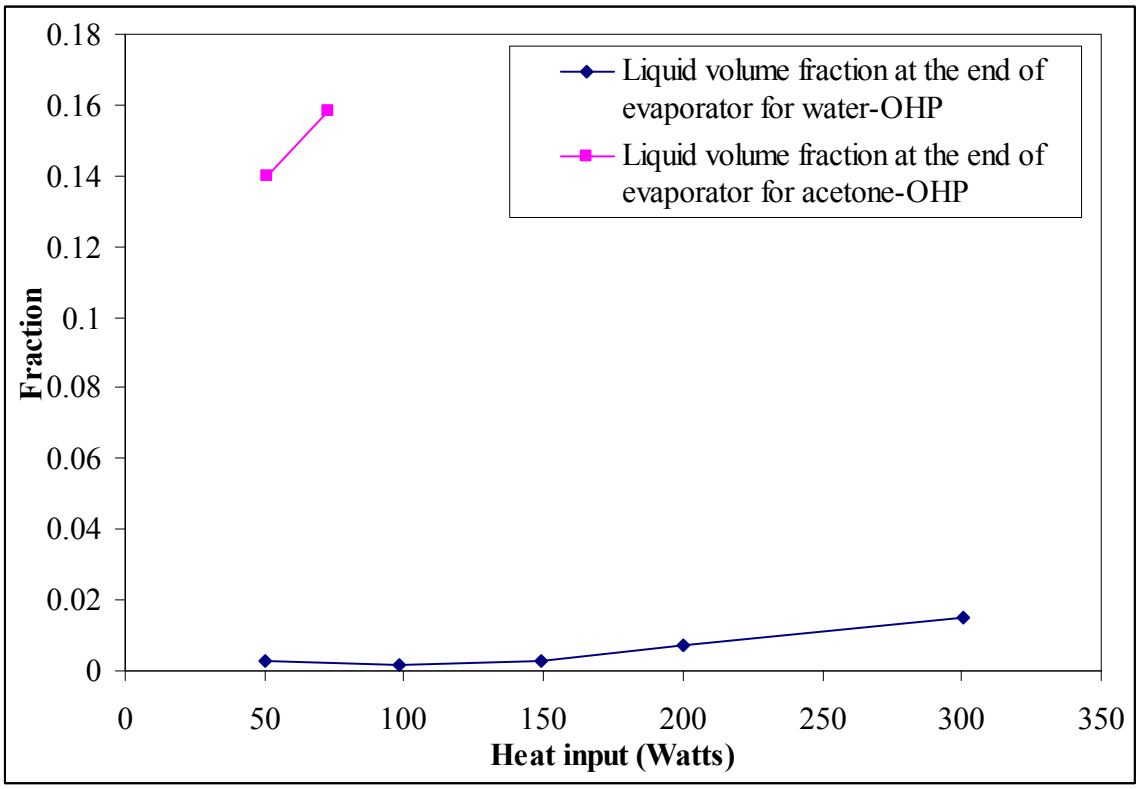

Figure 5.36. The plotted data of liquid volume fraction values at the end of evaporator at each steady-state heat input for water-OHP and acetone-OHP

Chapter 6 Discussion

6.1 Liquid movement with heat input

The behavior of the working fluids in the water-OHP and the acetone-OHP as heat is increased in a stair step fashion can be determined by examining video of the neutron imaging and liquid phase fraction information in the evaporator with time (Figures 5.10 to 5.27) and time-averaged phase fraction data (Figures 5.1 to 5.6). For the water-OHP, when 26 Watts heat input is first applied the neutron video shows that the liquid is slowly pushed out of the evaporator. Figure 5.10 shows that the liquid fraction in the evaporator goes lower than 0.01 the first time at 482.50 seconds. The liquid fraction at that point is 0.0098. Then, the value of liquid fraction is increased at the next frame. The total number of frames when liquid fraction in evaporator is below than 0.01 is 19 frames among 18,000 frames in this heat input test. According to the video, liquid is not expelled totally from the evaporator until the steady-state test at 26 Watts heat input. The liquid slugs move very slowly during this stage and the video must be watched carefully to see the motions. For the 26 Watts heat input steady-state test, the video shows that the liquid is expelled totally from the evaporator throughout the test.

On stepping the heat up to 50 Watts the liquid initially remains motionless and the temperature rises slowly in each section of the OHP. When the average temperature reaches about 47 °C in the evaporator, 39 °C in the condenser and 42 °C in the adiabatic region or a combined average of 42.74 °C for the whole heat pipe, the liquid can be seen to move in an intermittent fashion. This is the first startup point for water-OHP. The liquid slugs will temporarily enter the evaporator from the adiabatic section but quickly

reverse and leave the evaporator without going through the turns at the end of the evaporator. These entrances into the evaporator can be seen in Figure 5.28 as the peaks in the liquid fraction. After quickly entering and exiting the evaporator, the liquid typically remains relatively still resulting in the micro-pause periods shown in Figure 5.28. During the micro-pause periods the liquid in tubes adjoining each other and sharing a turn in the condenser will vibrate but will not move enough to cause liquid to enter the evaporator. At 50 Watts the water-OHP alternatively enters macro-action and macro-pause periods where the average temperature increases in each section during the macro-pause sections and decreases during the macro-action periods. In Figure 5.28 one can see that the average temperatures follow a similar pattern with each micro-action and micro-pause period.

For the transient test at 99 Watts heat input, one macro-action period is observed. Before the startup point, the liquid shows little movement in the condenser and adiabatic region and does not enter into the evaporator. After the startup point, it shows alternating micro-action and micro-pause periods. For the macro-action start, the average temperatures in the condenser, adiabatic region and evaporator are about 47, 51, and 55 °C, respectively (Figure 5.14). For the steady-state heat input test, the liquid shows micro-actions and micro-pauses alternatively from the start to the end. The average temperatures show movements corresponding to each micro-action event at both tests (Figure 5.15).

On stepping the heat input to 149 Watts, the liquid movements show micro-actions and micro-pauses. The average temperatures continue to show changes

corresponding to the micro-action events, but it is increasingly difficult to see this as the frequency of micro-action events has increased (Figure 5.17).

On stepping the heat input to 197 Watts (transient test) and 200 Watts (steady-state test), the micro-action periods are now almost continuous with only very short micro-pause periods where the evaporator has no liquid in it. The frequency of micro-action events is high enough that they can no longer be correlated with the average temperature fluctuations (Figure 5.19).

At 297 Watts (transient test) and 300 Watts (steady-state test) heat input the neutron video shows a nearly continuous presence of liquid in the evaporator which is also reflected in the liquid fraction in the evaporator plot of Figure 5.21.

The acetone-OHP behavior has some similarities to the water-OHP but also some differences. When 24 Watts of heat was initially applied there was a small amount of liquid in the evaporator. But, the liquid does not show active movement and the liquid in the evaporator slowly moves to the adiabatic region and the condenser (Figures 5.22 and 5.23).

On stepping the heat input to 51 Watts, the video shows the first startup point and movement of liquid becomes continuous. This is also reflected in the liquid fraction plot showing few micro-pause periods (Figure 5.24). The acetone-OHP either lacks this behavior or it occurs at a heat input between 24 and 51 Watts, a range which was not examined in these experiments. Liquid circulation through the entire length of the tubing is observed from this heat input and above.

On stepping to 73 Watts, temperatures are much steadier than for the water-OHP, probably due to greater movement of the fluids. At this heat input, it is hard to observe micro-pause periods as observed after the first startup point at 51 Watts.

At same heat input, acetone shows more active movement than water. At higher heat input, water begins to show similar movement to the acetone.

6.2 Average time gap per micro-action period

The average time gap per micro-action period was calculated. In Figures 6.1 and 6.2, micro-action periods for the first macro-action period and the second macro-action period at 50 Watts steady-state heat input for the water-OHP are shown, respectively. In Figures 6.3 and 6.4, micro-action periods for transient and steady-state tests at 99 Watts heat input are shown. From Figures 5.28, 6.1, 6.2, 6.3 and 6.4, the time at each peak indicated by an arrow was collected and the time gap for each peak was calculated. The average time gaps per micro-action period were also obtained, for transient and steady-state tests at 149 Watts and the transient test at 197 Watts and the steady-state test at 200 Watts heat input. The average time gap between micro-action periods are shown in Table 6.1. From this data, we see that, at similar heat input, micro-actions occur regularly although they do not occur with exactly the same time gap. It is also seen that micro-actions occur more frequently as the heat input is increased. The data for the transient test at 297 Watts and the steady-state test at 300 Watts heat input for the water-OHP and for all heat inputs for the acetone-OHP were not considered because it is hard to define micro-actions for these tests.

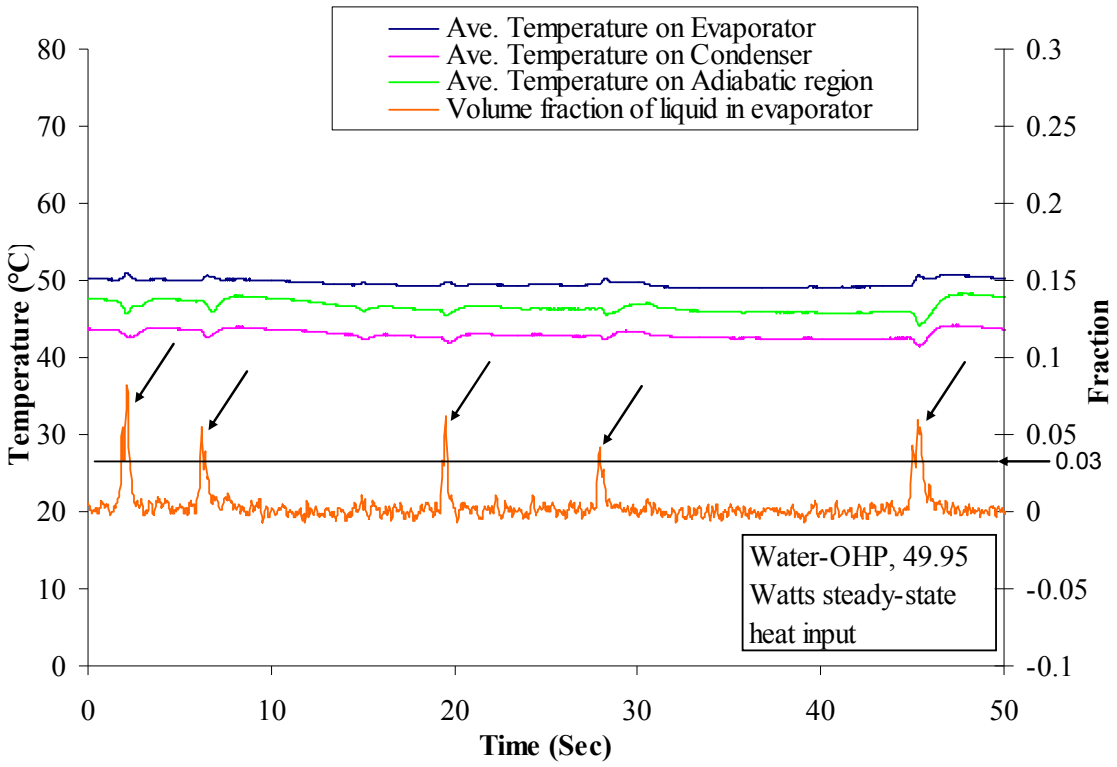

Figure 6.1. The micro-action periods and micro-pause periods in the first macro-action period in the steady-state test at 50 watts heat input for the water-OHP. The horizontal line indicates that the volume fraction of liquid in the evaporator is 0.03. The data above this line, indicated by arrows, are micro-action periods and data below the line are micro-pause periods.

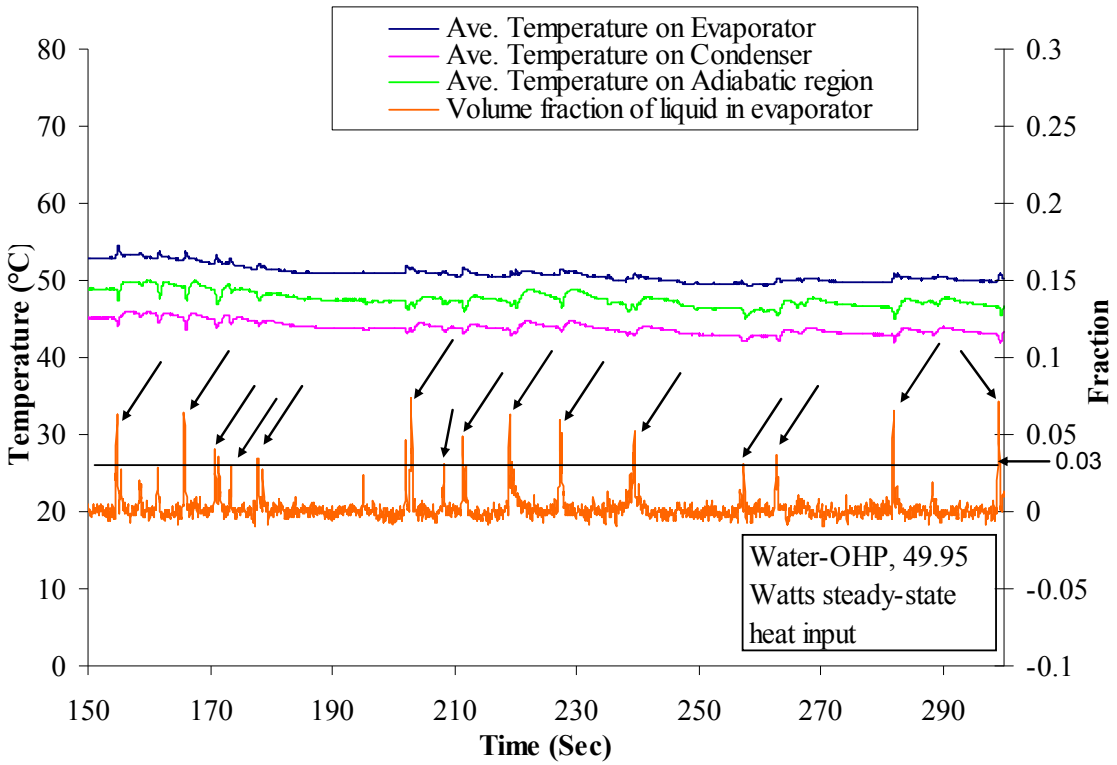

Figure 6.2. The micro-action periods and micro-pause periods in the second macro-action period for the steady-state test at 50 watts heat input for the water-OHP. The horizontal line indicates that the volume fraction of liquid in the evaporator is 0.03. The data above this line, indicated by arrows, are micro-action periods and data below the line are micro-pause periods.

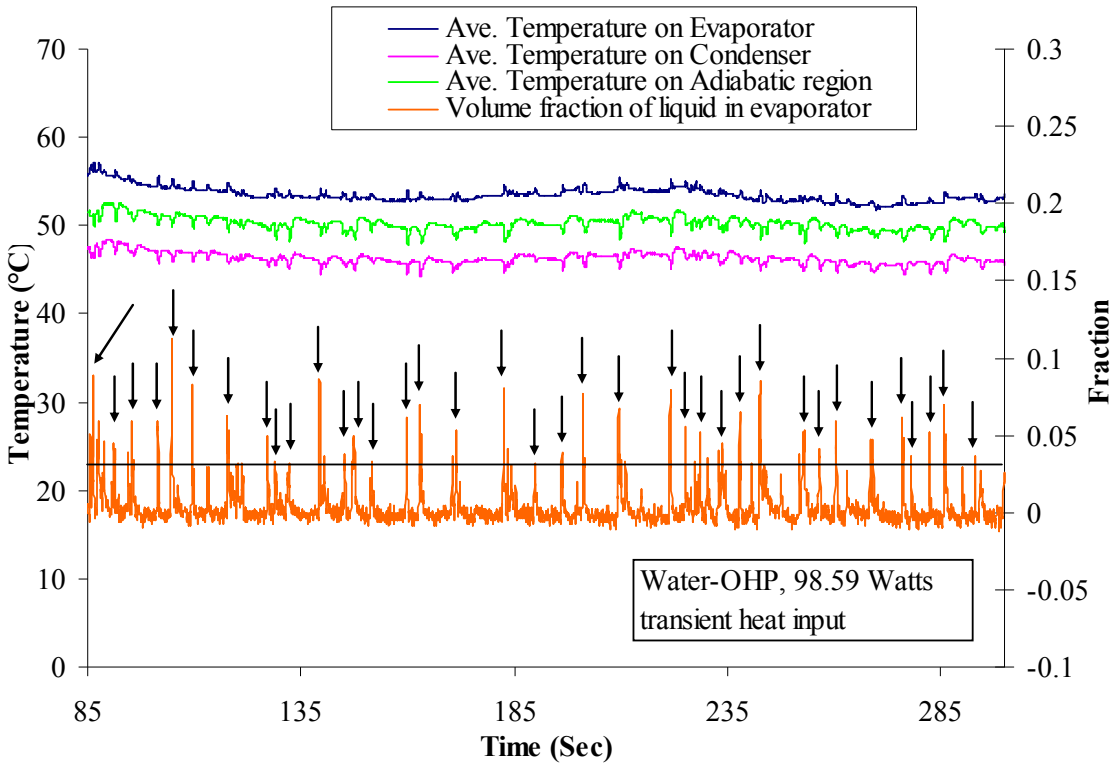

Figure 6.3. The micro-action periods and micro-pause periods for the transient test at 99 Watts heat input for the water-OHP. The horizontal line indicates that the volume fraction of liquid in the evaporator is 0.03. The data above this line, indicated by arrows, are micro-action periods and data below the line are micro-pause periods.

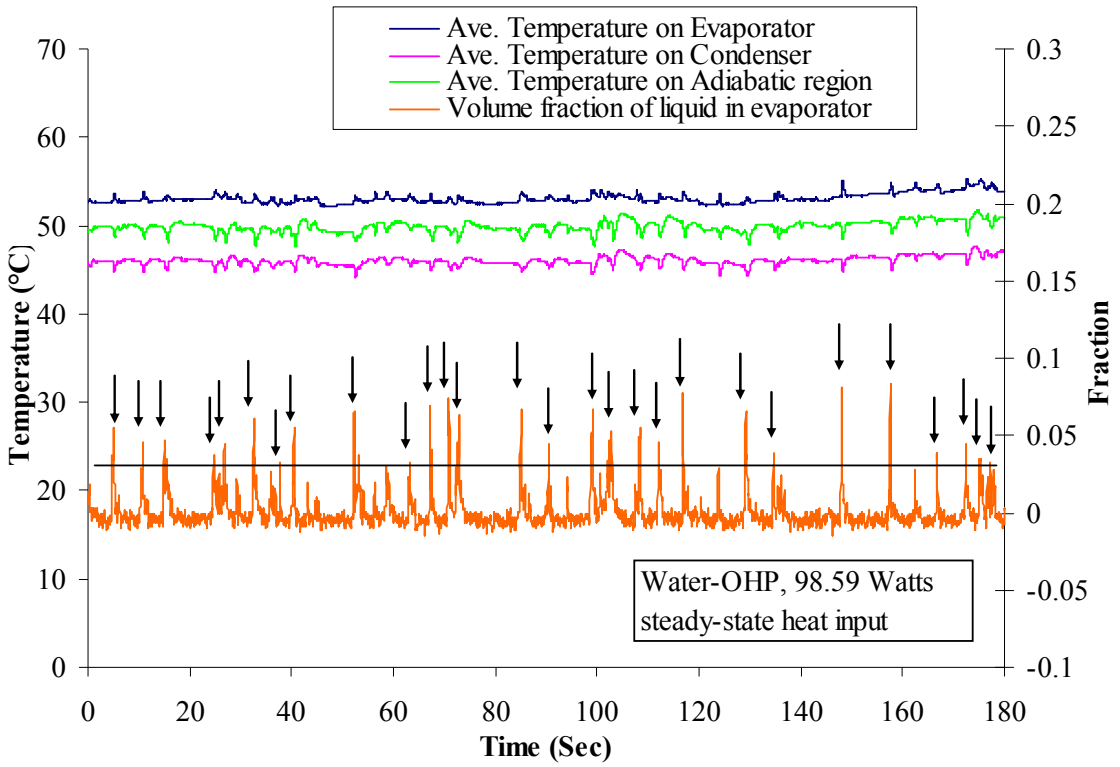

Figure 6.4. The micro-action periods and micro-pause periods for the steady-state test at 99 Watts heat input for the water-OHP. The horizontal line indicates that the volume fraction of liquid in the evaporator is 0.03. The data above this line, indicated by arrows, are micro-action periods and data below the line are micro-pause periods.

Table 6.1. The average time gap per micro-action period for selected heat input.

Liquid	Heat input (Watts)	Test	Order of macro-action period	Number of micro-action periods	Average time gap per micro-action period (seconds)	Standard deviation
Water	50	transient	1	12	8.72	4.46
Water	50	steady-state	1	5	10.79	5.00
Water	50	steady-state	2	15	10.31	6.79
Water	99	transient	1	37	5.75	2.60
Water	99	steady-state	1	28	6.38	3.48
Water	149	transient	1	64	4.74	2.02
Water	149	steady-state	1	30	4.05	2.04
Water	197	transient	1	53	3.38	1.78
Water	200	steady-state	1	47	2.57	1.74

6.3 Time-averaged phase fraction data

As the heat input was increased, the liquid was largely pushed out of the evaporator to the condenser and adiabatic region. In Table 5.1 it was shown that, for the water-OHP, the volume fraction of liquid is 0.005 in the evaporator, 0.745 in the condenser, and 0.589 in the adiabatic region at 26 Watts heat input. This means that at the relatively low heat input of 26 Watts, the liquid and vapor were already mainly distributed in the condenser/adiabatic region and the evaporator, respectively. At this stage, little or no movement of the liquid was observed. Any observed liquid motions were quite slow. The liquid volume fraction was 0.005 in the evaporator and 0.745 in the condenser at 26 Watts and changed to 0.002 in the evaporator and 0.886 in the condenser at 50 Watts. This means that, while there was little to no liquid in the evaporator, there are some vapor sections in the condenser. At higher heat input, 50 Watts, the amount of vapor in the condenser was smaller than at 26 Watts heat input. It is inferred that this is caused by the difference in the coefficients of thermal expansion between the vapor and liquid phases. Because the vapor has higher coefficient of thermal expansion, it expands more than the liquid in the evaporator by the supplied heat and, as a result, it expels the liquid to the condenser and adiabatic region. In the acetone-OHP little to no movement of the liquid in the tubing was observed, just like the water-OHP before the startup point.

The first startup points for both the water-OHP and acetone-OHP were observed during the transient response to approximately 50 Watts heat input. The evaporator and condenser were mainly occupied by vapor and liquid, respectively, before the startup points, that is, during the pre-startup period both the water and the acetone have little movement. During this pre-startup period, average temperatures on the evaporator,

condenser and adiabatic regions go up slowly and gradually. Thus, it is inferred that, although the vapor and liquid are distributed to the evaporator and condenser by a built up pressure difference, there is no temperature decrease in the OHP before the liquid in the tubing starts to move actively. In other words, observed temperature decreases are related with active movement of the working liquid in the OHPs regardless of its fluid, water or acetone.

In Figure 5.2, it was shown that for the acetone-OHP the liquid volume fraction in the evaporator is higher than that of the water-OHP at a heat input of approximately 50 Watts. It is expected that this same behavior also occurs at approximately 75 Watts heat input, although there are no data for the water-OHP at approximately 75 Watts. This result is caused because the acetone moves more actively than the water at the same heat input, so that it enters the evaporator more frequently than the water does. This phenomenon is also shown well in Figure 5.6. At approximately 50 Watts heat input, the ratio of volume of liquid in the evaporator to the volume of liquid in the entire pipe is much lower than the ratio of volume of liquid in condenser to volume of liquid in entire pipe for both the water-OHP and the acetone-OHP. It is speculated that this behavior difference between the acetone-OHP and the water-OHP is mainly caused by their viscosity difference. The viscosity of acetone is lower than the viscosity of water, so acetone can be more easily moved than water at relatively low heat input. In other words, acetone can be moved more actively than water at the same heat input. It is estimated that some other factors such as density and vapor pressure also contribute the more active movement of acetone (discussed further in section 6.9).

6.4 Startup points

Only three macro-action starts were observed for the water-OHP and one for the acetone-OHP in this work. The first startup point for the water-OHP occurred at an average temperature of 42.8 °C at 88.8 seconds after raising the heat input from 25.61 to 50 Watts and for the acetone-OHP it occurred at an average temperature of 40.5 °C at 108.7 seconds after raising the heat input from 24 to 51 Watts. The difference of time taken to be occurred is possibly explained by thermal conductivity for water and acetone. That is, time for water is shorter than time for acetone because of higher vapor and liquid thermal conductivities of water.

These average temperatures are an average of thermocouples 1 through 22; thermocouples 23 and 24 were excluded from these averages as they are on the long outer loop of the OHPs. For the water-OHP at the first startup the evaporator, condenser, and adiabatic region had average temperatures of 46.90, 41.81, and 39.31 °C, respectively. For the acetone-OHP at the first startup the evaporator, condenser, and adiabatic region had average temperatures of 43.15, 40.59, and 37.82 °C, respectively. The average temperature comes from thermocouples 1 to 8 for the condenser, from thermocouples 9 to 14 for the adiabatic region, and from thermocouples 15 to 22 for the evaporator.

For the third macro-action start, during the 50 Watts steady-state test for the water-OHP, the condenser, adiabatic region, and evaporator had average temperatures of 45.07, 48.81, and 53.01 °C, respectively. The fourth macro-action start occurred during the 99 Watts transient test for the water-OHP and showed temperatures of 47.48, 51.58, and 55.86 °C in the condenser, adiabatic region, and evaporator, respectively. (Table 6.2)

These results are explained by the fact that acetone moves more actively than water at the same heat input.

Table 6.2 Temperatures and time at startup points

OHP	Macro -action Period	Heat Input (Watts)	Test Type	Evaporator (°C)	Condenser (°C)	Adiabatic (°C)	Total (°C)	Time (sec)
Water	1	50	Transient	46.9	41.81	39.31	42.8	88.8
Water	3	50	Steady -state	53.01	45.07	48.81	48.98	-
Water	4	99	Transient	55.86	47.48	51.58	51.64	-
Acetone	1	99	Transient	43.15	40.59	37.82	40.5	108.7

6.5 Performance of OHP

In Figure 5.8, the relationship between the volume fraction of liquid in the evaporator and the heat transfer coefficient was shown. At zero heat input, the liquid volume fraction in the evaporator is a result of factors other than the heating of testing that occurred before that test and hence are probably not meaningful. At approximately 25 Watts, the liquid volume fraction in the evaporator and heat transfer coefficient are nearly the same for the water-OHP and the acetone-OHP. In both cases the liquid is pushed out of the evaporator and is not actively moving. The heat transfer coefficient does not depend on the moving fluid and is equivalent for the two OHPs. As the heat input is increased, the water-OHP shows a steady increase in heat transfer coefficient. Above 25 Watts heat input, though, the acetone-OHP shows a higher heat transfer coefficient than the water along with a higher volume fraction of liquid in the evaporator, reflecting more active movement of the acetone within the OHP.

6.6 Average temperature data and the liquid volume fraction in the evaporator

Figures 5.10 to 5.27 show the relationship between the average temperature data for the evaporator, condenser and adiabatic regions and the liquid volume fraction in the evaporator for the water-OHP and acetone-OHP. From the startup point to the end of the steady-state test at 149 Watts heat input for the water-OHP, each time there is peak in the liquid fraction data (liquid entering the evaporator from the adiabatic region) there is also steep change in the temperature data. Thus, it can be inferred that the steep temperature change of the OHP is related with the liquid movement, possibly evaporation of liquid in the evaporator causing a pressure rise in the whole heat pipe which compresses the vapor causing a temperature rise. For the transient test at 197 Watts heat input, this tendency, the relation between liquid fraction change and temperature change, is weakened. For the steady-state test at 200 Watts, the transient test at 297 Watts, and the steady-state test at 300 Watts, it is hard to observe this behavior because the liquid fraction and temperature changes are too chaotic. Micro-pause regions are necessary to observe the behavior. For the acetone-OHP, this tendency is observed, but it is not shown clearly because the liquid fraction and temperature changes are too chaotic and there are very few micro-pause periods. Figures 5.10, 5.11, and 5.24 also show that the overall temperature is increased when there is little or no liquid movement prior to the first startup points for the water- and acetone-OHPs.

The liquid volume fraction in the evaporator is compared to the temperature difference between the evaporator and the condenser for the transient test at 50 Watts heat input in Figure 6.5 for the water-OHP. In this figure, the temperature difference increases when the liquid has no or little movement, but when the liquid moves actively,

the temperature difference decreases overall although some peaks occur in the temperature data. The peaks in the temperature data coincide with peaks in the liquid fraction data. To understand how the peaks are produced in the temperature data, the average temperature of the evaporator, condenser and adiabatic regions are plotted with the liquid volume fraction in the evaporator in Figure 6.6. From this figure, it is observed that the average temperatures of the evaporator, condenser and adiabatic regions each increase when a peak in the volume fraction data occurs, i.e., when liquid enters the evaporator. To analyze this in more detail, a small section of time in Figure 6.6 is magnified in Figure 6.7. In this figure, when there is a peak in the liquid fraction data, the average temperature of the evaporator increases while the average temperatures of condenser and adiabatic regions decrease initially but then increase above their values before the liquid entered the evaporator. All the individual thermocouple data for the evaporator and condenser in Figure 6.7 are displayed in Figure 6.8. It is shown that the temperature data for individual thermocouples in the condenser are relatively uniform, but those for the evaporator are not. Only some of thermocouples in the evaporator contribute the initial temperature increase. In this figure, thermocouples 16, 17, 18 and 21 contribute the initial temperature increase. After the initial increase, all the thermal couples in the evaporator contribute the later temperature increase. It is inferred that this initial increase is associated with vapor and liquid movement in tubes, but the movement of the liquid in the tubes is chaotic and difficult to analyze. An initial temperature decrease and later overall temperature increase of temperature in the condenser are observed too. In the case of the condenser temperature, it is shown that all the thermocouples contribute to the initial temperature decrease and increase uniformly. The

temperature rise in the condenser might be due to an increase in pressure inside the OHP due to evaporation of liquid that enters the evaporator. The rise in pressure will compress the vapor throughout the OHP increasing its temperature. This may increase the heat transfer to the cooling fluid within the condenser from increased condensation due to the pressure rise and increased conduction due the temperature rise.

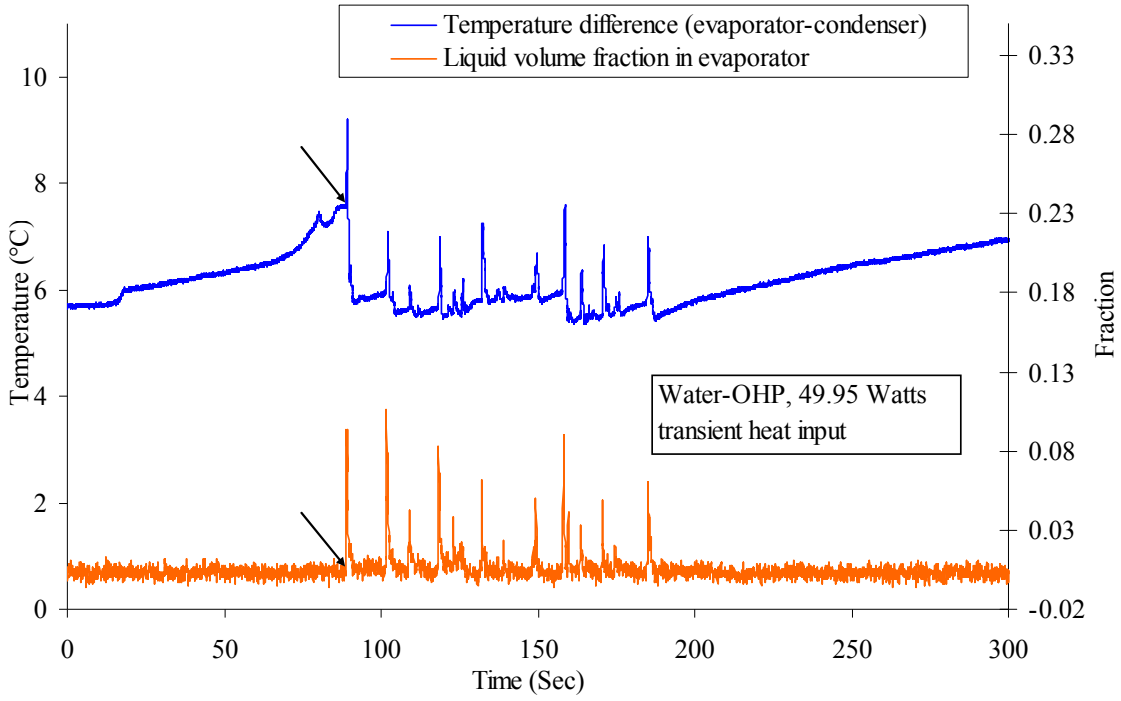

Figure 6.5. The data of temperature difference and liquid volume fractions are shown. The two arrows indicate the startup point.

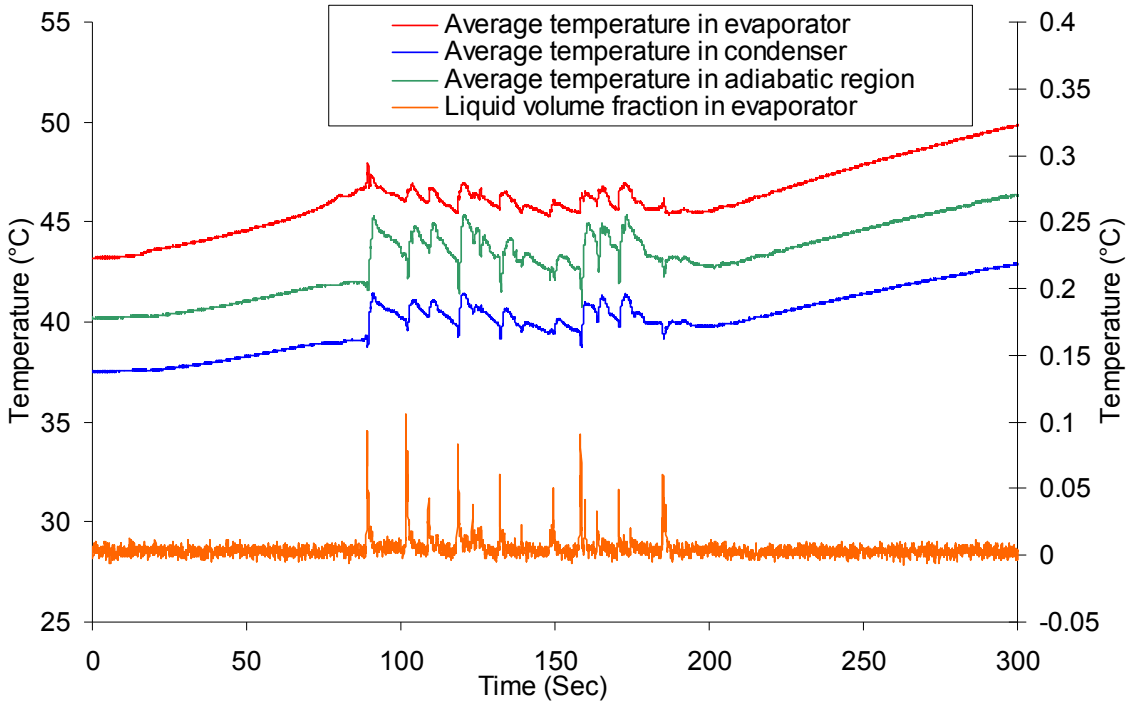

Figure 6.6. The data of average temperatures at evaporator, condenser and adiabatic region and liquid volume fractions are shown.

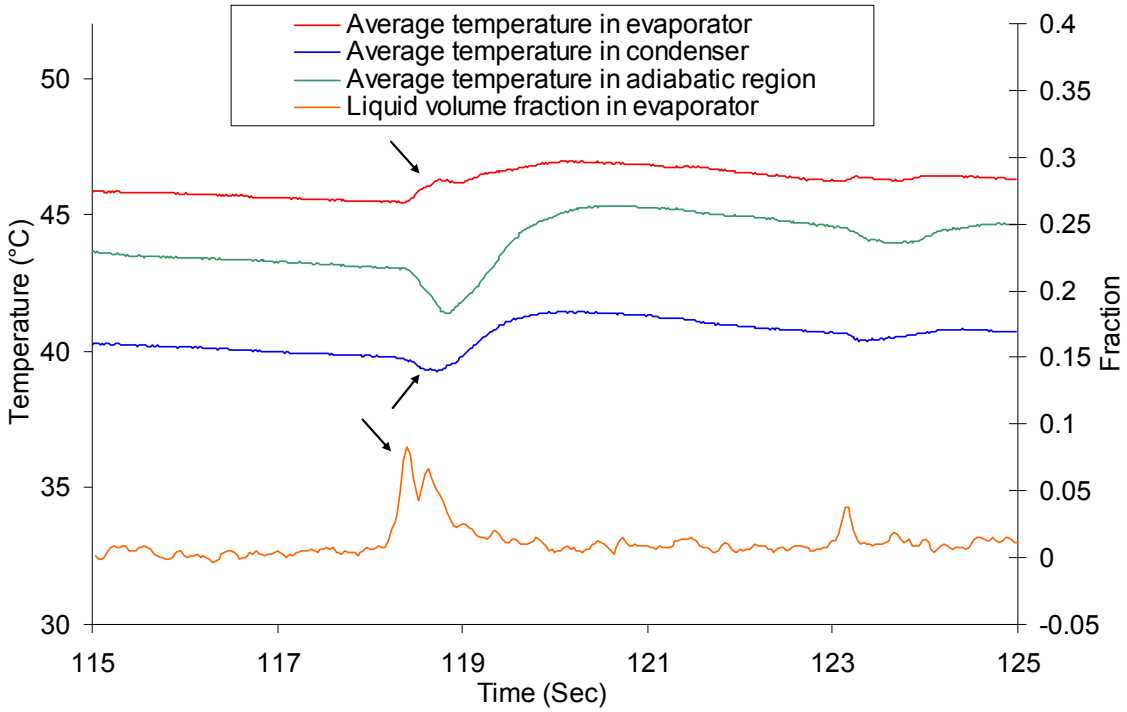

Figure 6.7. The magnified data of average temperatures at evaporator, condenser and adiabatic region and liquid volume fractions are shown. When there is steep change in liquid fraction data, there are also steep changes in temperature data. The average temperatures at condenser and adiabatic regions are decreased while the average temperature at evaporator is increased. After about 0.5 seconds, the decreased temperatures at condenser and adiabatic regions are increased higher that previous temperatures.

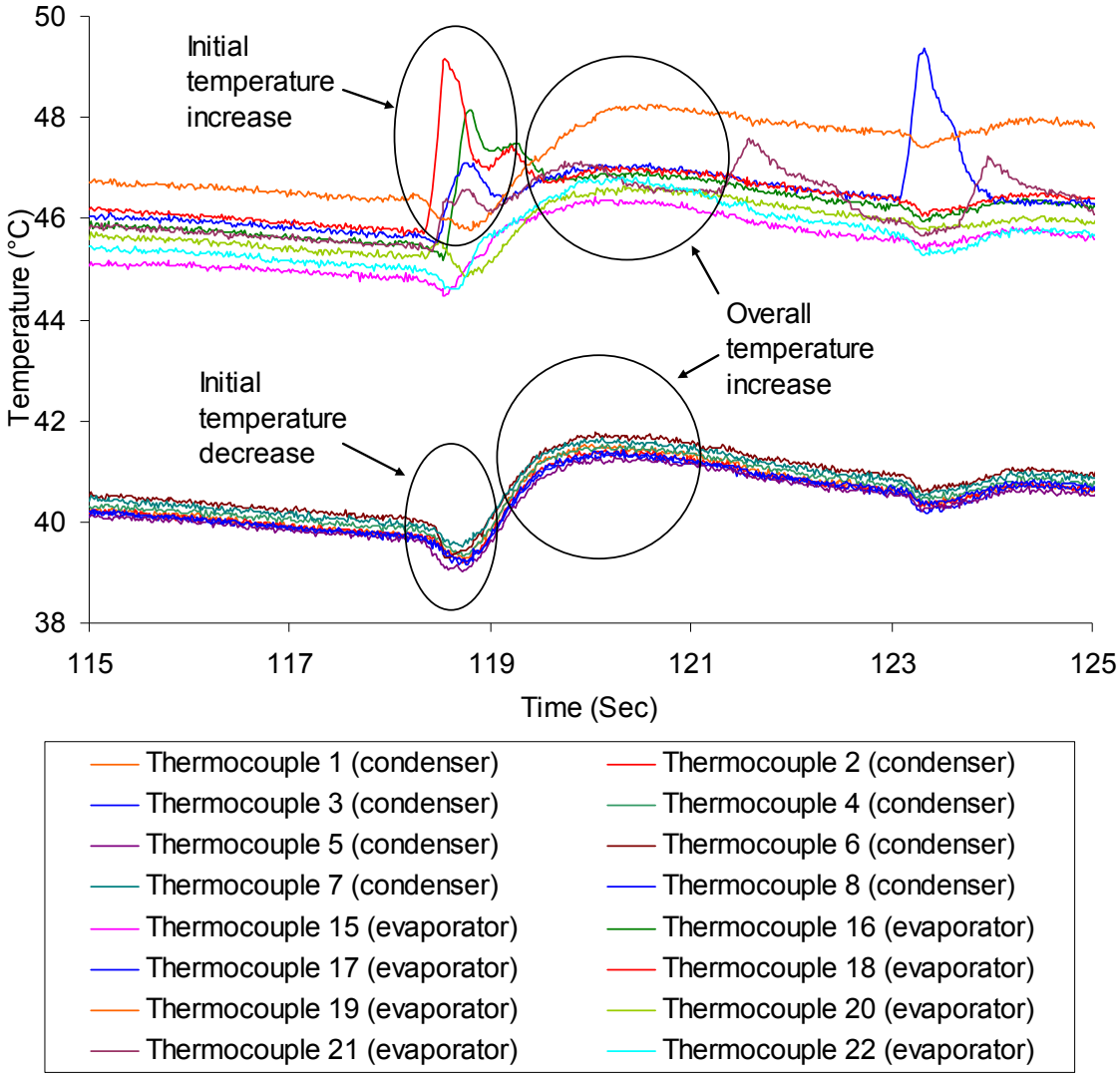

Figure 6.8. The temperature data for individual thermocouples are shown. All the individual temperature data at condenser show same temperature change, decreased at first and increased higher than previous level, while some temperatures at evaporator shows initial temperature increases and others are decreased at first and increased higher than previous level.

Figures 6.9 and 6.10 show the plotted data of temperature difference between evaporator and condenser and liquid volume fraction in evaporator for the steady-state test at 50 Watts and the transient test at 99 Watts heat input for the water-OHP. From Figures 6.5, 6.9 and 6.10, it is shown that the temperature difference is 7.6 °C, 7.9 °C and 8.38 °C when liquid starts to enter to the evaporator, i.e., at the startup point. (Table 6.3)

Those three values are close each other. It is also shown that temperature difference increases as the heat input is increased, though the differences may be too small to be significant. Thus, it is recommended to investigate temperature differences when the liquid starts to move into the evaporator for the further studies.

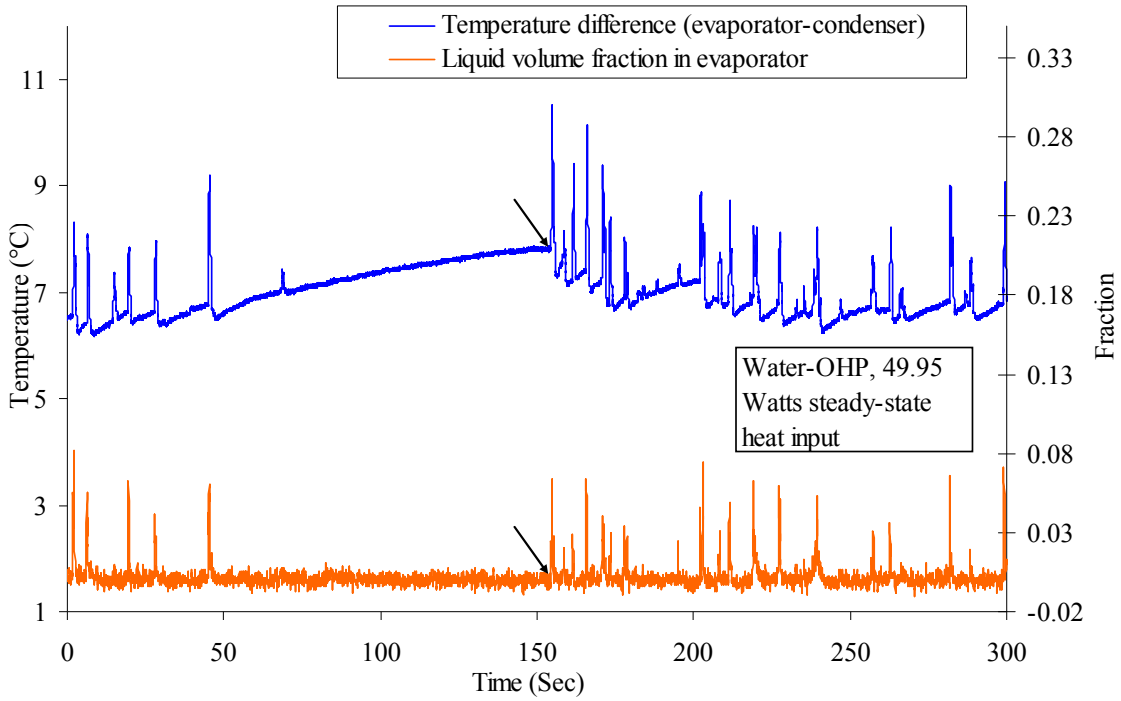

Figure 6.9. The temperature difference between the evaporator and condenser and the liquid volume fraction in the evaporator for the steady-state test at 50 Watts. The two arrows indicate the startup point.

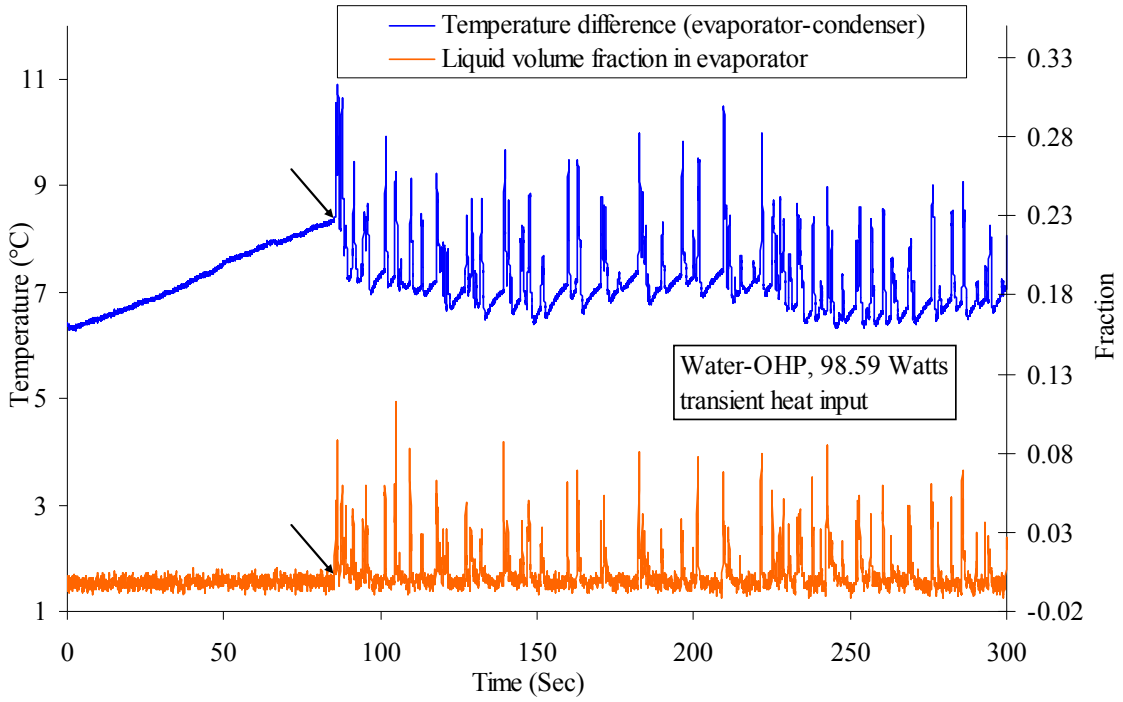

Figure 6.10 The temperature difference between the evaporator and condenser and the liquid volume fraction in the evaporator for the transient test at 99 Watts. The two arrows indicate the startup point.

Table 6.3 Data of temperature difference between evaporator and condenser at startup points

OHP	Macro -action Period	Heat Input (Watts)	Test Type	Evaporator (°C)	Condenser (°C)	Temperature Difference (°C)
Water	1	50	Transient	46.9	41.81	7.58
Water	3	50	Steady-state	53.01	45.07	7.94
Water	4	99	Transient	55.86	47.48	8.38

The movement of acetone in the OHP is more active compared to water at same heat input. A startup point also exists for the acetone-OHP, but the acetone once moving, moves more actively. For the heat input levels tested there were regular alternating macro-action and micro-pause periods for the acetone. Such behavior could possibly exist at heat inputs between 25 and 50 Watts though.

6.7 Individual temperature and fraction data for some thermocouples

Figures 5.31 to 5.34 show the temperature data and liquid volume fraction at three locations on a single tubing leg where the thermal couples were attached (evaporator, condenser, and adiabatic region). In these figures, it is hard to find direct correspondence between volume fraction and temperature data at individual thermocouple positions. For the water-OHP there abrupt changes in temperature sometimes correspond to changes in volume fraction at a location (a vapor-liquid interface moves past the location) and sometimes they do not. The changes in temperature do not seem to be caused simply by the motion of vapor-liquid interfaces past the thermocouple locations.

For the transient behavior of the acetone-OHP after application of 51 Watts of heat (Figure 5.33), we see a steady temperature rise while the liquid volume fraction stays steady followed by a temperature decrease after the active motion of the fluid begins. For the steady-state behavior of the acetone-OHP at 51 Watts heat input (Figure 5.34), we see no correspondence between the liquid volume fraction and the temperatures at individual thermocouple locations.

For the thermocouples on a single leg located on the evaporator, condenser, and adiabatic region, the temperature curves look similar even though the thermocouples are located centimeters apart and the fluid motions do not seem to couple them.

Figures 5.31 to 5.33 show the noise variation of the intensities when the tubing is fully occupied by vapor or fully occupied by liquid. The noise variation is the highest at the condenser and the lowest at the adiabatic region for each figure. This is because in the adiabatic region there are fewer attenuation factors (fiberglass insulation, aluminum foil, copper tube, and vapor or liquid in the tubes), while in the condenser, there are more

attenuation factors (copper block and cooling heavy water along with fiber glass insulation, aluminum foil, copper tube, and vapor or liquid in the tubes). Thus, the intensity in condenser is lower than the intensity in the adiabatic region. Because of the lower intensity, more noise is produced. To reduce the noise it would help to use materials that have lower neutron attenuation coefficients. Thus, using aluminum heating and cooling blocks would be recommended, instead of the copper blocks, for the next experiment.

6.8 Circulation of liquid in tubes

In Figure 5.36, the liquid fractions at the end of the evaporator where the turns are located are shown. From these data, the degree of liquid circulation though whole pipe is inferred. It is shown that acetone circulates through the whole heat pipe more than water at a similar heat input. As the heat input is increased, the liquid fraction at the end of evaporator is also increased for both the water-OHP and the acetone-OHP. This means that circulation behavior is strengthened. For the acetone-OHP, the circulation is increased steeply from the heat input change from 50 to 75 Watts. On the other hand, water does not show a steep change in circulation, although the circulation slowly increases as the heat input is increased. Actually, from 50 Watts to 100 Watts, the fraction is decreased little bit as the heat input is increased.

This shows coincidence with the previous data. That is, from the previous data, it is known that acetone moves more actively than water. Thus, it is estimated that the acetone circulates more than the water. The data in Figure 5.36 supports this estimation.

6.9 Effects of properties of water and acetone

The performance difference between the water-OHP and the acetone-OHP can be qualitatively explained by the differences in the fluid properties. Figures 6.11 to 6.18 show the vapor pressure, latent heat, density, viscosity, thermal conductivity and heat capacitance of water and acetone as a function of temperature.

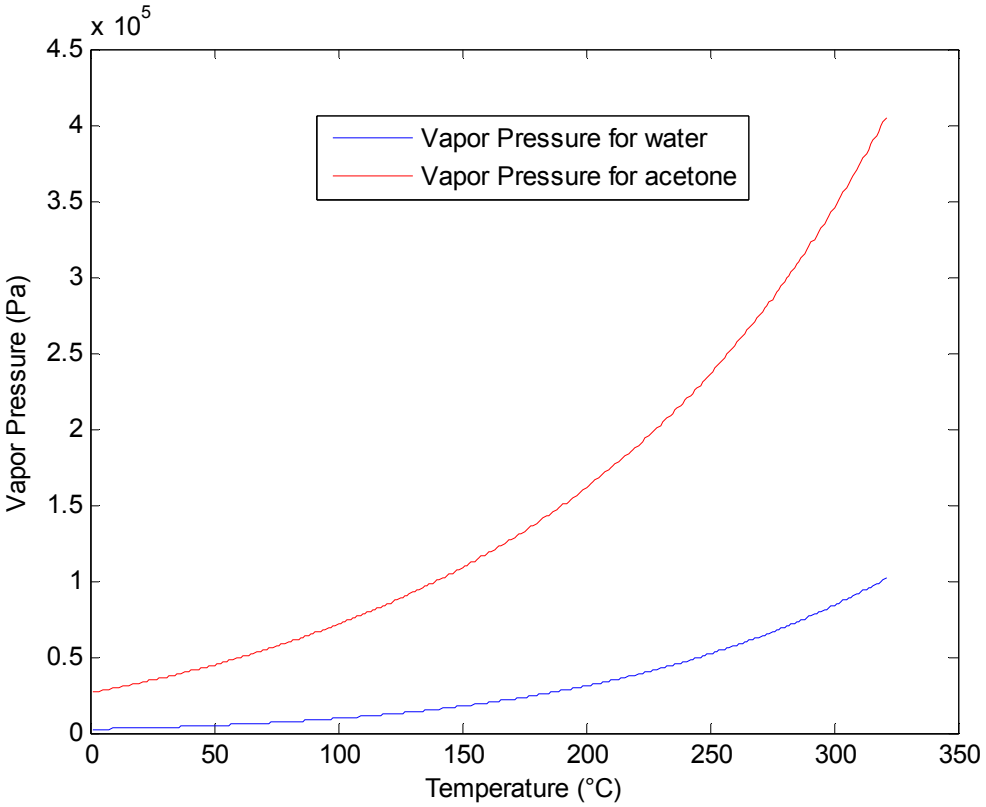

Figure 6.11. Vapor pressure with temperature variation for water and acetone.

From the previous discussion, it is inferred that the more active motion of liquid reduces the overall temperature difference between the evaporator and condenser in the heat pipe. Thus, it is also inferred that one factor in the performance of a heat pipe is related with the movement of liquid and that more active movement causes a better performance. The movement of liquid in the heat pipe is caused by the difference of pressure between evaporator and condenser. Thus, from the vapor pressure variation with

temperature (dp/dT) in Figure 6.11, it is inferred that, for the same temperature difference between the evaporator and condenser, there is a higher pressure difference in an acetone-OHP than in a water-OHP. Thus, the vapor pressure variation with temperature causes a more active fluid movement and favors a better performance in an acetone-OHP than in a water-OHP.

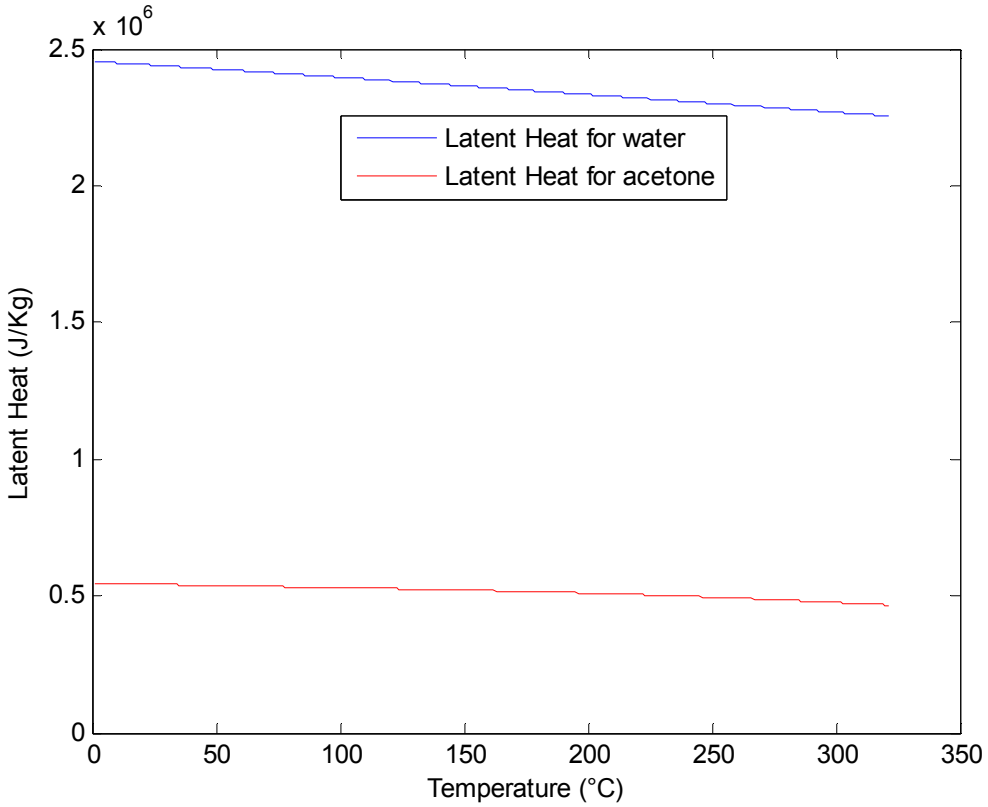

Figure 6.12. Latent heat with temperature variation for water and acetone.

The graph in Figure 6.12 shows the latent heat variation for water and acetone with temperature. The fluid that has a higher latent heat absorbs more heat when it evaporates than one that has lower latent heat. Thus, the water absorbs more heat than acetone when the liquid evaporates. This factor favors the performance of water in an OHP over acetone. But, in these studies, with the heat input between 25 Watts and 75

Watts, the acetone-OHP shows better performance. So, it is inferred that the latent heat is not a dominant factor for the better performance of a heat pipe at these heat input levels.

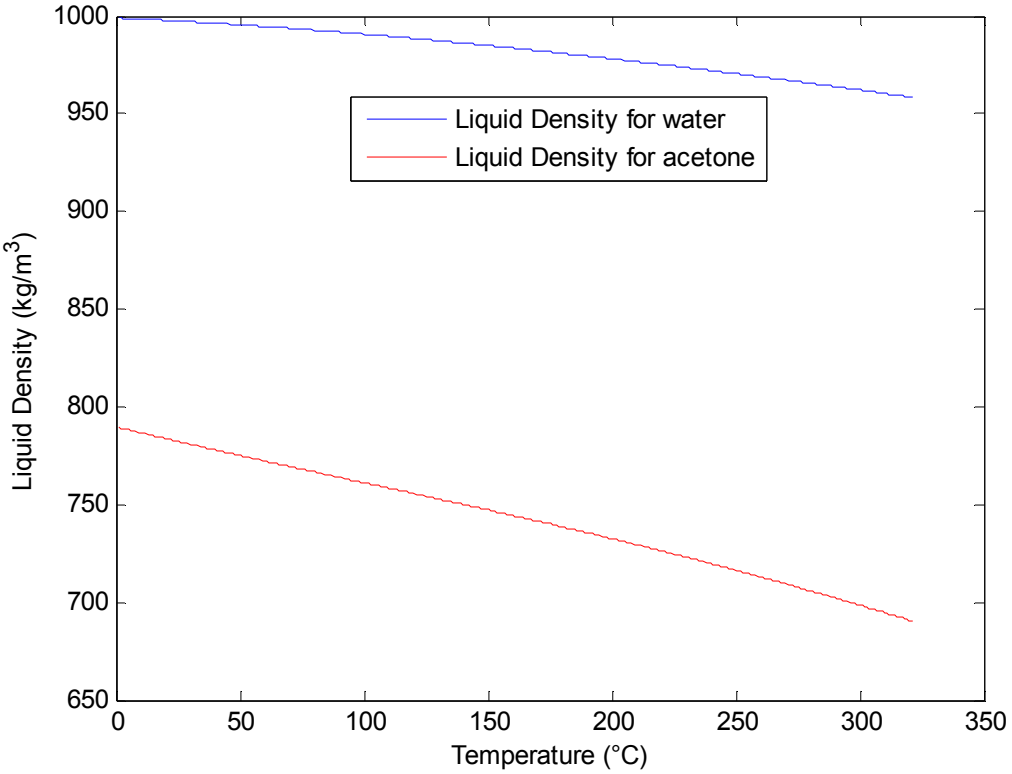

Figure 6.13. Liquid density with temperature variation for water and acetone.

Figure 6.13 shows the density of water and acetone with temperature. Higher density will produce liquid slugs of greater mass, so, it is inferred that a higher density fluid will have more resistance to flow in the tubing of an OHP. Thus, water will have more resistance to flow in the tube, all other things being equal. Density will favor acetone in fluid movement and OHP performance.

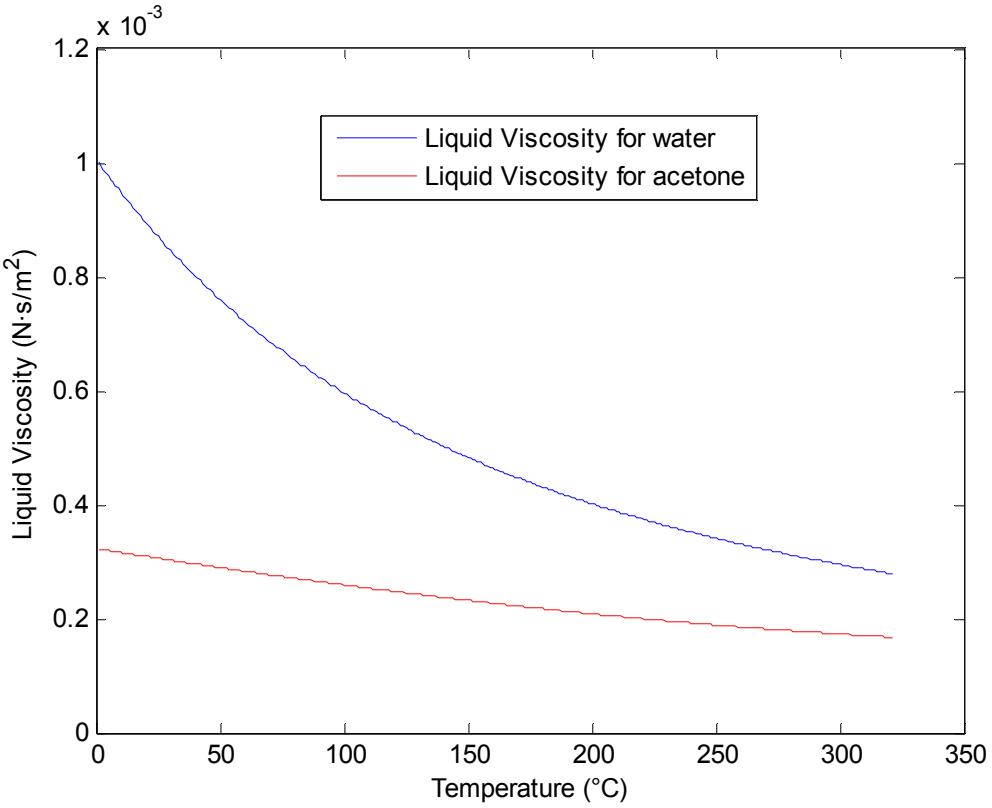

Figure 6.14. Liquid viscosity with temperature variation for water and acetone.

Figure 6.14 shows the viscosity of the liquid with temperature for water and acetone. A higher viscosity fluid has more resistance to the flow in the tubing of an OHP. Thus, higher viscosity should lead to lower performance in an OHP. Since the viscosity of water is higher than that of acetone, viscosity will favor the performance of the acetone-OHP. This again is consistent with the experimental data.

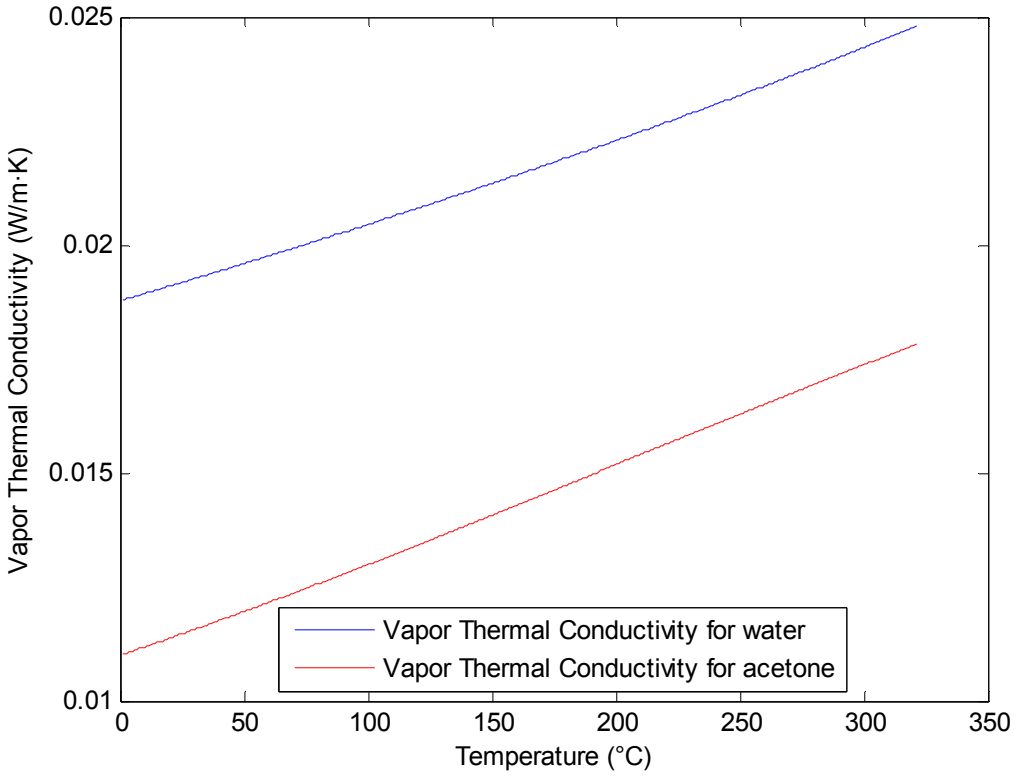

Figure 6.15. Vapor thermal conductivity with temperature variation for water and acetone.

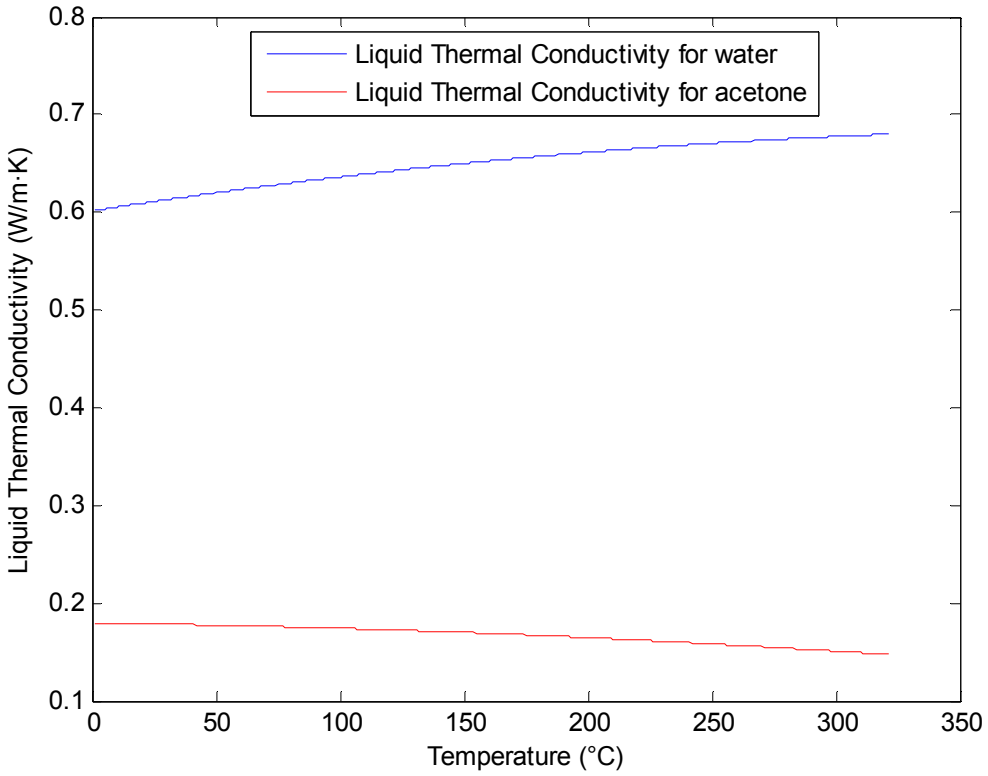

Figure 6.16. Liquid thermal conductivity with temperature variation for water and acetone.

In Figures 6.15 and 6.16, water shows higher thermal conductivity than acetone for both the vapor and liquid phases. Higher thermal conductivity should produce better performance in an OHP. Since the water-OHP shows a lower performance than the acetone-OHP it is inferred that thermal conductivity of the fluids is not a dominant factor at heat inputs of these studies.

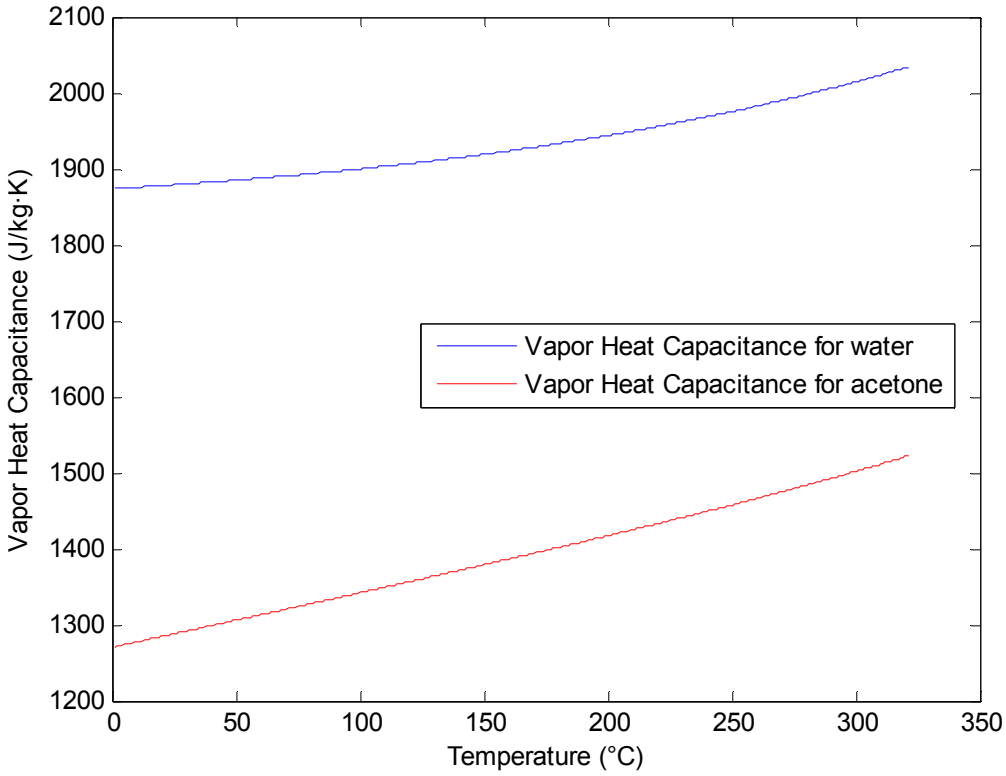

Figure 6.17. Vapor heat capacitance with temperature variation for water and acetone.

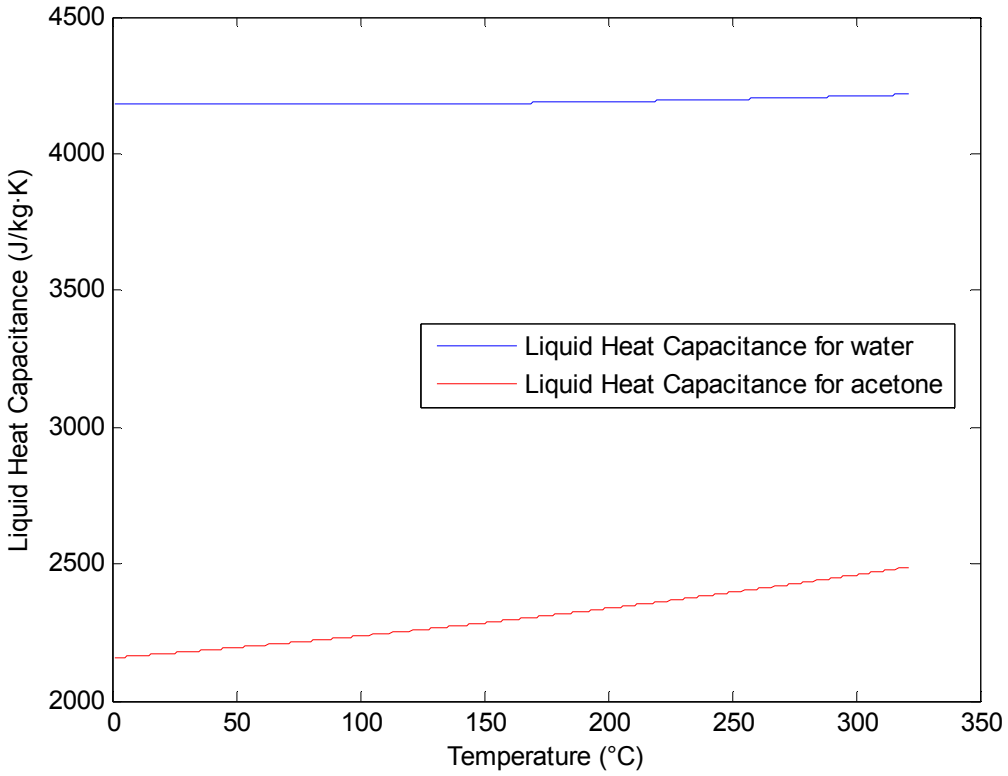

Figure 6.18. Liquid heat capacitance with temperature variation for water and acetone.

In Figures 6.17 and 6.18, vapor and liquid heat capacitances for water and acetone are shown. For a fluid that has a higher heat capacitance, it takes more heat to raise the temperature of the material and should transfer more heat for a given temperature difference between the evaporator and condenser. Since water has a higher heat capacitance but the acetone-OHP performs better, it is inferred that heat capacitance is not a dominant factor in performance at the heat inputs of these studies.

From the analysis above, and the fact that the acetone-OHP shows better performance than the water-OHP over a heat input range of about 25 to 75 Watts it is inferred that the contribution of liquid density, liquid viscosity, and vapor pressure are the more important factors in this heat input range for the OHP design used in these studies. In as yet unpublished experimental data, the water-OHP shows better performance than

acetone-OHP at heat inputs above 150 Watts up to 250 Watts (Wilson, 2008b). These results do not have corresponding neutron imaging results. Thus the dominating fluid properties on performance may change at higher heat inputs for this OHP design.

6.10 Error analysis

In these studies, there are a number of factors that produce uncertainties. First, scattered neutrons produce uncertainties. When neutrons interact with sample material, some of the neutrons are scattered in random directions. Some of these neutrons arrive at the detector and register as neutron intensity. This neutron intensity overlays the intensity from straight-line transmission and attenuation through the sample. The correction of uncertainties from scattered neutrons is not easy at this time because of the complicated geometries of the samples.

Second, the image acquisition has inherent uncertainties such as a non-uniform response and nonlinearities in the detector, although dark current and sensitivity correction were done with the detector output. Conversion efficiencies for neutrons to photons in the scintillator and from photons to electric signals in the silicon plate will cause uncertainties. Dead time is another factor contributing to uncertainty. The neutron image detector produces 12-bit intensity values. Thus, its depth range is 0 to 4095. The average intensity of each pixel of each frame of the original image data at zero heat input for the water-OHP is 400.39. This is 9.7% of the total available intensity that could be read. This means that inherent uncertainties of imaging device may cause some data distortion because of low image intensities.

Third, uncertainties can be produced from the algorithms used to find the vapor and liquid volume fractions. For example, the 'intensity_in' data at boundaries between the liquid and vapor in the tubes don't show clear characteristics of liquid or vapor. In these cases, determining the 'vapor intensity', I_v and 'liquid intensity', I_l correctly is not easy. These uncertainties are expected to be negligible because the number of positions at boundaries is much smaller than the positions not at boundaries. In many positions in the tubes, determining I_v and I_l was done automatically by algorithms. Thus, there may be some uncertainties in determining I_v and I_l, but this factor is also considered to be negligible by careful observation of the results.

The observed standard deviations of the individual pixel intensities in a sequence of images with time after processing a test at zero heat input for the water-OHP were calculated and are shown in Figure 6.19. With zero heat input, the specimen is static and differences between images are due to the imaging system and not due to motions in the sample. The standard deviations of the corresponding temperature measurements for the zero heat input for the water-OHP were also calculated and are shown in Figure 6.20. Each data point corresponds to an individual thermocouple. The average relative error, standard deviation of the intensity divided by the intensity, in these images was 2.13 %. The maximum and minimum relative errors are 6.32 and 0.72 % respectively. For the temperature measurements, the average thermocouple standard deviation observed was 0.035 °C while the maximum standard deviation was 0.039 °C.

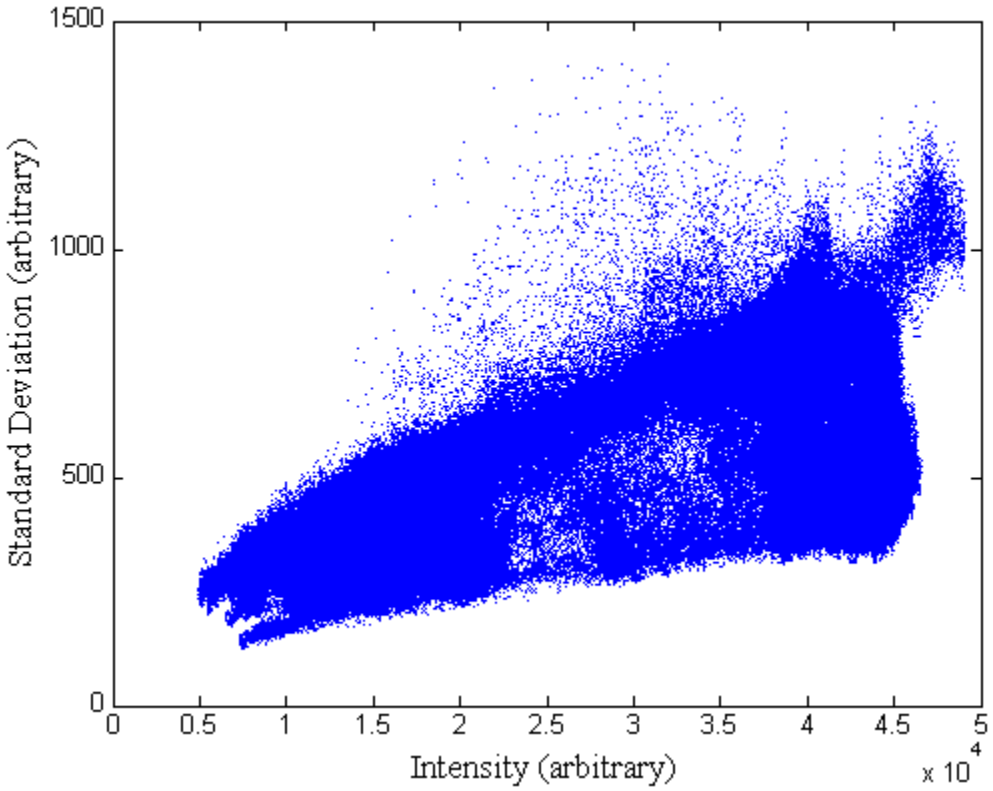

Figure 6.19. The standard deviations of the observed intensities of each pixel of image data after processing at zero heat input for the water-OHP.

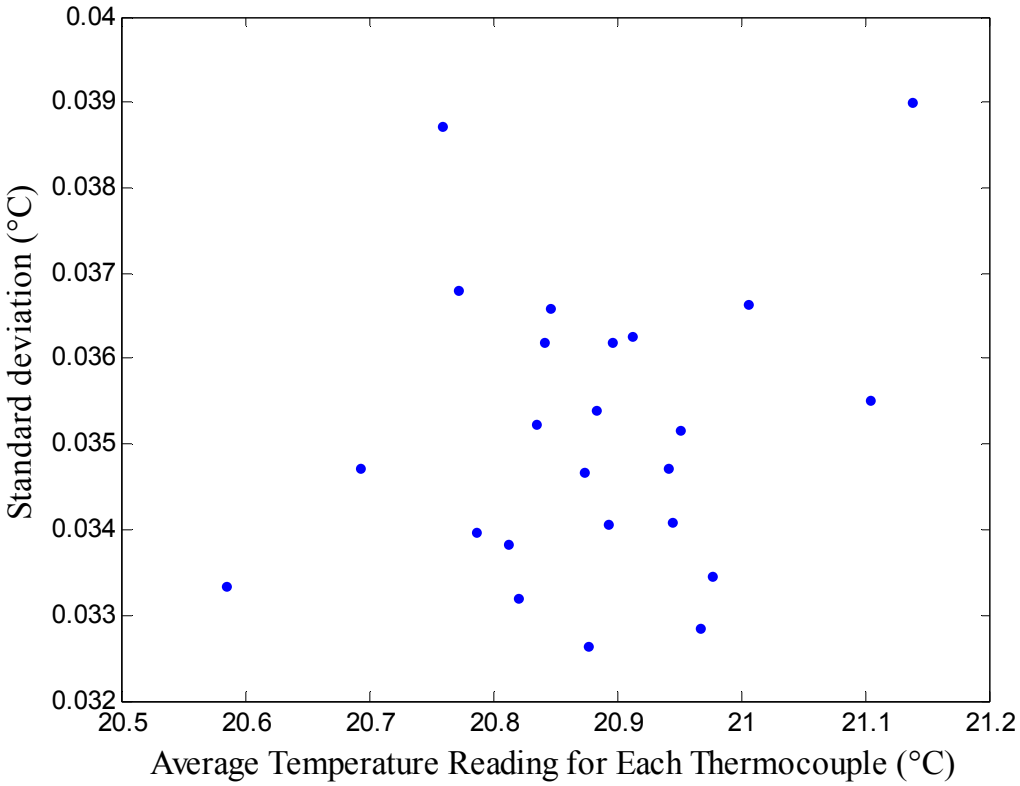

Figure 6.20. The standard deviations of temperature at zero heat input for the water-OHP.

Chapter 7 Conclusions

The purpose of this research was to investigate and quantify the dynamics of the working fluid in OHPs. The volume fraction of vapor and liquid and their distribution in OHPs have been observed and compared with simultaneous temperature data. In these studies, a calibration sample or images of an empty or liquid-filled OHP could not readily be obtained because of experimental conditions. Thus, an algorithm was developed to quantify the vapor and liquid volume fractions in the tubes without calibration samples or images.

To summarize, in these studies neutron radiography is shown to be a good method to investigate and quantify the movement of the working fluid in an OHP. Image data shows the movement of a hydrogen-bearing liquid in real-time.

The volume fraction data of vapor and liquid are matched well with image data. That is, whenever there is a movement of liquid in the tubes, the volume fraction data also reflect the movements. The distribution of liquid and vapor in the OHP among the evaporator, condenser, and adiabatic regions was also calculated using the volume fraction data.

By viewing movie, the liquid has no or little movement for both water- and acetone-OHP before the first startup points. After the startup point, the water shows macro-action and macro-pause periods. Within the macro-action periods, there are micro-action and micro-pause periods. As heat input becomes higher than 197 Watts heat input, it becomes hard to observe the micro-action and micro-pause periods. That is, at higher heat input, water seems to move continuously. Acetone shows continuous

movement after the startup point, so it is hard to observe micro-action and micro-pause periods. So, it can be said that acetone shows more active movement than water at same heat input. Considering the circulation, acetone also shows more circulation movements than water. This is observed not only in video, but also in the data of liquid fraction at the end of evaporator. The average time gap per micro-action period becomes shorter as heat input is increased.

The liquid volume fraction in the evaporator obtained by the algorithm developed for this work increases as the heat input goes up. This is because the liquid moves and enters into the evaporator more actively at higher heat input. It can be synchronized with movement of liquid in the video. Thus, the fraction data obtained by the algorithm are valid for analyzing the behavior of liquid in the OHPs.

The first startup points occurred after the heat input is raised from 25 to 50 Watts for both water- and acetone-OHPs. At the first startup point, the time taken after raising the heat input is shorter for the water-OHP and the temperature is lower for the acetone-OHP. The temperature at the third startup point is lower than at the fourth startup point for the water-OHP.

Compared to the water-OHP, the acetone-OHP shows better thermal performance based on the heat transfer coefficient. This is partly explained by the more active movement of the acetone compared to the water which can be readily visualized and is reflected quantitatively in the volume fraction data for the evaporator section of the OHP. Higher heat input also produces more active liquid movement and, as a result, gives better performance. The movement of liquid is affected by viscosity and density of liquid and the variation of vapor pressure with temperature. So, it can be said that these three

characteristics contribute to determining the performance of OHP. This performance result is restricted to a heat input from about 25 to 75 Watts.

Comparing volume fraction data and average temperature data, the volume fraction data matches well with the average temperature data. We see that temperature fluctuations are caused by the active movement of liquid in the tubes. Whenever there is an active movement of liquid, the volume fraction data changes and the temperature data shows fluctuations.

Though volume fraction data show connection with average temperature data, individual volume fraction data at one thermocouple location do not show a strong connection with the temperature data at the same thermocuple. This means that the temperature fluctuations on an individual thermocouple are not always affected by the liquid-vapor interfaces passing by them.

In these studies, there are some inherent uncertainties from various sources. The average relative intensity error at each data point in images at zero heat input is 2.13 % with maximum and minimum relative error of 6.32 and 0.72 % respectively. The average thermocouple standard deviation is 0.035 °C with the maximum standard deviation of 0.039 °C.

Chapter 8 Suggestions for Further Research

There are some suggestions for further studies. Firstly, in Figure 5.10 and Figure 5.11, macro-action periods and macro-pause periods alternately occur. It is inferred that there are some factors to move and stop the liquid in the tubes. One of the possible factors is critical overall temperature of tubes or temperature difference between evaporator and condenser that causes movement of the liquid. Thus, there is a need to investigate the temperature data for initiating macro-action and for causing macro-pause of water and acetone in tubes, respectively with image data obtained by neutron imaging. In the plotted data in Figure 5.11, it is shown that there are two macro-action periods and one macro-pause period. These data were imaged for 300 seconds. With sufficient time of measurement, critical temperatures or temperature difference between evaporator and condenser for starting and stopping of the working fluids in OHP tubes may be found.

In addition, it is suggested to study the causes why micro-action and micro-pause occur in the OHP tubes. It is estimated that the factors causing macro-action and macro-pause periods can also cause micro-action and micro-pause periods. Also, it is possible to have more factors for micro-action and micro-pause periods than for macro-action and macro-pause periods. In these studies, those types of movement were not observed well for the acetone-OHP. But, at lower and more detailed heat input, it may be possible to observe the movement of acetone acting like water in the tubes. Thus, it will be interesting to discover macro-action and macro-pause periods and micro-action and micro-pause periods for the acetone-OHP. It will be also interesting to study factors in detail making water and liquid behave differently from each other.

It is strongly recommended to study the phenomenon of temperature drop and rising observed in Figure 6.3 and Figure 6.4. Investigation is needed as to why the average temperature in the evaporator increases and in the adiabatic region and condenser it decreases when the liquid starts to move actively. Furthermore, it would be interesting to know why temperatures in some positions are increased and in other positions decreased in the evaporator while temperatures in the adiabatic region and condenser usually decrease.

References

Akachi, H., 1990, Structure of a Heat Pipe, US Patent 4,921,041.

Asano, H., N. Takenaka, T. Fujii and B. Maeda, 2004, "Visualization and Void Fraction Measurement of Gas-Liquid Two-Phase Flow in Plate Heat Exchanger," Applied Radiation and Isotopes 61 (2004) 707–713.

Asano, H., N. Takenaka, T. Fujii, H. Hayashi, and T. Wakabayashi, 2005, Visualization and Void Fraction Measurement of Gas-Liquid Two-Phase Flow in a Commercial Plate Heat Exchanger by Thermal Neutron Radiography, IEEE Transactions on Nuclear Science, Vol. 52, No. 1, February 2005.

Berger, H. 1970, "Neutron Radiography," Research Techniques in Nondestructive Testing, R. S. Sharpe, ed., Academic Press, New York, NY, 269-314.

Berger, H. 1971, "Neutron Radiography," Annu. Rev. Nucl. Sci. 1971.21:335-364.

Berger, H. 2004, "Advances in Neutron Radiographic Techniques and Applications: a Method for Nondestructive Testing," Applied Radiation and Isotopes 61 (2004) 437–442.

Bücherl, T., N. Kardjilov, C. L. von Gostomski, E. Calzada and A. M. ELGhobary, 2004, "A mobile Neutron Source Based on the SbBe Reaction," Applied Radiation and Isotopes 61 (2004) 659–662.

Domanus, J.C., R. Matfield, J.F.W. Markgraf and D.J. Taylor, 1992, "Imaging Techniques," Practical Neutron Radiography, J.C. Domanus, ed., Kluwer Academic Publishers, Boston, 51-56.

Estermann, M. and J. Dubois, 2005, "Investigation of the Properties of Amorphous Silicon Flat-Panel Detectors Suitable for Real-Time Neutron Imaging," IEEE TRANSACTIONS ON NUCLEAR SCIENCE, VOL. 52, NO. 1.

Estermann, M., G. Frei, E. Lehmann, and P. Vontobel, 2005, "The Performance of an Amorphous Silicon Flat Panel for Neutron Imaging at the PSI NEUTRA Facility," Nuclear Instruments and Methods in Physics Research A 542 (2005) 253–257.

Glasstone, S. and A, Sesonske, 1994, "Nuclear Reactor Engineering: Reactor Design Basics," 4th edition, vol 1, An International Thomson Publishing Company, New York.

Harms, A.A., and D.R. Wyman, 1986, "Mathematics and Physics of Neutron Radiography," D. Reidel Publishing Company, Boston.

Hawkesworth M.R. and J. Walker, 1983, "Basic Principles of Thermal Neutron Radiography," Neutron Radiography, Proceedings of the First World Conference, J.P. Barton and P.V.D. Hardt eds., D. Reidel Publishing Company, Boston, 5-21.

Hibiki, T., K.Mishima, K.Yoneda, S.Fujine, K.Kanda, H.Nishihara, A.Tsuruno, M.Matsubayashi, M.Sobajima and O.Ohtomo, 1992, "Study on Two-phase Flow Using Image Processing Technique," Neutron Radiography(4): Including Radioscopy and Complementary Inspection Methods Using Neutrons, Proceedings of the Fourth World Conference, J.P. Barton, ed., Gordon and Breach Science Publishers, Langhorne, PA, 317-324.

Jacobson, D. L., 30 Sep 2007, Gaithersburg, MD (personal communication).

Jacobson, D. L., D. S. Hussey, E. Baltic, J. LaRock, M. Arif, J. Gagliardo, J. Owejan, T. Trabold, "Neutron Radiography and Tomography Facilities at NIST to analyze in-situ PEM Fuel Cell Performance", Proceedings of the 8th World Conference on Neutron Radiography, (2006).

Kandlikar, S.G., and Steinke, M.E., 2002, "Flow Boiling Heat Transfer Coefficient in Minichannels-Correlation and Trends", Proc. of 12th Int. Heat Transfer Conference, Grenoble, France, Paper ~ 1178.

Karimi, G. and J.R. Culham, 2004, "Review and Assessment of Pulsating Heat Hipe Mechanism for High Heat Flux Electronic Cooling," Proceedings of 2004 Inter Society Conference on Thermal Phenomena.

Koerner, S., E. Lehmann, and P. Vontobel, 2000, "Development and Optimization of a CCD-Neutron Radiography Detector," Nuclear Instruments and Methods in Physics Research A 454 (2000) 158-164.

Lehmann, E. H., P. Vontobel, G. Frei and C. Bronnimann, 2004, "Neutron Imaging-detector Options and Practical Results", Nuclear Instruments and Methods in Physics Research A 531 (2004) 228–237.

Ma, H.B., M.A. Hanlon and C.L. Chen, 2006, "An Investigation of Oscillating Motions in a Miniature Pulsating Heat Pipe," Microfluid Nanofluid (2006) 2: 171–179.

Sarkar, P. S., Y. Kashyap, Amar Sinha, P. K. Vijyan, and G. S. S. Prasada Rao, 2005, "Applications for Real-Time Neutron Radiography for Convection Driven Flow Pattern Transition Studies," IEEE Transactions on Nuclear Science, Vol. 52, No. 1, February 2005.

Siegmund, O.H.W., J.V. Vallerga, A. Martin, B. Feller, M. Arif, D.S. Hussey and D.L. Jacobson, 2007, "A High Spatial Resolution Event Counting Neutron Detector Using Microchannel Plates and Cross Delay Line Readout," Nuclear Instruments and Methods in Physics Research A 579 (2007) 188–191.

Silva, A.X. da, and V.R. Crispim, 2001, "Study of a Neutron Radiography System Using ^{252}Cf neutron Source," Radiation Physics and Chemistry 61 (2001) 515–517.

Sonoda, K., A. Ono, N. Takenaka, T. Fujii, S. Tazawa and T. Nakanii, 1992, "Visualization and Volumetric Fraction Measurement of Multiphase Flow by Neutron Radiography," Neutron Radiography(4): Including Radioscopy and Complementary Inspection Methods Using Neutrons, Proceedings of the Fourth World Conference, J.P. Barton, ed., Gordon and Breach Science Publishers, Langhorne, PA, 347-354.

Uchimura, K., G.D. Harvel, T. Matsumoto, M. Kanzaki and J. Chang, 1998, An Image Processing Approach for Two-phase Interfaces Visualized by a Real Time Neutron Radiography Technique, Flow Measurement and Instrumentation 9 (1998) 203–210.

Wilson, C., 2006, "Experimental Investigation of Nanofluid Oscillating Heat Pipes," MS Thesis, Columbia MO, University of Missouri.

Wilson, C., 2008a Research Assistant, University of Missouri, private communication, Apr 7, 2008.

Wilson, C., 2008b Research Assistant, University of Missouri, private communication, July 9, 2008.